

ATOMIC FORCE MICROSCOPY STUDIES OF THE
REACTION OF LITHIUM WITH AMORPHOUS SI-SN
ALLOYS

By
Luc Yvon Beaulieu

SUBMITTED IN PARTIAL FULFILLMENT OF THE
REQUIREMENTS FOR THE DEGREE OF
DOCTOR OF PHILOSOPHY
AT
DALHOUSIE UNIVERSITY
HALIFAX, NOVA SCOTIA
JULY, 2002

© Copyright by Luc Yvon Beaulieu, 2002



National Library
of Canada

Bibliothèque nationale
du Canada

Acquisitions and
Bibliographic Services

Acquisitons et
services bibliographiques

395 Wellington Street
Ottawa ON K1A 0N4
Canada

395, rue Wellington
Ottawa ON K1A 0N4
Canada

Your file *Votre référence*
ISBN: 0-612-83574-X
Our file *Notre référence*
ISBN: 0-612-83574-X

The author has granted a non-exclusive licence allowing the National Library of Canada to reproduce, loan, distribute or sell copies of this thesis in microform, paper or electronic formats.

L'auteur a accordé une licence non exclusive permettant à la Bibliothèque nationale du Canada de reproduire, prêter, distribuer ou vendre des copies de cette thèse sous la forme de microfiche/film, de reproduction sur papier ou sur format électronique.

The author retains ownership of the copyright in this thesis. Neither the thesis nor substantial extracts from it may be printed or otherwise reproduced without the author's permission.

L'auteur conserve la propriété du droit d'auteur qui protège cette thèse. Ni la thèse ni des extraits substantiels de celle-ci ne doivent être imprimés ou autrement reproduits sans son autorisation.

Canada

DALHOUSIE UNIVERSITY
FACULTY OF GRADUATE STUDIES

The undersigned hereby certify that they have read and recommend to the Faculty of Graduate Studies for acceptance a thesis entitled "Atomic Force Microscopy Studies of Lithium with Amorphous Si-Sn Alloyws", by Luc Beaulieu in partial fulfilment for the degree of Doctor of Philosophy.

Dated: August 27, 2002

External Examiner:

Research Supervisor:

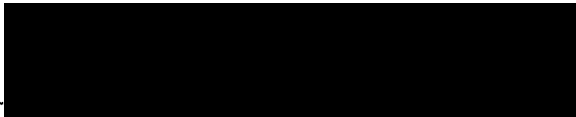
Examining Committee:

DALHOUSIE UNIVERSITY

Date: July, 2002

Author: Luc Yvon Beaulieu
Title: Atomic Force Microscopy Studies of the Reaction
of Lithium with Amorphous Si-Sn Alloys
Department: Physics and Atmospheric Science
Degree: Ph.D. Convocation: Oct Year: 2002

Permission is herewith granted to Dalhousie University to circulate and to have copied for non-commercial purposes, at its discretion, the above title upon the request of individuals or institutions.



Signature of Author

THE AUTHOR RESERVES OTHER PUBLICATION RIGHTS, AND NEITHER THE THESIS NOR EXTENSIVE EXTRACTS FROM IT MAY BE PRINTED OR OTHERWISE REPRODUCED WITHOUT THE AUTHOR'S WRITTEN PERMISSION.

THE AUTHOR ATTESTS THAT PERMISSION HAS BEEN OBTAINED FOR THE USE OF ANY COPYRIGHTED MATERIAL APPEARING IN THIS THESIS (OTHER THAN BRIEF EXCERPTS REQUIRING ONLY PROPER ACKNOWLEDGEMENT IN SCHOLARLY WRITING) AND THAT ALL SUCH USE IS CLEARLY ACKNOWLEDGED.

Contents

List of Tables	vii
List of Figures	viii
List of Symbols ¹	xiii
Abstract	xx
Acknowledgment	xxi
Special Thanks to...	xxii
1 Introduction	1
1.1 Batteries	1
1.1.1 Li-Based Batteries	3
1.1.2 Lithium alloys	4
1.2 Samples	13
1.2.1 Sample Preparation	13
1.2.2 Sample Processing	15
2 Electrochemical Behavior of Si-Sn Electrodes	20
2.1 Cycling Behavior of $\text{Si}_{0.66}\text{Sn}_{0.34}$	20
2.2 X-Ray Characterization of $\text{Si}_{0.66}\text{Sn}_{0.34}$	22

3	Introduction to Atomic Force Microscopy	40
3.1	Working of an AFM	40
3.1.1	Contact Mode	43
3.1.2	Other imaging Techniques	44
3.1.3	Imaging Artifacts	44
3.2	Experimental Setup	51
3.3	Imaging Analysis	53
3.3.1	Image Flattening	53
4	<i>In Situ</i> AFM characterization of Electrode Materials	57
4.1	Morphology of $\text{Si}_{0.66}\text{Sn}_{0.34}$ Thin Film Electrodes	57
4.2	Measuring Volume Changes	73
4.2.1	Volume Changes from RMS Roughness	73
4.2.2	Volume Changes from Patterned Surfaces	79
4.3	Volume Changes of Patterned α -Si Electrodes	84
4.4	Volume Changes of Patterned Sn Electrodes	92
4.5	Volume Changes of Patterned Si-Sn Electrodes	104
5	Comparison to Other Systems	116
5.1	$\text{Mo}_{1-x}\text{Sn}_x$ System	116
5.2	Al Electrodes	123
6	Conclusion	129
6.1	Future Work	130
6.2	Final Remarks	133
A	Sputter Deposition	135
B	Substrate Polishing	141
C	X-ray Analysis	145
C.1	Powder Diffraction	145

C.2	<i>In Situ</i> X-Ray Diffraction	148
C.3	Debye Scattering Equation	149
D	Fitting Theory	152
E	Software	155
E.1	Introduction	155
E.1.1	Tower Fitting Program	156
	Bibliography	162

List of Tables

1.1	Comparison of different types of rechargeable batteries.	2
1.2	Gravimetric capacities of lithium alloys.	4
4.1	Description of the images displayed in figure 4.5.	65
4.2	Height changes of a Si tower as it reacts with Li.	89
4.3	Volume per Sn and percent depth of discharge for different Li-Sn phases.104	
B.1	Directions for polishing stainless steel.	143

List of Figures

1.1	Li-Sn phase diagram.	6
1.2	Voltage profile and differential capacity plot of a Li/Sn cell.	7
1.3	Li/SnO cell cycled between two different voltage windows	9
1.4	Sputtering masks used to prepare $\text{Si}_{1-x}\text{Sn}_x$	14
1.5	Composition, x , in $\text{Si}_{1-x}\text{Sn}_x$ as a function of r	16
1.6	Set-up used to measure the resistivity of $\text{Si}_{1-x}\text{Sn}_x$ as a function of x	17
1.7	Resistivity of $\text{Si}_{1-x}\text{Sn}_x$ as a function of x	18
1.8	X-ray diffraction patterns of $\text{Si}_{1-x}\text{Sn}_x$ for different values of x	19
2.1	Voltage profiles of Li/graphite and Li/ $\text{Si}_{0.66}\text{Sn}_{0.34}$ cells.	21
2.2	Capacity versus cycle number of a Li/ $\text{Si}_{0.66}\text{Sn}_{0.34}$ cell.	21
2.3	Comparison between calculated and experimental x-ray diffraction pattern of $\text{Si}_{0.66}\text{Sn}_{0.34}$	22
2.4	<i>In situ</i> x-ray analysis of a Li/ $\text{Si}_{0.66}\text{Sn}_{0.34}$ cell (first discharge).	24
2.5	Comparison between x-ray diffraction patterns of a Li/ $\text{Si}_{0.66}\text{Sn}_{0.34}$ cell at different states of charge.	25
2.6	<i>In situ</i> x-ray analysis of a Li/ $\text{Si}_{0.66}\text{Sn}_{0.34}$ cell (first charge).	26
2.7	<i>In situ</i> x-ray analysis of Li/ $\text{Si}_{0.66}\text{Sn}_{0.34}$ cell (second discharge).	27
2.8	<i>In situ</i> x-ray analysis of Li/ $\text{Si}_{0.66}\text{Sn}_{0.34}$ cell (second charge).	28
2.9	Comparison between the x-ray diffraction pattern of a fully discharged $\text{Si}_{0.66}\text{Sn}_{0.34}$ electrode and a simulated x-ray diffraction pattern of a Li-Sn tetrahedron.	30

2.10	Comparison between the x-ray diffraction pattern of the fresh cell and the fully discharged cell.	31
2.11	Fitting of <i>in situ</i> x-ray diffraction patterns.	33
2.12	Fitting of <i>in situ</i> x-ray diffraction patterns.	34
2.13	Fitting analysis of <i>in situ</i> x-ray diffraction experiment.	35
2.14	Voltage versus capacity for hysteresis analysis.	37
2.15	Difference between average charge and discharge potentials versus specific current.	38
3.1	Schematic representation of an atomic force microscope.	41
3.2	SEM images of nanoprobes	42
3.3	Numerical simulation of an AFM image of a square step of constant height imaged with a pyramid-shaped tip.	45
3.4	Double imaging produced by a tip having two minima	46
3.5	Piezo tube used in the AFM scanner	47
3.6	Hysteresis curve of a piezo in an AFM scanner.	48
3.7	Combined effects of tip shape, hysteresis, creep, and cross coupling in an AFM image.	50
3.8	Picture of the AFM inside the glovebox.	51
3.9	Wetcells used to house the sample during imaging.	52
3.10	Plane fitting of an AFM topograph.	54
3.11	Geometry of the AFM tip during imaging.	55
3.12	Comparison between images flattened by commercial software and our software.	56
4.1	Schematic showing the morphology change of a $\text{Si}_{0.66}\text{Sn}_{0.34}$ film during the reaction with lithium.	60
4.2	Results of an <i>in situ</i> optical microscopy experiment performed on a $\text{Li}/\text{Si}_{0.66}\text{Sn}_{0.34}$ cell.	61

4.3	Average particle size of a $\text{Si}_{0.66}\text{Sn}_{0.34}$ film as a function of the first discharge capacity.	63
4.4	Schematic representation of the stress involved during the delithiation of a $\text{Si}_{0.66}\text{Sn}_{0.34}$ film.	64
4.5	Results of an <i>in situ</i> AFM experiment performed on a $\text{Li}/\text{Si}_{0.66}\text{Sn}_{0.34}$ cell.	66
4.6	Three-dimensional AFM images.	68
4.7	The resemblance of a $\text{Si}_{0.66}\text{Sn}_{0.34}$ film after contraction to cracked mud.	70
4.8	Schematic representation of a rough film on a smooth substrate before and after lithiation. Change in RMS roughness and voltage versus AFM scan number.	71
4.9	Surface distributions of the substrate and sample.	74
4.10	Model showing the effects of the substrate roughness on the ability to measure the doubling of film thickness.	76
4.11	Change in height of $\text{Si}_{0.66}\text{Sn}_{0.34}$ occurring during the first discharge determined from RMS roughness and average piezo voltage changes.	77
4.12	Cross-section of an AFM image compared to an AFM tip.	79
4.13	Mesh used to produce patterned electrode materials.	80
4.14	Assembly for making patterned surface electrodes.	81
4.15	Imaging a tilted patterned surface with AFM.	81
4.16	Analysis of a square tower imaged an AFM.	82
4.17	Error in AFM volume measurements of a square step.	84
4.18	X-ray diffraction pattern of <i>a</i> -Si.	85
4.19	Electrochemical performance of a $\text{Li}/a\text{-Si}$ cell.	85
4.20	Elemental analysis of an <i>a</i> -Si tower.	87
4.21	Topographic images obtained from an <i>in situ</i> AFM experiment on a patterned <i>a</i> -Si sample.	88
4.22	Area, height, and volume changes of an <i>a</i> -Si tower as it reacts with Li.	90
4.23	Comparison between the voltage profile of an <i>a</i> -Si film and an <i>a</i> -Si patterned electrode.	91

4.24	X-ray diffraction pattern of Sn on copper.	92
4.25	SEM micrographs of patterned Sn.	94
4.26	EDS and WDS analysis of a Sn tower.	95
4.27	The reaction of Sn with lithium shows the decomposition of electrolyte.	97
4.28	<i>In situ</i> AFM images taken during the electrochemical reaction of Li with patterned Sn.	98
4.29	<i>In situ</i> AFM images taken during the electrochemical reaction of Li with patterned Sn.	99
4.30	Selected AFM images of a Sn tower shown in 2 and 3-dimensions.	101
4.31	Change in volume of a Sn tower versus time.	102
4.32	Volume change of a Sn tower compared to the expected volume changes.	103
4.33	X-ray diffraction pattern of sputtered Si-Sn.	105
4.34	SEM images of $\text{Si}_{0.6}\text{Sn}_{0.4}$	107
4.35	Electron microprobe analysis of a $\text{Si}_{0.6}\text{Sn}_{0.4}$ tower.	108
4.36	Topographic images obtained from an <i>in situ</i> AFM experiment on a patterned $\text{Si}_{0.6}\text{Sn}_{0.4}$ sample.	109
4.37	Analysis of an <i>in situ</i> AFM experiment of patterned $\text{Si}_{0.6}\text{Sn}_{0.4}$	110
4.38	Volume measurements of a $\text{Si}_{0.6}\text{Sn}_{0.4}$ tower.	113
4.39	Comparison between the RMS roughness of a patterned electrode to that of a film.	115
5.1	<i>In situ</i> x-ray diffraction experiment of a Li/Mo-Sn cell.	117
5.2	RMS roughness of a Li/ $\text{Mo}_{0.58}\text{Sn}_{0.42}$ cell.	119
5.3	Change in lattice parameter of the BCC $\text{Mo}_{0.66}\text{Sn}_{0.34}$ phase during the reaction with Li.	120
5.4	Result of an <i>in situ</i> AFM experiment on a $\text{Mo}_{0.65}\text{Sn}_{0.35}$ electrode cycled versus Li metal.	121
5.5	Analysis of the <i>in situ</i> AFM experiment for a $\text{Mo}_{0.65}\text{Sn}_{0.35}$ electrode cycled versus Li metal.	122

5.6	Results of an <i>in situ</i> AFM experiment conducted on an Al film as it reacts with Li.	124
5.7	Two and three dimensional AFM images of an Al tower.	126
5.8	<i>In situ</i> AFM result of an Al patterned electrode cycled versus Li. . .	128
6.1	Voltage profile and capacity retention of a composite $\text{Si}_{0.66}\text{Sn}_{0.34}$ electrode cycled versus Li.	131
A.1	Schematic representation of the inside of a sputtering chamber. . . .	136
A.2	Magnetrons used during sputtering.	137
A.3	Sputtering machine at Dalhousie University	138
A.4	Deposition profile from sputtering masks.	139
B.1	LECO VP-160 polishing machine.	142
B.2	Effects on the substrate due to over-polishing.	144
C.1	X-ray beam incident on an electron.	146
C.2	Sketch of the hardware used to build <i>in situ</i> x-ray cells.	149
C.3	Picture showing the experimental setup for performing <i>in situ</i> x-ray diffraction.	150
E.1	Typical AFM image of a patterned electrode and the effects of piezo hysteresis.	157
E.2	Raw AFM data of a patterned electrode fitted to a plane.	159
E.3	Tilting AFM images shows the cross-coupling.	160
E.4	Area and lines used to determine the average height, width, and length respectively.	161

List of Symbols¹

ΔG°	Gibbs free energy
n	number of electrons
F	Faraday's number = 96,487
E	Electromotive force
μ	Chemical potential
e	Magnitude of the charge of an electrode
NHE	Normal hydrogen electrode
ρ	Density
M	Arbitrary metal that reacts with Li
V_f	Final volume
V_i	Initial volume
TOC	Tin oxide composite
X	Nothing or any inactive spectator compound
DC	Direct current

¹Symbols are listed in the order in which they appear in the text.

sccm	standard cubic centimeter per minute
EDS	Energy dispersive spectroscopy
r	Radius
x	Composition of Sn
a	Lattice parameter
a -Si	Amorphous silicon
x	Lithium content
Y_n^{calc}	Linear combination of two x-ray diffraction patterns
Y_{FC}	X-ray diffraction pattern of the <u>F</u> resh <u>C</u> ell
Y_{0V}	X-ray diffraction pattern at zero volts
z	Adjustable parameter $0 \leq z \leq 1$
m	Data points in each x-ray diffraction pattern
n	X-ray diffraction scan number
$calc$	Stands for <i>calculated</i>
M	Total number of data points in each x-ray diffraction pattern
\bar{V}_C	Average charge voltage
\bar{V}_D	Average discharge voltage
AFM	Atomic force microscope
AFMs	Atomic force microscopes
SEM	Scanning electron microscope

LFM	Lateral force microscopy
E	Electric field
M	Molar concentration
EC	Ethylene carbonate
PC	Propylene carbonate
SPM	Scanning probe microscope
<i>Image^{leveled}</i>	Leveled AFM image
<i>Image^{raw}</i>	Raw (as collected) AFM data
<i>Plane</i>	Numerical value of a plane
$\alpha, \beta, \gamma, x_o, \text{ and } y_o$	Adjustable parameters of an elliptical paraboloid
\vec{V}_1 and \vec{V}_2	Vectors
θ	Angle between vectors \vec{V}_1 and \vec{V}_2
CCD	Charge couple device
CD	Compact disk
σ	stress
RMS	Root mean squared
z_i	Surface height of the sample
z_μ	Mean value of the surface height
N	Total number of data points
z	Surface height of the sample

t	Average thickness of the film
Δz	Inherent film roughness
s	Surface of substrate
$P(s)$	Height distribution of the substrate
$P(\Delta z)$	Height distribution of the film
A and B	Amplitude of distributions
e	Natural exponent $e \approx 2.71828$
σ_s	Standard deviation of substrate distribution
$\sigma_{\Delta z}$	Standard deviation of film distribution
$\delta()$	Dirac delta function
$\sigma_{\Delta l_f}$	Standard deviation of film lithiated film
h , w , and l	Height, width, and length respectively
φ and β	Angle of inclination of the sample
θ	Half-angle of an AFM tip
ϕ	Angle of inclination of the sample
ξ , ζ , λ , and μ	Angles
RF	Radio frequency
WDS	Wavelength dispersive spectroscopy
BCC	Body centered cubic
PVdF	Polyvinylidene fluoride

λ	Wavelength
π	$\pi \approx 3.14159$
SEI	Solid electrolyte interface
HOPG	Highly oriented pyrolytic graphite
E	Electric field vector
B	Magnetic field vector
e^-	Symbol for an electron
S	South
N	North
<i>I</i>	Radiated intensity
I_o	Incident intensity
m_e	Electron mass
<i>c</i>	Speed of light
<i>r</i>	Magnitude of a radial vector
f_n	Atomic form factor
$\rho_n(r)$	Radial electronic density
<i>k</i>	Magnitude of the wave vector
\vec{r}	Atomic position vector
x_n, y_n, z_n	Cartesian coordinates of atom <i>n</i>
<i>h, k, l</i>	Miller indices

\vec{G}	Reciprocal lattice vector
$\vec{b}_1, \vec{b}_2, \vec{b}_3$	Basis vectors of reciprocal space
d_{hkl}	Shortest distance between planes (h, k, l)
n	Order of the observed maximum
λ	Wavelength
θ	Angle of incidence
F_{hkl}	Structure factor
N	Number of atoms
i	Complex number $i = \sqrt{-1}$
F^*	Complex conjugate of F
I_{eu}	Intensity in electro units
m, n	Atom number
f_n	Form factor of atom n
s and s_o	Direction vectors of x-ray beam
r	Vector between atoms m and n
θ	Half of the x-ray scattering angle
k	Wave vector
w_i	Weighing factor
y_i^{exp}	Experimental data points
y_i	Points on a straight line

- m Slope of a straight line
- b Intercept of the ordinate and a straight line

Abstract

The electrochemical and mechanical properties of an amorphous $\text{Si}_{0.66}\text{Sn}_{0.34}$ compound are studied as it reacts with Li. This material is shown by *in situ* x-ray diffraction to remain amorphous during the reaction with Li. This unusual structural behavior is believed to account for the excellent capacity retention displayed by Li/ $\text{Si}_{0.66}\text{Sn}_{0.34}$ cells. To study the changes in the morphology of $\text{Si}_{0.66}\text{Sn}_{0.34}$ as it reacts with Li *in situ*, a commercial atomic force microscope (AFM) has been placed inside an argon-filled glovebox. To increase the sensitivity, the AFM has been placed on a vibration damping system and surrounded by a draft shield. A heating element placed inside the draft shield is used to maintain the entire microscope and sample at a constant temperature. Using this AFM workstation, we show how $\text{Si}_{0.66}\text{Sn}_{0.34}$ can reversibly react with Li to undergo volume changes on the order of 250%.

The AFM workstation has also been used to study α -Si, Sn, Al, and $\text{Mo}_{0.65}\text{Sn}_{0.35}$ as they react with Li. *In situ* atomic force microscopy has been used to observe an anomalous catalytic reaction occurring at the surface of Sn. *In situ* atomic force microscopy has also been used to help identify a BCC $\text{Mo}_{0.65}\text{Sn}_{0.35}$ phase as an intermetallic insertion material for Li. This unique reaction has never been reported for any intermetallic system.

Acknowledgment

Je souhaite remercier mes parents pour l'encouragement et le support financé qu'ils m'ont donné durant mes années universitaires.

I would like to thank all my colleagues which have worked in this lab during the time of both my M.Sc. and Ph.D. Although the list is too long to name them all, I would like to acknowledge Tim Hatchard and Arman Bornakdapour for making my samples, David Stevens for many useful discussions and Simon Trussler for machining most of the equipment used to perform my experiments.

I would like to thank the members of my committee, Dr. Rich Dunlap and especially Dr. Manfred Jericho for taking time off during his summer vacation to read my thesis and participating in the examination process.

I would also like to thank my better half Bronwyn Vigneault-MacLean for proof-reading my thesis and mostly for being there with her support and encouragement at every step of the way.

Finally, I would like to thank and acknowledge my supervisor Jeff Dahn whose help and support has been the main source of inspiration and drive in my research. Through enormous generosity, Jeff has given me countless opportunities which have allowed me to obtain all the success which I have had and for which I will never forget.

Special Thanks to...

- Bridget Trim, Gloria Tweedy, Judy Hollett, Barbara Gauvin for everything from taking care of pay checks to filling out order forms but mostly for putting up with my impatient.
- Alex Feargrieve and again Simon Trussler for all the machining required for this project.
- Andy George for answers to endless questions.
- Jim Chisholm for all the computer support.
- John Duane (a.k.a Duane Borgal) For all the help in finding the right fittings.
- Dr. J. Kreuzer and Dr. J. Cordes for answers to many of my theoretical questions.
- Dr. Michael A. Gharghouri for introducing me to proper polishing methods and letting me use his equipment at Daltech.
- Bob MacKay for use and time on his electron probe.
- Thanks to the people at 3M mainly Larry Krause and Bob DeMaster for helping me obtain my NSERC industrial post graduate scholarship.
- Thanks to NSERC for the same reason.

Chapter 1

Introduction

1.1 Batteries

A battery is a device used to convert chemical potential energy to electrical energy by means of reduction-oxidation (redox) reactions. Although the term “battery” is often used, the basic electrochemical unit is called a cell¹. A cell is made up of two electrodes, an anode (negative) and a cathode (positive), submerged in an ionically conductive medium, the electrolyte. During operation, the electrodes are connected together by an external circuit. As the external circuit is closed electrons begin to flow from the lower potential electrode to the higher potential electrode. By definition, the anode is the electrode which gives up electrons² to provide the current and the cathode is the electrode which accepts the electron^{3†}.

The design of a battery is often dependent on the amount of work required. The

¹A battery is a collection of cells connected either in series or in parallel.

²The anode is oxidized and is called the reducing agent.

³By accepting the electrons the cathode is reduced and is called an oxidizing agent.

[†]For simplicity, the electrode which is oxidized on the first discharge is usually called the anode while the electrode which is reduced on the first discharge is called the cathode.

amount of work a cell can do is given by the change in Gibbs free energy:

$$\Delta G^\circ = -nFE \quad (1.1)$$

where n is the number of electrons, $F = 96,487$ C is Faraday's constant, and E is the electromotive force (emf) of the cell. The emf of the cell can be defined from the chemical potentials given by equation 1.2

$$E = -\frac{\mu_{cathode} - \mu_{anode}}{e} \quad (1.2)$$

where for the case of a lithium-ion battery, $\mu_{cathode}$ is the chemical potential of Li atoms in the cathode, μ_{anode} is the chemical potential Li atoms in the anode, and e is the magnitude of the electron charge.

There are many different types of rechargeable batteries available on the market. These range from lead-acid to lithium-ion, the latter being the subject of a great deal of study due to its superior performance. Table 1.1 shows a comparison of different types of batteries available. As can be seen, the lithium-ion battery out-performs all other types of batteries on today's market.

Table 1.1: Comparison of different types of rechargeable batteries.

Batteries	Voltage (V)	Specific Energy (Wh/kg)	Energy Density (Wh/l)
Lead-acid	1.98	35	80
Nickel-Cadmium	1.2	50	100
Nickel-Metal hydride	1.2	80	300
Lithium-Ion (C/LiCoO ₂)	3.6	165	420

1.1.1 Li-Based Batteries

Of all the metals, lithium has the lowest potential (-3.01 V versus NHE.)[1]. This, along with its low density ($\rho = 0.54\text{g/cm}^3$), makes lithium metal an excellent choice for producing high-voltage light-weight batteries. Lithium batteries were first introduced starting in the mid 1970s [2, 3, 4, 5, 6, 7, 8, 9]. These first batteries used pure Li metal as the anode while the cathode was either a transition metal oxide (such as MnO_2 or V_2O_5) or a chalcogenide (such as MoS_2 or TiS_2). Unfortunately the presence of Li metal made these types of batteries very hazardous which prompted the search to find safer materials to be used as anodes⁴.

To pursue this goal two schools of thought emerged: One of these focused on different types of graphites as possible anode materials. The initial success of graphite fueled many research projects in many different laboratories [1, 10, 11]. The second group focused on the use of lithium alloys or intermetallic compounds as a replacement for lithium metal. In the following, we give a brief description of the different philosophies taken by various research groups in the search for the best intermetallic anode material. In doing so we hope to highlight the key points that have influenced the anode materials studied in this work and more importantly the method used to study them. For more complete reviews on lithium batteries the reader is referred to the following references [1, 10, 11, 12, 13].

⁴A battery with lithium metal used as the anode is called a *lithium battery*. A battery in which lithium atoms shuttle between the anode (not lithium) and the cathode is called a *lithium-ion battery*.

1.1.2 Lithium alloys

Since the early 1970's, it has been known that lithium can reversibly react, at room temperature, with many elements to form Li_xM alloys where M can be Mg, Ca, Al, Si, Ge, Sn, Pb, As, Sb, Bi, Pt, Ag, Au, Zn, Cd, Hg, Ba, C etc... [1, 14, 15, 16, 17, 18, 19]. As shown in table 1.2, lithium alloys can supply large gravimetric capacities when cycled versus lithium metal. However, due to cost, safety, and environmental con-

Table 1.2: Gravimetric capacities of lithium alloys.

Element M	x in Li_xM	Capacity (mAh/g)	Comments
Ca	2	1337	Not electrically conductive
*Al	1	990	Inexpensive and good conductor
*Si	4.4	4200	Readily available and very affordable.
*Ge	4.4	1625	Readily available.
*Sn	4.4	993	Good electrical conductivity and inexpensive
Pb	3.75	485	Toxic
As	3	1073	Toxic
*Sb	3	660	Poor conductor of heat and electricity
Bi	3	385	Poor conductor of electricity
Pt	2	275	Expensive
Au	3.75	510	Expensive
Zn	1	423	
Hg	3	401	Liquid at room temperature.
Ba	4	781	
C	0.1667	372	Can be expensive

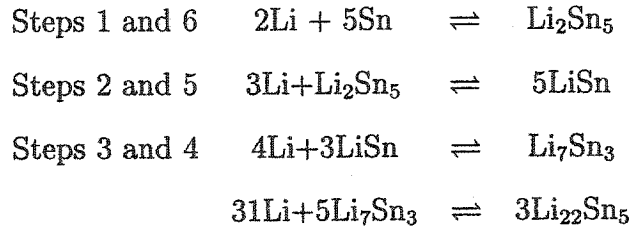
cerns, only the elements labeled with asterisks in table 1.2 have been predominately considered for application as anode materials for lithium-ion batteries.

The reaction of Li with a metal M can be written as:



In the first studies, it was found that this reaction was often accompanied by large volume changes in the lithiated host metal M [1, 10, 20, 21, 22][†]. These volume changes were believed to be the cause of the poor cycling performance observed by these materials. In the late 1980's and the mid 1990's, the study of lithium alloys was taken up by Huggins *et al.*[23, 24, 25, 26, 27, 28] and Besenhard *et al.* [1, 10, 11, 20, 21] who tried to understand the failure mechanisms in lithium alloys and develop strategies to overcome them. It was proposed that the change in volume occurring during the reaction with lithium caused large stresses in the host element M, causing the electrode to suffer from cracking and crumbling. This "self pulverization" was believed to cause loss of electrical contact between the active material and the substrate which in turn led to short cycle life [1, 10, 20, 21].

As an example, the reaction of Li with Sn is described by a series of phase transitions dictated by the Li-Sn phase diagram shown in figure 1.1 [29]. Based on this diagram, the room temperature reaction of Li with Sn occurs via the following path:



These phase transitions can be seen in the voltage profile of a Sn cell cycled against lithium metal. Figure 1.2a shows the voltage as a function of lithium concentration, x , of a Li/Sn cell. The voltage profile shows plateaus indicating two-phase coexistence of different Li-Sn phases (steps 1 to 6 shown above). These plateaus can more easily be seen in a graph of differential capacity versus cell voltage as shown in figure 1.2b.

[†]These volume changes are the main concern of our study and will be expanded upon in the rest of this thesis.

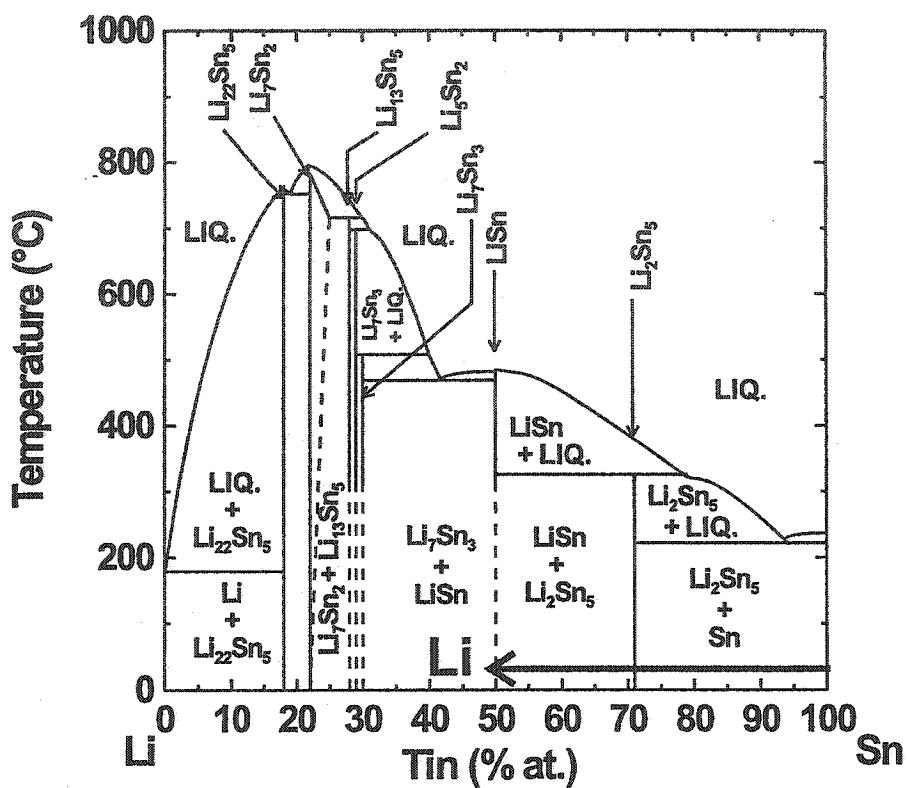


Figure 1.1: The Li-Sn phase diagram shows the many phase transitions undergone when Li is allowed to react with Sn.

Plateaus in a voltage curve manifest themselves as sharp peaks in differential capacity versus voltage. In figure 1.2 each phase transition as numbered above can be observed.

In short, the reaction of Li with Sn can be summarized as follows:



In the tetragonal tin phase there is one tin atom per 27 \AA^3 . Once the tin electrode

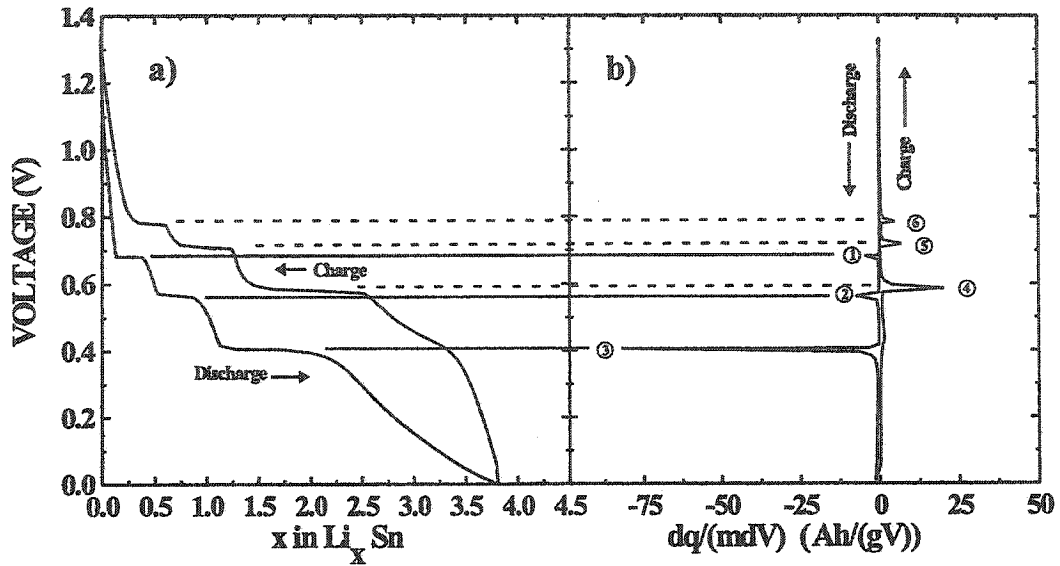


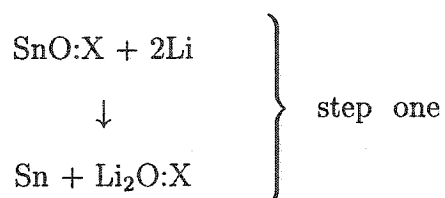
Figure 1.2: a) Voltage versus Li concentration, x , of a Sn electrode cycled versus Li. b) Differential capacity versus cell voltage of the Li/Sn cell from panel (a).

has fully reacted with Li to form $\text{Li}_{4.4}\text{Sn}$ there is one Sn atom for every 96 \AA^3 [30]. This means that the volume surrounding each Sn atom increases by almost 4 times after reacting with lithium. This corresponds to a 255% increase in volume calculated by $(V_f - V_i)/V_i$ where V_f and V_i are the final and initial volume respectively.

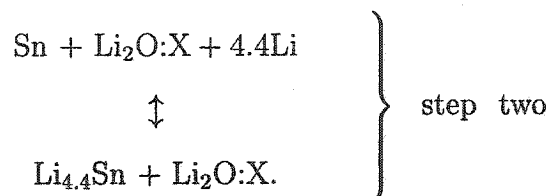
Tin-Oxide Compounds

Due to their reaction mechanism, lithium alloys were found to be poor candidates as anode materials for lithium-ion batteries. Because of this, many groups focused their research on carbonaceous anode materials [1, 10, 11]. However, the study of intermetallic electrodes was rejuvenated when, in 1997, Fuji Film Celltec Co. Ltd. published results showing how amorphous tin oxide composites (TOC) could be used

successfully as anode materials for Li-ion batteries [31]. Though their initial understanding of the reaction mechanism of these TOC was wrong, it was later shown by Courtney *et al.* why these materials were so successful [32, 33, 34, 35, 36]. From this study emerged a complete understanding of the reaction mechanism of TOC type materials. Briefly, Courtney *et al.* showed that for samples like SnO:X or SnO₂:X where X can be nothing or a variety of spectator compounds, the presence of oxygen bonded to the tin caused a large source of irreversible capacity. The general reaction can be described as follows:



and further Li alloys with the formed Sn



Step one shows the irreversible reaction of two Li atoms for every O bonded to Sn and step two shows the reversible alloying of Sn with 4.4 Li atoms. The reaction of O with Li, in step 1, constitutes the source of the irreversible capacity.

In their work, Courtney *et al.* also proposed an explanation for the failure mechanism of Sn-containing materials. As shown earlier, the reaction of Li with Sn occurs via a succession of two-phase steps. Through careful consideration of the structures of each phase, the authors argued that the transition from pure Sn to LiSn occurred

with little disturbance to the active regions of the electrode. Further lithiation of the electrode from LiSn to $\text{Li}_{22}\text{Sn}_5$ on the other hand caused drastic rearrangement of the active part of the anode. This rearrangement came in the form of mismatched boundaries between different Li/Sn phases. These different boundaries were believed to be the site where the electrode could potentially crack and become electrically isolated from the rest of the bulk. In figure 1.3 we reproduce figure 13 of reference [32]. Figure 1.3a shows the poor capacity retention of a Li/SnO cell cycled between

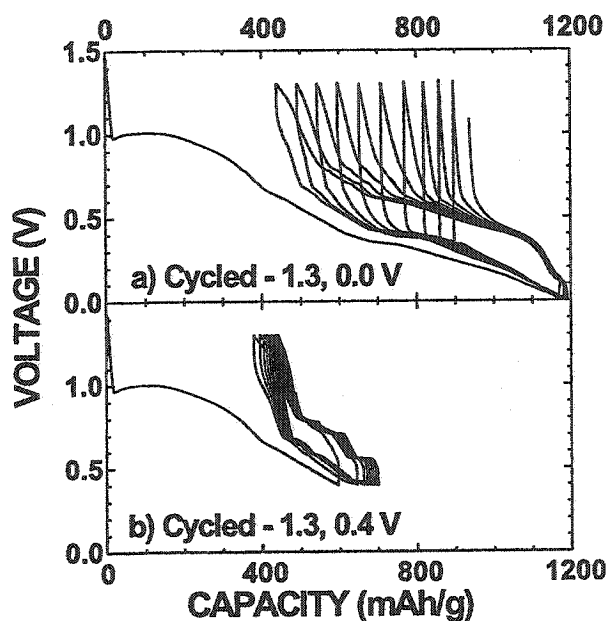


Figure 1.3: SnO/Li cell cycled a) between 1.3–0 V and b) 1.3–0.4 V.

1.3 and 0 V. This voltage window allows the complete reaction of Li with Sn to form $\text{Li}_{4.4}\text{Sn}$. However, figure 1.3b shows that when a Li/SnO cell is cycled between 1.3 and 0.4 V, excellent capacity retention is obtained. In this voltage window the lithium is allowed to react with tin to the compositional limit of LiSn . This figure supports the arguments presented by Courtney *et al.* [32].

In other work, Courtney *et al.* also showed that the concentration of Sn plays

an important role in the cycling performance of these amorphous oxides [35]. In this work it was clearly shown that samples of SnO:X with large concentrations of Sn suffered greater capacity losses upon cycling than those with smaller concentrations of Sn. The poor capacity retention was found to be caused by the aggregation of Sn clusters in the electrode. With every cycle, Sn clusters grew in size allowing the formation of two-phase regions during the reaction with lithium, ultimately causing the electrode to fail.

Active/Inactive Materials

Since the unavoidable presence of oxygen in Fuji-type materials caused large irreversible consumption of Li, which in a Li-ion cell is of a fixed amount, studies on these materials have largely ceased. However, the initial work on these materials inspired the study of what are now known as *Active/Inactive* materials.

The term *Active/Inactive* materials came from the idea of placing *active* materials like Sn in an *inactive* matrix M. The purpose of the inactive elements M is to keep the active element segregated in small clusters in order to avoid two-phase coexistence during the alloying with Li. The first thorough study came from a study of the Sn-Fe-C system [37, 38, 39, 40, 41]. In this work it was found that an active material such as Sn₂Fe mixed with the inactive material SnFe₃C could produce a working electrode capable of delivering approximately 200 mAh/g for over 50 cycles in the voltage window of 1.3–0 V. This result is lower than the capacity of graphite (372 mAh/g). However, when converted to volumetric capacity, the Sn containing material delivers approximately 1500 mAh/cm³ which is a significant improvement over the volumetric capacity of graphite, 800 mAh/cm³. Therefore, in cases where volume is

important (cell phones or watches), this material would be preferred.

The biggest achievement obtained from the work on Active/Inactive materials was to show that it is possible to disperse an active material in an inactive matrix without requiring the presence of oxygen. Since the work from Mao *et al.*, many groups have conducted studies on Active/Inactive materials. Despite this, no significant findings have been published [42, 43, 44].

From the discussion given above, we can now summarize the key points:

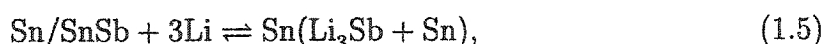
1. Oxygen, when bonded to the active material, can cause large irreversible capacity [32].
2. Large volume changes cause the electrode to crack and possibly become electrically disconnected from the current collector. [1, 10, 20, 21]
3. Best results are obtained when active materials such as Si, Sn, and Al are finely dispersed inside the electrode. This eliminates two-phase coexistence during the reaction with lithium. [32]
4. Minimizing the grain size of the active material improves the performance of the anode material. [33, 37, 38, 39, 40]
5. In the limit of the above statement, amorphous materials perform much better as anode material than crystalline materials⁵.

Active/Active Materials

While some have worked on mixing active materials in inactive matrices, others attempted to mix active materials with different active materials. For example, Huggins

⁵Although other groups have also stated this [45], this statement is based almost entirely on unpublished research that has been conducted in our lab and at 3M.

et al. prepared samples of Si and Cd dispersed in a Li_7Sn_3 matrix [24, 46, 25, 26]. In that study it was found that good cycling could be obtained when the cells were cycled in a way so as to leave the Li_7Sn_3 phase unaffected. In a similar study, Besenhard *et al.* prepared Sn/SnSb powders by electrodeposition [20, 21]. In that study it was found that the more reactive phase (SnSb) would alloy with Li metal at a potential of approximately 850-800 mV versus lithium metal (pure Sn reacts mostly at lower potentials). Therefore, by restricting the depth of discharge to the limited reaction



200 discharge/charge cycles could be achieved. This reaction, which delivers a capacity of 360 mAh/g, is very close to that of graphite 372 mAh/g. However, when these electrodes were discharged completely to 0.0 V, the samples delivered poor capacity retention for the same reasons as described above.

Although the compounds Si/ Li_7Sn_3 or Cd/ Li_7Sn_3 and Sn/SnSb do not represent a true *Active/Active* material, the idea of mixing active materials did not go unnoticed. In 1999, 3M Corp. synthesized amorphous Si-Sn based intermetallic compounds designed to serve as anode materials for lithium-ion batteries [47]. These materials have been shown to deliver large specific and volumetric capacities without compromising the cells' capacity retention. Unfortunately, since this compound is a true *Active/Active* material, it was predicted to undergo large volume changes when fully reacted with lithium. For this material to ever be used as an anode material in commercial lithium-ion batteries these volume changes must be known and understood.

Until recently [48, 49, 50, 51, 52], only a few groups have performed *in situ* studies of the morphology changes of electrode materials. To study these morphology

changes, most researchers have been forced to fall back on *ex situ* measurements of electrode materials. The purpose of this study has been to develop a new and complete system where an atomic force microscope placed inside an argon filled glovebox is used to study the morphology changes of electrode materials *in situ*.

1.2 Samples

In the sections that follow, we will outline how, using combinatorial materials science, a binary system such as Si-Sn can be studied in a time-efficient and effective manner.

1.2.1 Sample Preparation

All of the samples presented in this work were prepared by sputter deposition (see appendix A for a brief description of the sputtering process.)

Two sputtering systems and approaches were used to prepare the samples in this work. One sputtering system is well adapted to making a range of stoichiometries in a single deposition as in combinatorial materials science. The other larger system is well suited to the production of larger quantities of material of a single composition. Combinatorial magnetron sputtering was performed using a Corona Vacuum Coater's (Vancouver, B.C. Canada) V3T system. The system is turbo pumped and reaches a base pressure of 5×10^{-8} Torr[†]. Two inch diameter targets of Si and Sn were used.

The sputtering chamber is equipped with a 40 cm diameter water-cooled rotating substrate table and a stationary mask platform. The mask openings, shown in figure 1.4, were placed as near to the substrate table as possible. The curved mask opening opposite to the Si target was designed so that a constant Si deposition rate (measured

[†]At a pressure of 5×10^{-8} Torr (6.66 μ Pa), a 1 cm³ volume at 21° C contains 1.6×10^9 atoms.

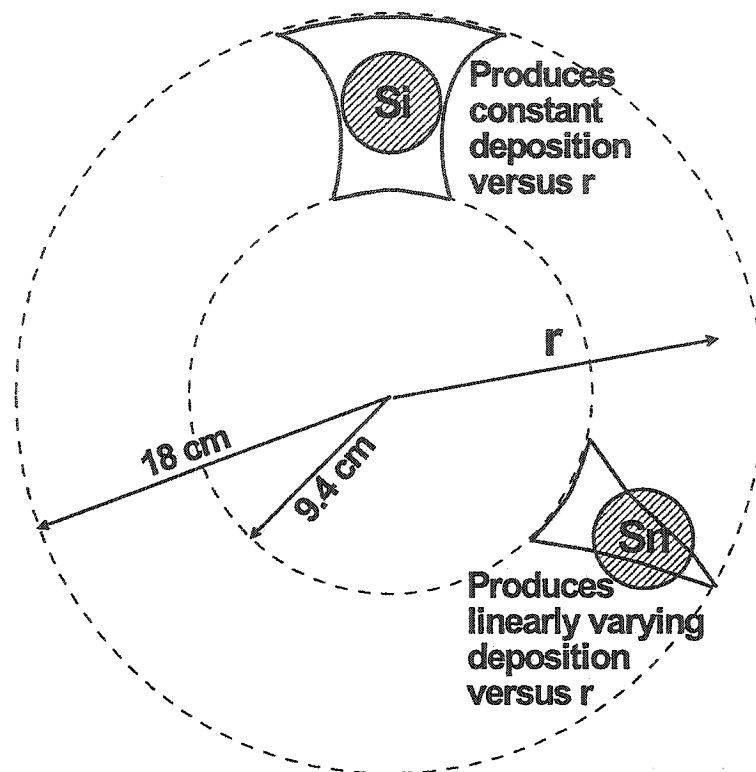


Figure 1.4: Schematic representation of the setup used inside the sputtering chamber at Dalhousie University. Sputtering masks are used to deposit a linear range in composition x in the binary system $\text{Si}_{1-x}\text{Sn}_x$.

in $\text{\AA}/\text{cm}^2/\text{s}$) is maintained as a function of r as shown in figure 1.4 when the substrate table is rotating. The curved mask opening opposite to the Sn target was designed so that a linearly varying deposition rate is achieved as a function of r when the substrate table is rotating. Sputtering and rotation rates were selected so that about one atomic layer of atoms was deposited during each pass under the targets. Both Sn and Si were sputter deposited using DC power supplies, operating at 50 and 300

Watts respectively. The Ar flow rate was about 19 sccm[†], and chamber pressure was maintained at 3.2 mTorr during the deposition. The substrate table angular speed was 20 rpm.

From previous studies, it has been shown that intermetallic alloys with a high concentration of Sn serve as poor anode materials for lithium-ion batteries. For this reason, samples of $\text{Si}_{1-x}\text{Sn}_x$ were made with $0 \leq x \leq 0.5$. In order to verify the proper stoichiometry, the samples were studied by energy dispersive spectroscopy (EDS) using a fully automated 733 JEOL electron microprobe X-ray microanalyzer equipped with an Oxford Link eXL 131 eV energy dispersive detector. The 2 μm electron beam was operated at 15 kV and 15 nA. Figure 1.5 shows the measured stoichiometry as a function of the radial distance. The tin composition, x , is near 0.5 at the inner edge of the deposit (the inner radius r is 9.4 cm) and decreases almost linearly to $x = 0$ at $r = 18.3$ cm. Moreover, the EDS analysis showed no signs of impurities or contaminations from other elements.

1.2.2 Sample Processing

Once the proper stoichiometry of the samples was verified, the next step was processing the samples in order to obtain the most promising material. In order to determine the optimum stoichiometry it is important to know the qualities that enhance the performance of an electrode material. Since the capacity of Si is 4200 mAh/g and that of Sn is 990 mAh/g it would be beneficial to maximize the amount of Si in the sample. However, since Si has a much higher electrical resistivity than Sn ($\rho_{\text{Si}} \approx 3 \times 10^6 \mu\Omega/\text{cm}$ and $\rho_{\text{Sn}} \approx 11 \mu\Omega/\text{cm}$ at 273K [53]) the concentration of Sn must be sufficiently high

[†]The unit sccm stands for *standard cubic centimeter per minute* which indicates the flow rate of one cubic centimeter of gas at standard temperature and pressure per minute.

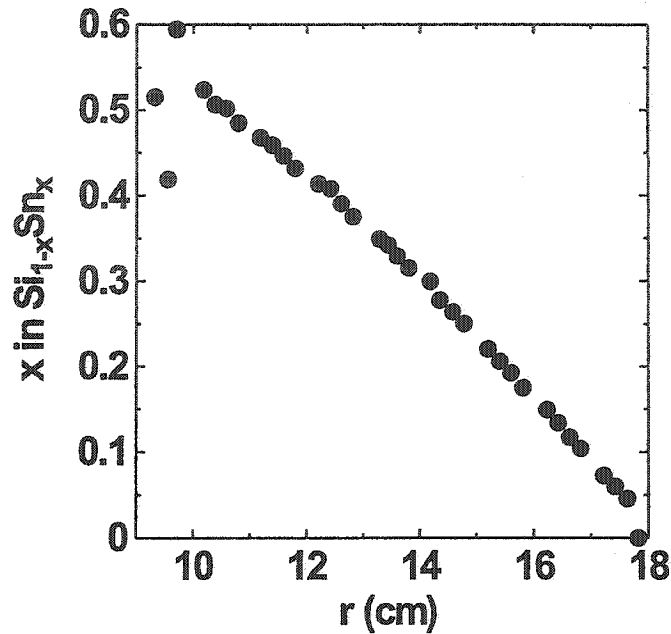


Figure 1.5: Sn composition x in $\text{Si}_{1-x}\text{Sn}_x$ plotted as a function of the radial distance from the center of the sputtering table.

to make the sample useful as an electrode material. Also, as stated earlier, amorphous materials perform much better as anode materials than crystalline materials. With these factors in mind, the samples were first screened by performing resistivity analysis and X-ray diffraction.

Resistivity measurements were made using a two-wire technique with silver painted contacts to the $\text{Si}_{1-x}\text{Sn}_x$ films. A two-wire measurement was deemed sufficient because the film resistance was normally between 10Ω and $10\text{M}\Omega$. As shown in figure 1.6, strips of $\text{Si}_{1-x}\text{Sn}_x$ for $0 \leq x \leq 0.5$ were deposited on microscope slides. The resistivity results were then measured four strips at the time. Figure 1.7 shows the

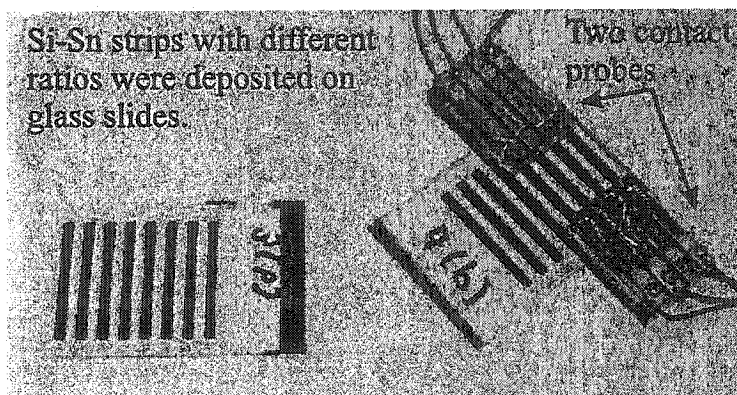


Figure 1.6: Set-up used to measure the resistivity of $\text{Si}_{1-x}\text{Sn}_x$ as a function of x .

resistivity (taken at 21°C) of $\text{Si}_{1-x}\text{Sn}_x$ (solid dots) versus x for the films deposited on the rectangular slides. The value of x was determined from the position of the slide (its value of r) and figure 1.4. The resistivity drops dramatically with x , until about $x = 0.3$, where a change in slope is observed. The data match that collected by Maruyama and Akagi (hollow squares) [54] quite well. However, the precision of our data is much higher so that the change in slope at about $x = 0.3$ can be observed.

X-ray diffraction was performed using an Inel curved position sensitive detector (CPS 120) and a PW 1720 Phillips X-ray generator using $\text{Cu K}\alpha$ radiation. The system is equipped with an automated XY motion stage, which makes it an ideal tool for analyzing the combinatorial samples. (Theory of X-ray diffraction is given in Appendix C at the end of this thesis.) Figure 1.8 shows x-ray diffraction patterns for representative $\text{Si}_{1-x}\text{Sn}_x$ samples with $x = 0.24, 0.36, 0.40$ and 0.53 . All samples with $x \leq 0.36$ are amorphous and all samples with $x \geq 0.40$ show evidence for crystalline tin precipitates. We believe that the change in slope of the resistivity graph is probably

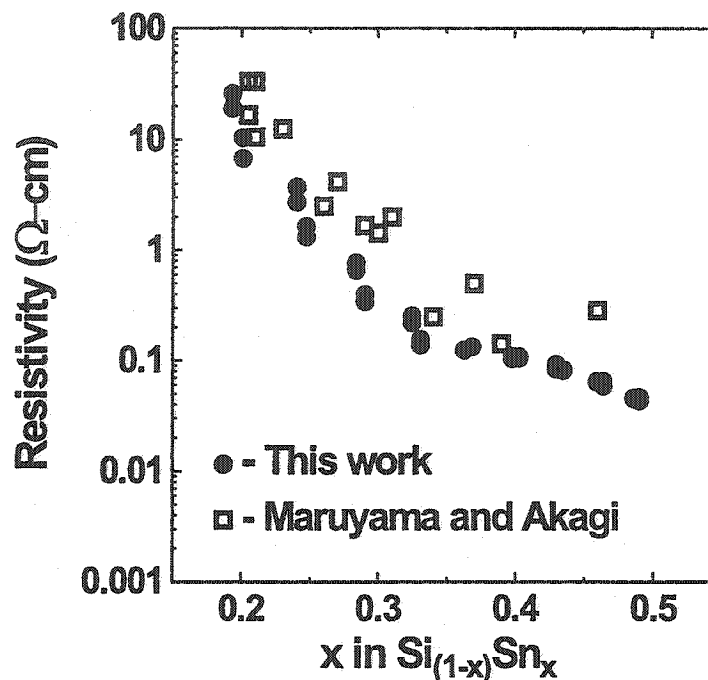


Figure 1.7: Resistivity (Ωcm) as a function of Sn composition x . Solid dots indicate data taken by the present author and hollow squares show data from Maruyama and Akagi [54].

caused by the onset of tin crystallization. The diffraction patterns of the amorphous samples with $x = 0.24$ and 0.36 in figure 1.8 are dominated by the signal from the underlying glass slide because the films are only about $1 \mu\text{m}$ thick.

Based on the results in figures 1.7 and 1.8, the composition $\text{Si}_{0.66}\text{Sn}_{0.34}$ was selected for electrochemical study. $\text{Si}_{0.66}\text{Sn}_{0.34}$ has a relatively low resistivity and shows no evidence for the precipitation of crystalline tin. The bulk of this thesis will be concentrated on the electrochemical, structural, and morphological properties of $\text{Si}_{0.66}\text{Sn}_{0.34}$.

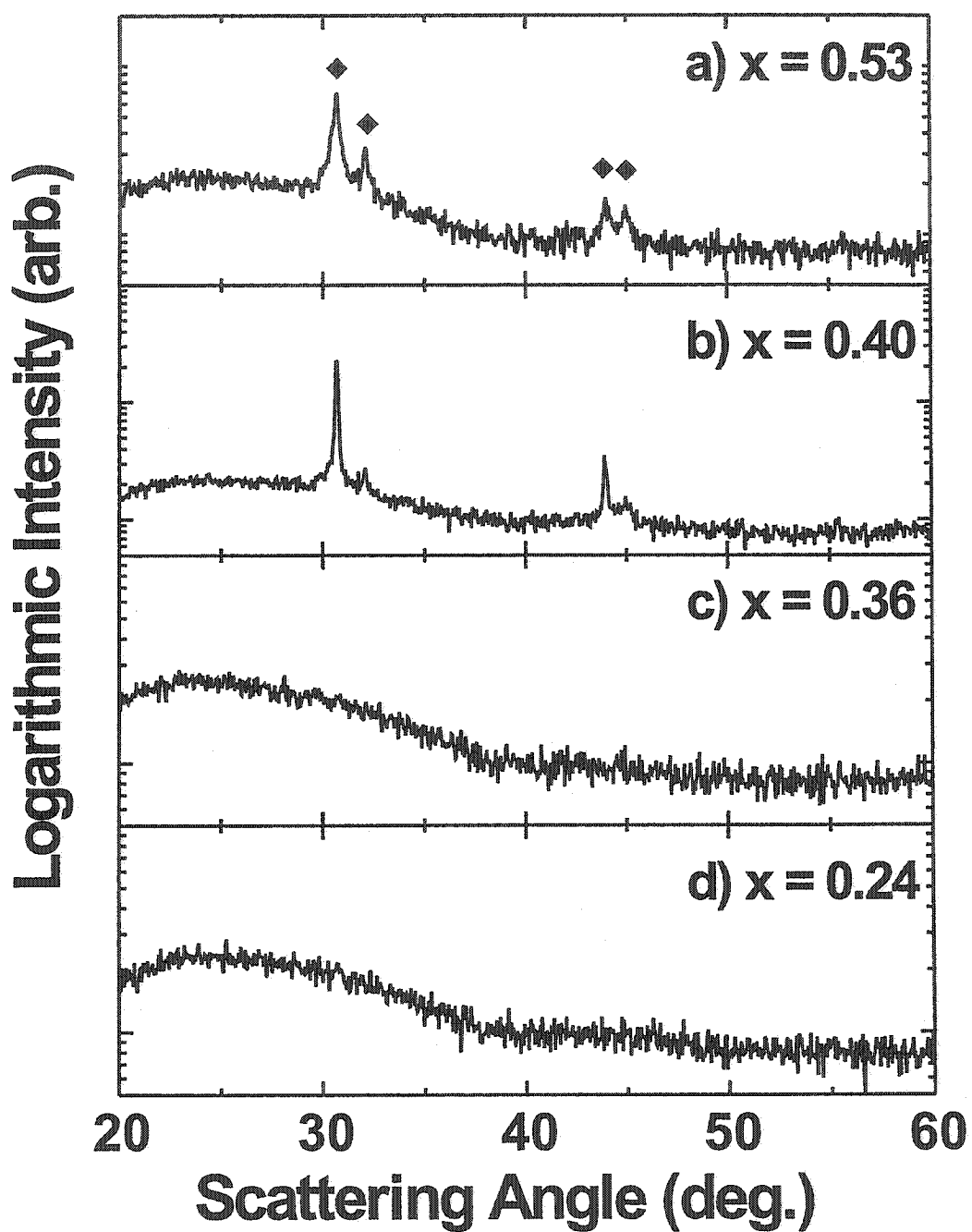


Figure 1.8: X-ray diffraction patterns of $\text{Si}_{1-x}\text{Sn}_x$ for a) $x = 0.53$, b) $x = 0.40$, c) $x = 0.36$, d) $x = 0.24$. The peaks labeled with rhombuses are from crystalline Sn.

Chapter 2

Electrochemical Behavior of Si-Sn Electrodes

In section 1.2 it was shown how Si-Sn samples were synthesized and screened revealing $\text{Si}_{0.66}\text{Sn}_{0.34}$ as the most promising compound. In this chapter we discuss the electrochemical properties of $\text{Si}_{0.66}\text{Sn}_{0.34}$.

2.1 Cycling Behavior of $\text{Si}_{0.66}\text{Sn}_{0.34}$

Figure 2.1 shows the voltage versus capacity of a Li/graphite (2.1a) and Li/ $\text{Si}_{0.66}\text{Sn}_{0.34}$ (2.1b) cell. As can be seen, the capacity of $\text{Si}_{0.66}\text{Sn}_{0.34}$ is vastly superior to that of graphite. Moreover, figure 2.1b shows many qualities of the voltage curve of the Si-Sn electrode. First of all, the voltage curve is smooth and free of plateaus indicating the absence of phase changes occurring in the material during cycling. Also, the cell suffers from a very small irreversible capacity and polarization. Furthermore, the electrode's low potential versus Li metal makes it an excellent candidate as an anode

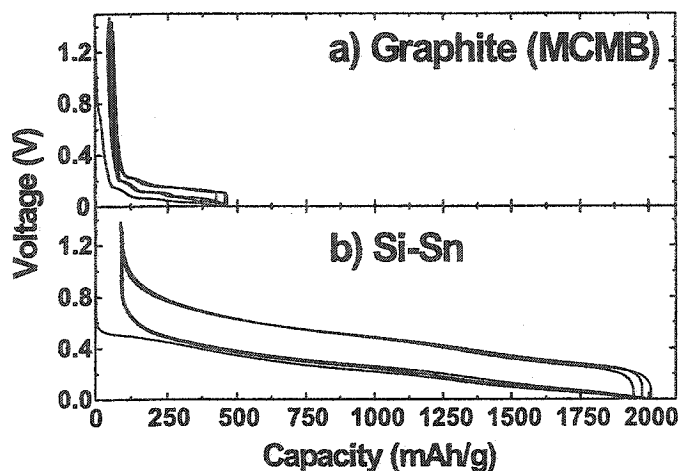


Figure 2.1: Comparison between the voltage versus capacity of a) graphite (mesophase carbon microbeads) and b) $\text{Si}_{0.66}\text{Sn}_{0.34}$

material for commercial lithium-ion batteries. Figure 2.2 shows the capacity retention of $\text{Si}_{0.66}\text{Sn}_{0.34}$ as a function of cycle number for a cell discharged to a cutoff potential of 0.2 V. Few intermetallic electrodes have been shown to exhibit such excellent capacity retention. More often than not, tin-containing electrodes have been shown to give poor capacity retention due to the aggregation of Sn atoms within the electrode material. As larger Sn clusters form with each successive cycle, discrete Li-Sn phases begin to form causing large volume changes and cracking as discussed in section 1.1.

In order to try to understand the excellent cycling behavior of a $\text{Li}/\text{Si}_{0.66}\text{Sn}_{0.34}$ cell, an *in situ* x-ray diffraction analysis was performed.

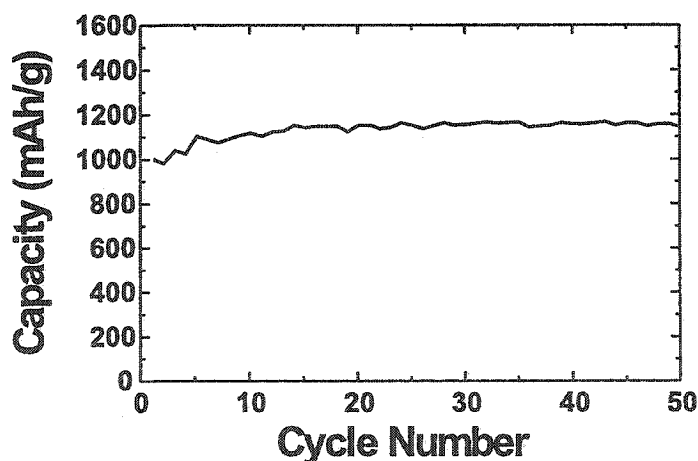


Figure 2.2: Capacity versus cycle number of $\text{Si}_{0.66}\text{Sn}_{0.34}$ cycled versus Li metal at 30 ° C.

2.2 X-Ray Characterization of $\text{Si}_{0.66}\text{Sn}_{0.34}$

Figure 2.3a shows the x-ray diffraction pattern of powdered $\text{Si}_{0.66}\text{Sn}_{0.34}$ prepared in the Randex sputtering system (see Appendix C for the theory of x-ray diffraction). The x-ray diffraction pattern shows the alloy is amorphous as expected based on figure 1.8. In order to more fully understand the structure of this amorphous material, the Debye

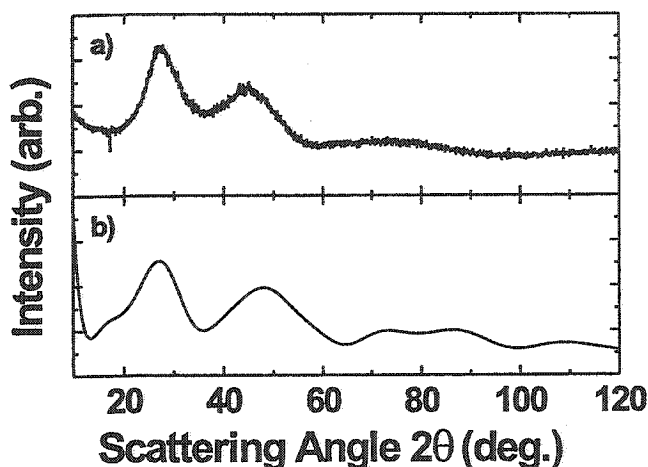


Figure 2.3: a) X-ray diffraction pattern of amorphous $\text{Si}_{0.66}\text{Sn}_{0.34}$ b) Simulated x-ray diffraction pattern of a single Si unit cell (with $a = 5.6 \text{ \AA}$) using the Debye scattering equation.

scattering formalism (see Appendix C) was used to calculate the diffraction pattern of a single Si unit cube containing 18 atoms, eight on the corners [(0,0,0), (1,0,0), (0,1,0), (0,0,1), (1,1,0), (0,1,1), (1,0,1) and (1,1,1)], six on the faces [(1/2,1/2,0), (0,1/2,1/2), (1/2,0,1/2), (1/2,1/2,1), (1,1/2,1/2), (1/2,1,1/2)] and four within the cube at [(1/4,1/4,1/4), (3/4,3/4,1/4), (1/4,3/4,3/4) and (3/4,1/4,3/4)] [55]. The calculated result that best matched the $\text{Si}_{0.66}\text{Sn}_{0.34}$ pattern was obtained when a cube edge of 5.6 \AA was used. This is slightly larger than the accepted value $a = 5.43 \text{ \AA}$ for crystalline Si [55]. The increase is probably a result of the larger Sn atoms incorporated substitutionally into amorphous Si (*a*-Si). Although not rigorous,

this Debye calculation suggests that $\text{Si}_{0.66}\text{Sn}_{0.34}$ has a short-range ordered diamond structure, similar to α -Si [56].

Figure 2.4 shows the *in situ* x-ray diffraction results collected during the first discharge cycle of a $\text{Li}/\text{Si}_{0.66}\text{Sn}_{0.34}$ cell. The cell was discharged at 19.7 mA/g (C/96 or 0.15 mA/cm²) to 0.2 volts for the first cycle. The voltage versus capacity curve for the cell collected during the experiment is shown in panel 2.4e. The maximum capacity of 860 mAh/g obtained for the first discharge represents approximately 2 Li atoms per $\text{Si}_{0.66}\text{Sn}_{0.34}$ formula unit. Some of the x-ray diffraction patterns collected during the first discharge cycle are shown in order from top to bottom in panels 2.4a to 2.4d. Each x-ray diffraction pattern took 2 hours to collect. The sharp peaks in the diffraction pattern are due to various cell parts. The solid dots on the voltage curve (2.4e) show the starting position at which each x-ray scan shown in panels 2.4 a-d were collected. Figures 2.4 a-d show that the x-ray diffraction pattern of the electrode develops broad peaks at $2\theta \approx 23^\circ$ and $2\theta \approx 40^\circ$ during the insertion of lithium.

The change in the 23° peak can more clearly be seen in figure 2.5a where the x-ray diffraction pattern at the bottom of discharge (dark line) is compared to the x-ray diffraction pattern of the fresh cell (light line). Displaying the two curves together shows the existence of the broad peak. The broad peaks observed in this work have often been observed in other Li-Sn-containing intermetallics and have been explained in [57] by the local structure found in $\text{Li}_{22}\text{Sn}_5$ (or isostructural $\text{Li}_{22}\text{Si}_5$). In this structure, Sn atoms are arranged locally on the corners of tetrahedra that have edges 3.3 Å long.

The results from the first charge of the same $\text{Li}/\text{Li}_x\text{Si}_{0.66}\text{Sn}_{0.34}$ cell are shown in figure 2.6. As lithium is removed from the electrode, the broad peaks (panels 2.6

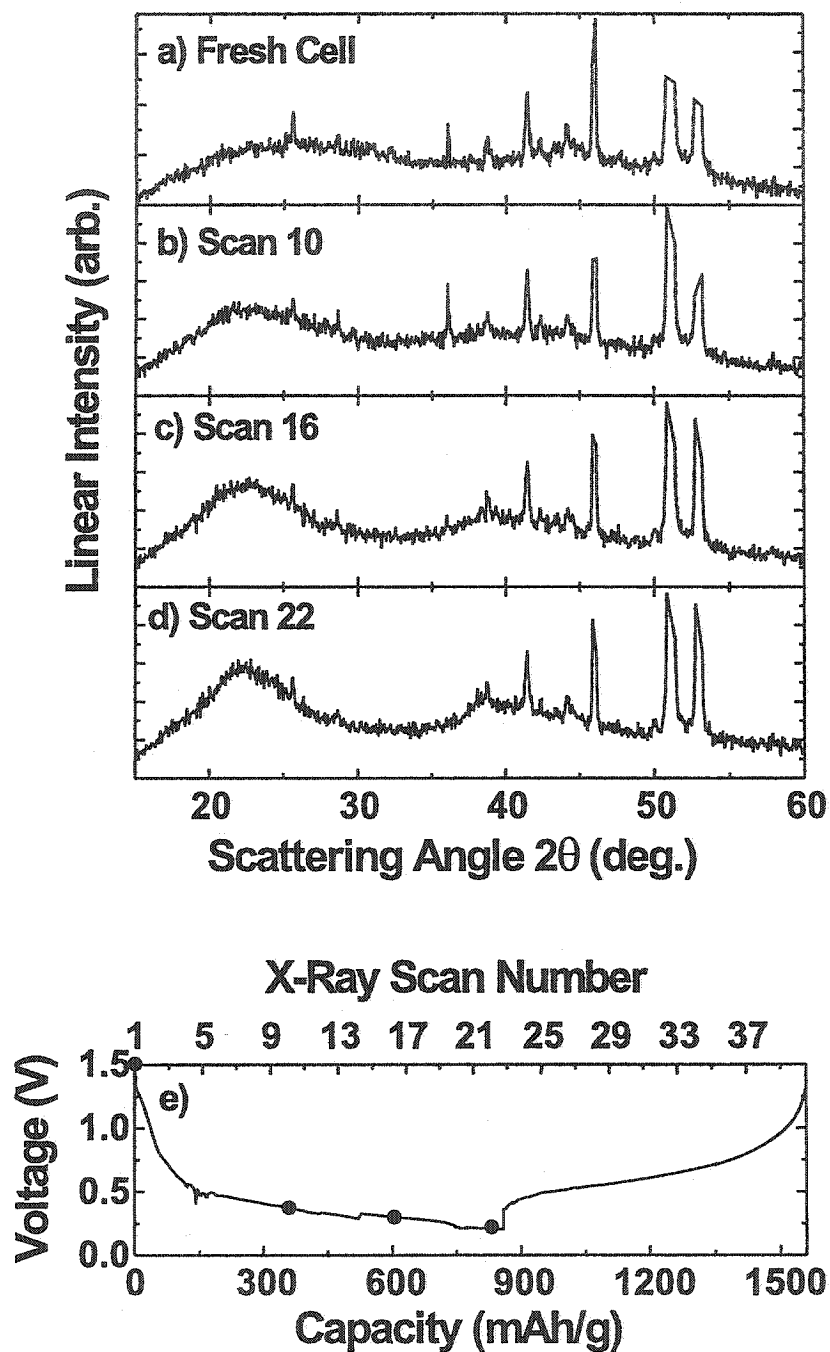


Figure 2.4: (a-d) *In situ* x-ray diffraction patterns collected during the first discharge cycle of a $\text{Si}_{0.66}\text{Sn}_{0.34}$ electrode cycled against Li metal discharged to 0.2 V. The sharp peaks in the diffraction patterns come from various cell parts. (e) Voltage versus capacity (bottom abscissa) and x-ray scan number (top abscissa) collected during the experiment. The black dots on the voltage curve show where the x-ray scans began.

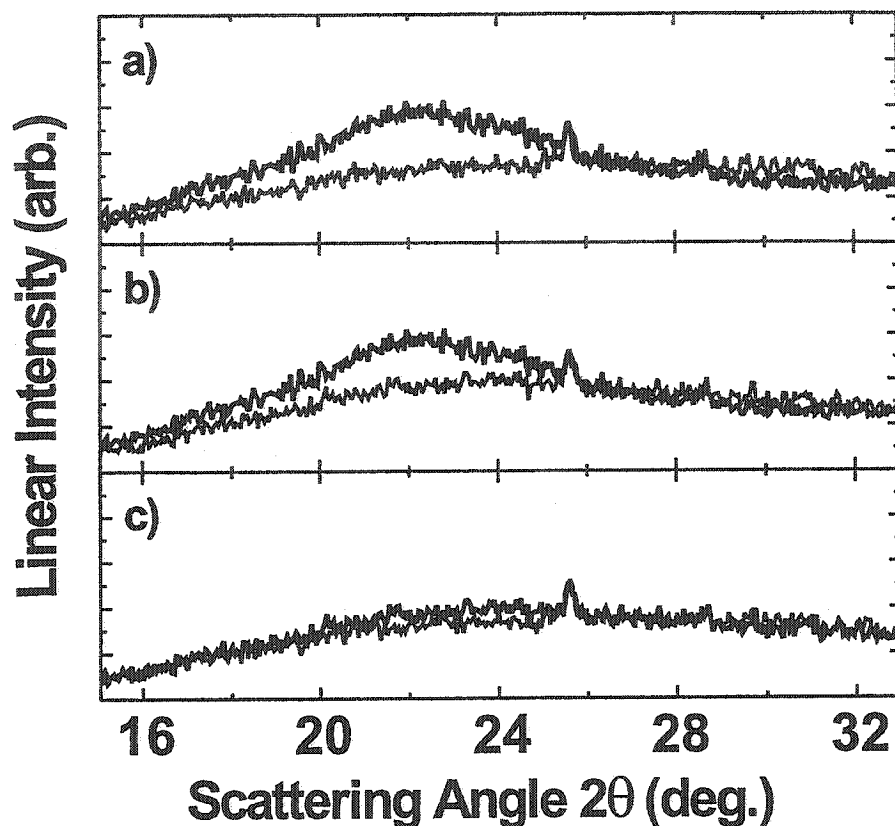


Figure 2.5: a) Comparison between the x-ray diffraction pattern of the fresh cell (light line) and the fully discharged cell (dark line). b) Comparison between the x-ray diffraction pattern of the fully discharged cell (dark line) and the fully charged cell (light line). c) Comparison between the x-ray diffraction pattern of the fresh cell (light line) and the fully charged cell (dark line).

a-d) slowly disappear until the x-ray diffraction pattern of the electrode at the top of the first charge cycle resembles the x-ray diffraction pattern of the fresh cell. Figure 2.5b shows the x-ray diffraction pattern of the electrode at the bottom of the first discharge cycle (dark line) and the top of the first charge cycle (light line). More importantly, figure 2.5c shows a comparison between the x-ray diffraction pattern of

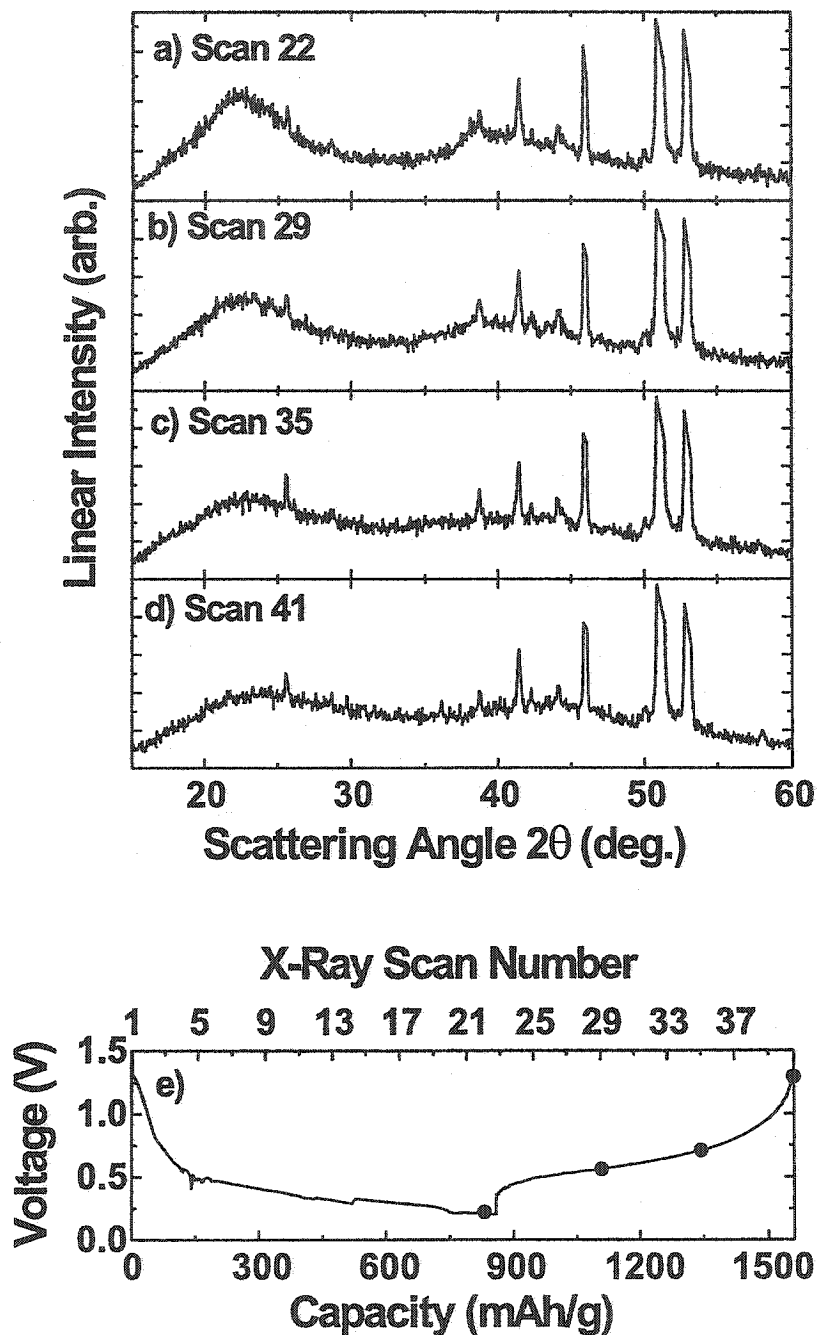


Figure 2.6: (a-d) *In situ* x-ray diffraction patterns collected during the first charge cycle of a $\text{Si}_{0.66}\text{Sn}_{0.34}$ electrode cycled against Li metal charged to 1.3 V. The sharp peaks in the diffraction patterns come from various cell parts. (e) Voltage versus capacity (bottom abscissa) and x-ray scan number (top abscissa) collected during the experiment. The black dots on the voltage curve show where the x-ray scans began.

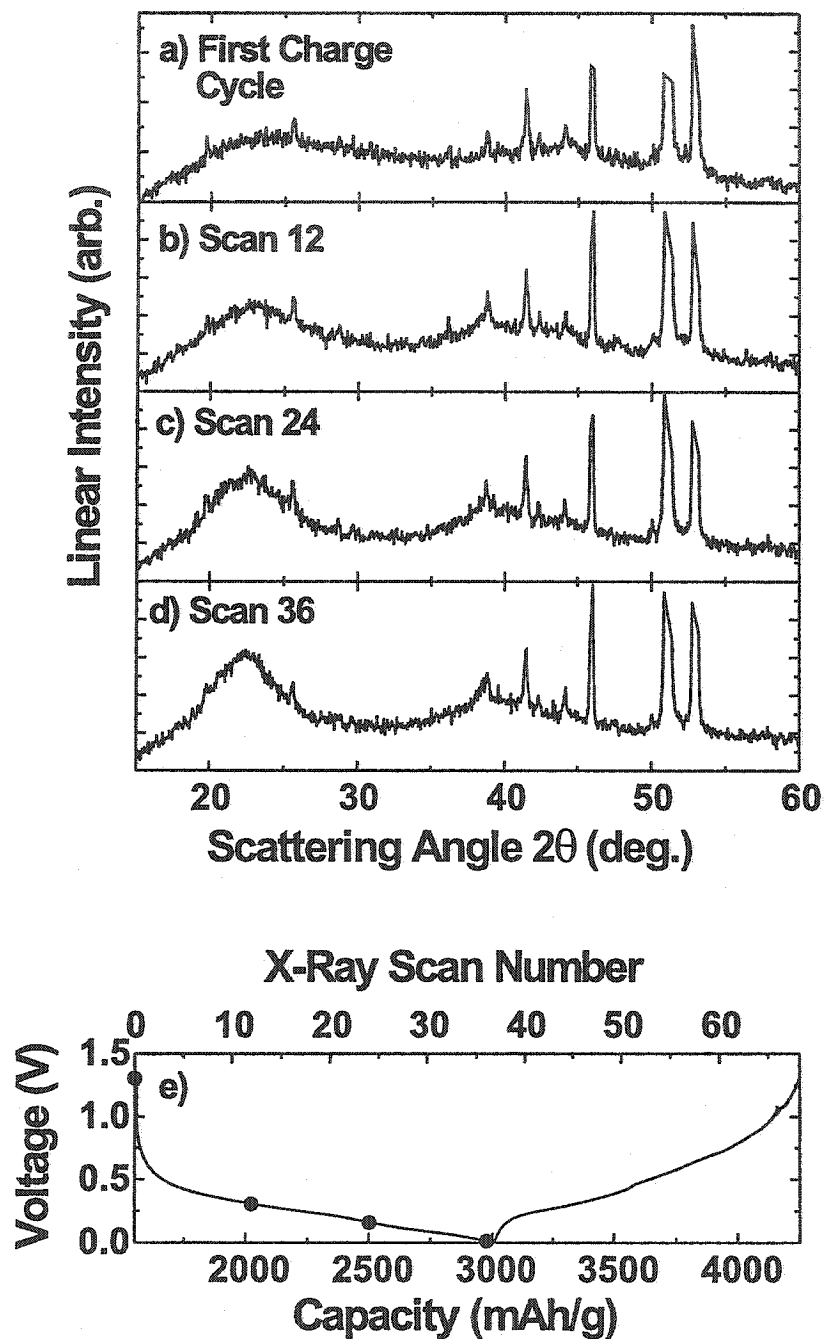


Figure 2.7: (a-d) *In situ* x-ray diffraction patterns collected during the second discharge cycle of a $\text{Si}_{0.66}\text{Sn}_{0.34}$ electrode cycled against Li metal to 0.0 V. The sharp peaks in the diffraction patterns come from various cell parts. (e) Voltage versus capacity (bottom abscissa) and x-ray scan number (top abscissa) collected during the experiment. The black dots on the voltage curve show where the x-ray scans began.

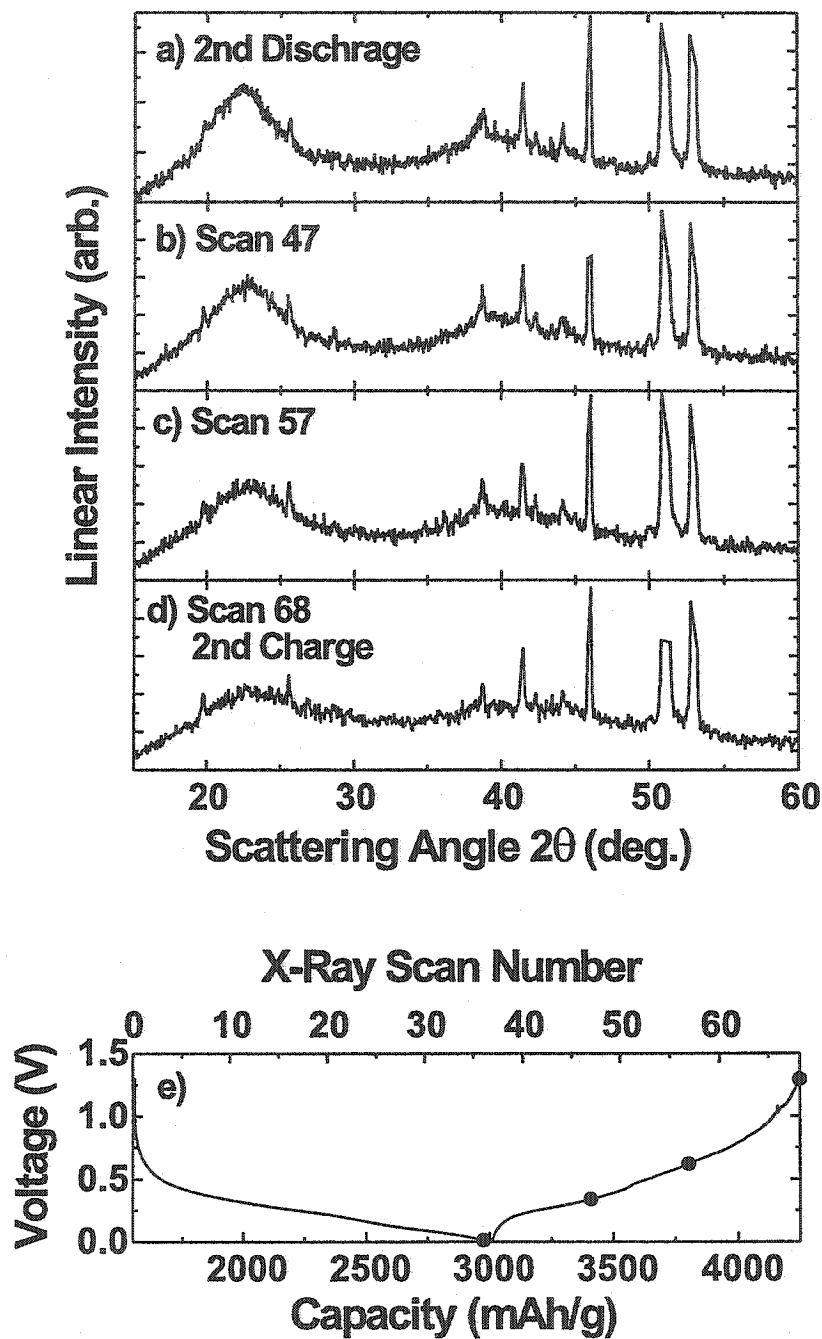


Figure 2.8: (a-d) In situ x-ray diffraction patterns collected during the second charge cycle of a $\text{Si}_{0.66}\text{Sn}_{0.34}$ electrode cycled against Li metal charged to 0.0 V. The sharp peaks in the diffraction patterns come from various cell parts. (e) Voltage versus capacity (bottom abscissa) and x-ray scan number (top abscissa) collected during the experiment. The black dots on the voltage curve show where the x-ray scans began.

the fresh cell (light line) and the x-ray diffraction pattern of the electrode at the top of the first charge cycle (dark line). Little difference is observed between the patterns in figure 2.5c showing that the electrode returns to approximately the starting state.

In this same experiment *in situ* x-ray diffraction patterns were collected for the second cycle where this time the cell was discharged to 0.0 V (approximately $x = 4$ in $\text{Li}_x\text{Si}_{0.66}\text{Sn}_{0.34}$). The results for the second discharge and charge cycle are shown in figures 2.7 and 2.8 respectively. The same gradual increase in broad peaks at $2\theta \approx 23^\circ$ and $2\theta \approx 40^\circ$ (figures 2.7 b-d) are observed during the discharge. The 23° peak (shown in figure 2.7) becomes more intense than the corresponding peak formed during the first discharge cycle (to 0.2 V) shown in figure 2.4d presumably due to the larger amount of lithium added to the sample. Figures 2.8 a-d show that as lithium is again removed from the electrode the 23° and 40° peaks slowly disappear.

The x-ray diffraction pattern observed at 0.0 V (figure 2.7d) is very similar to that found during the room temperature lithiation of Sn at the same potential [36]. Figure 2.9 shows a comparison between the x-ray diffraction pattern of a fully discharged $\text{Si}_{0.66}\text{Sn}_{0.34}$ electrode (figure 2.9a), and a simulated x-ray diffraction pattern of a Li-Sn tetrahedron (figure 2.9b). Such local tetrahedral arrangements of Sn atoms are found in $\text{Li}_{22}\text{Sn}_5$ and $\text{Li}_{22}\text{Si}_5$, where a Li atom is at the center of the tetrahedron and Sn or Si atoms are at the four corners. The edge length of the tetrahedron was taken to be 3.3 \AA , approximately the same as the nearest neighbor Sn-Sn distance in $\text{Li}_{22}\text{Sn}_5$. The similarities between the two diffraction patterns are striking suggesting that the local arrangements of Si and Sn atoms are similar to the local arrangements found in $\text{Li}_{22}\text{Sn}_5$ and $\text{Li}_{22}\text{Si}_5$.

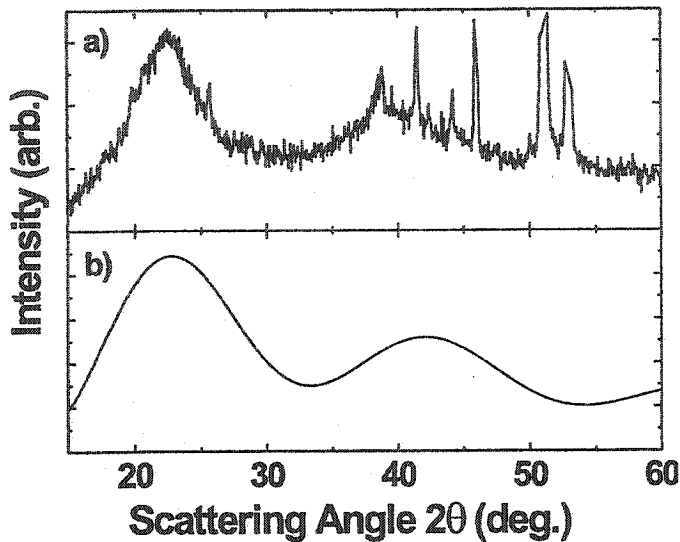


Figure 2.9: Comparison between a) the x-ray diffraction pattern of a fully discharged $\text{Si}_{0.66}\text{Sn}_{0.34}$ electrode and b) a simulated x-ray diffraction pattern of a Li-Sn tetrahedron.

Figure 2.10 shows by x-ray diffraction that the starting $\text{Si}_{0.66}\text{Sn}_{0.34}$ (dark line) material is structurally different from the final lithiated material, $\text{Li}_{4.4}\text{Si}_{0.66}\text{Sn}_{0.34}$ (light line). However, the intermediate diffraction patterns in figures 2.4, 2.6, 2.7 and 2.8 appear by eye to be made up of a fraction of the pattern from the first scan of the cell (figure 2.4a) and a fraction of the pattern from the electrode at 0 V (figure 2.7 d). In order to more fully examine this idea, we represented an arbitrary scan of the electrode in the cell, $Y_n(m)$ as a sum:

$$Y_n^{calc}(m) = (1 - z)Y_{FC}(m) + zY_{0V}(m), \quad (2.1)$$

where $Y_n^{calc}(m)$ is the calculated m^{th} data point of the n^{th} scan, $Y_{FC}(m)$ is the m^{th} data point of the Fresh Cell scan (figure 2.4a), $Y_{0V}(m)$ is the m^{th} data point of the scan at 0 V (figure 2.7d) and z is a number between 0 and 1. The index, m , runs from

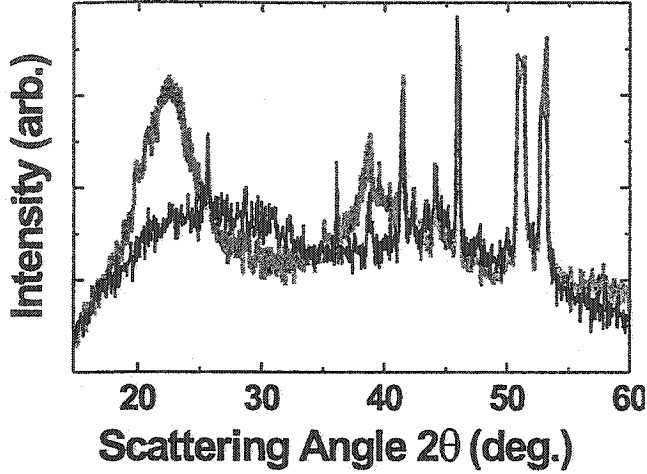


Figure 2.10: Comparison between the x-ray diffraction pattern of the fresh cell (dark line) and the fully discharged cell (0.0 V) (light line), corresponding to $\text{Li}_{4.4}\text{Si}_{0.66}\text{Sn}_{0.34}$.

1 to M , where M is the number of data points in each scan, in this case 900. The goodness of fit, χ^2 , defined as:

$$\chi^2 = \frac{1}{M} \sum_{m=1}^M \frac{Y_n(m) - Y_n^{calc}(m)}{Y_n(m)}, \quad (2.2)$$

was then minimized (using the solver feature of Microsoft Excel) by changing z .

Figure 2.11 shows some fits to data sets based on this approach. For example, figure 2.11a shows that scan 11 of the first discharge is well fitted with $z = 0.56$, figure 2.11c shows that scan 22 of the first discharge (figure 2.4d) is well fitted with $z = 0.88$, and figure 2.11e shows that scan 31 of the first cycle, during charge, is well fitted with $z = 0.60$. For the second cycle, figure 2.12a shows that the first scan of the second discharge (scan 41 overall) is well fitted with $z = 0.18$, figure 2.12c shows that scan 18 of the second discharge (scan 58 overall) is well fitted with $z = 0.67$ and figure 2.12e shows that scan 51 (scan 92 overall) of the second cycle, during charge,

is well fitted with $z = 0.75$. In fact, almost all the scans can be fitted well by this approach as we show below.

Figure 2.13a shows the cell potential versus scan number, n , for the first two cycles, figure 2.13b shows χ^2 versus n and figure 2.13c shows both z and $1 - z$ versus n . Since we are fitting a data set with random statistical noise by the linear combination of two other data sets having random statistical noise, a “perfect” fit will have $\chi^2 = 2$. (If a data set with random statistical noise is fitted to a noise-free calculation, then it is well known that a “perfect” fit will have $\chi^2 = 1$. In our case, a perfect fit has $\chi^2 = 2$ because the calculated curve and the data set both have statistical noise). Figure 2.13b shows that the fits give χ^2 near 2 for most of the data sets proving that all scans can be well represented by a linear combination of the scan from the fresh cell and the scan from the fully discharged cell.

Figure 2.13c shows that as x in $\text{Li}_x\text{Si}_{0.66}\text{Sn}_{0.34}$ increases, the diffraction pattern shows more and more evidence of the local structure found in $\text{Li}_{4.4}\text{Sn}$ or $\text{Li}_{4.4}\text{Si}$, since z increases when x increases. When the lithium is removed from the electrode, the diffraction pattern reverts to that characteristic of the local structure found in the diamond lattice. The variation of z and $1 - z$ with scan number, or x , is not perfectly linear. For example, there is a region in figure 2.13c near the start of the experiment, when z does not change appreciably for the first 3 scans. This may indicate that either the transferred lithium is consumed by irreversible surface reaction and is not incorporated into the host, or that the transferred lithium is incorporated uniformly interstitially within the diamond-like $\text{a-Si}_{0.66}\text{Sn}_{0.34}$ structure without causing significant bond rearrangements as found in $\text{Li}_{4.4}\text{Sn}$. In the range from scans 60 to 78 in figure 2.13c, the variation of z with scan number slows. The

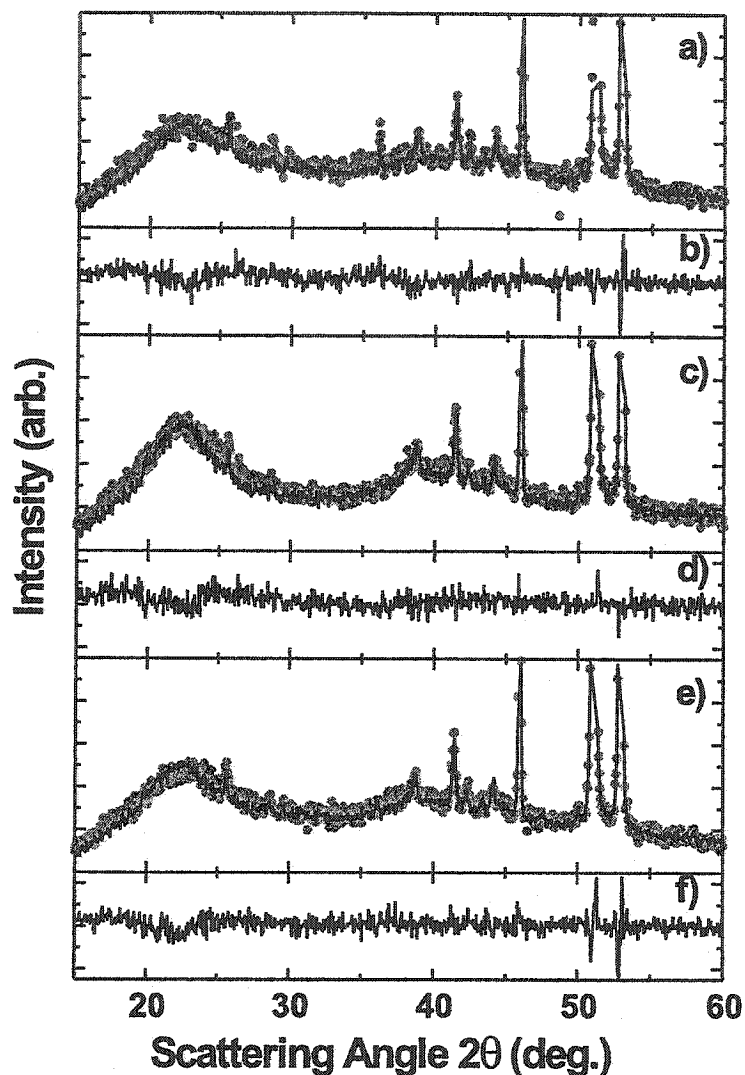


Figure 2.11: a) Solid grey dots show the x-ray diffraction pattern of scan 11 of the first discharge cycle while the solid line shows the fit to the data set using a linear combination of the first scan and the scan taken at 0.0 V corresponding to $\text{Li}_{4.4}\text{Si}_{0.66}\text{Sn}_{0.34}$. b) Difference between scan 11 and the linear combination. c) Solid grey dots show the x-ray diffraction pattern of scan 22 of the first discharge cycle while the solid line shows the linear combination d) Difference between scan 22 and the linear combination. e) Solid grey dots show the x-ray diffraction pattern of scan 31 of the first charge cycle while the solid line shows the linear combination f) Difference plot between scan 31 and the linear combination.

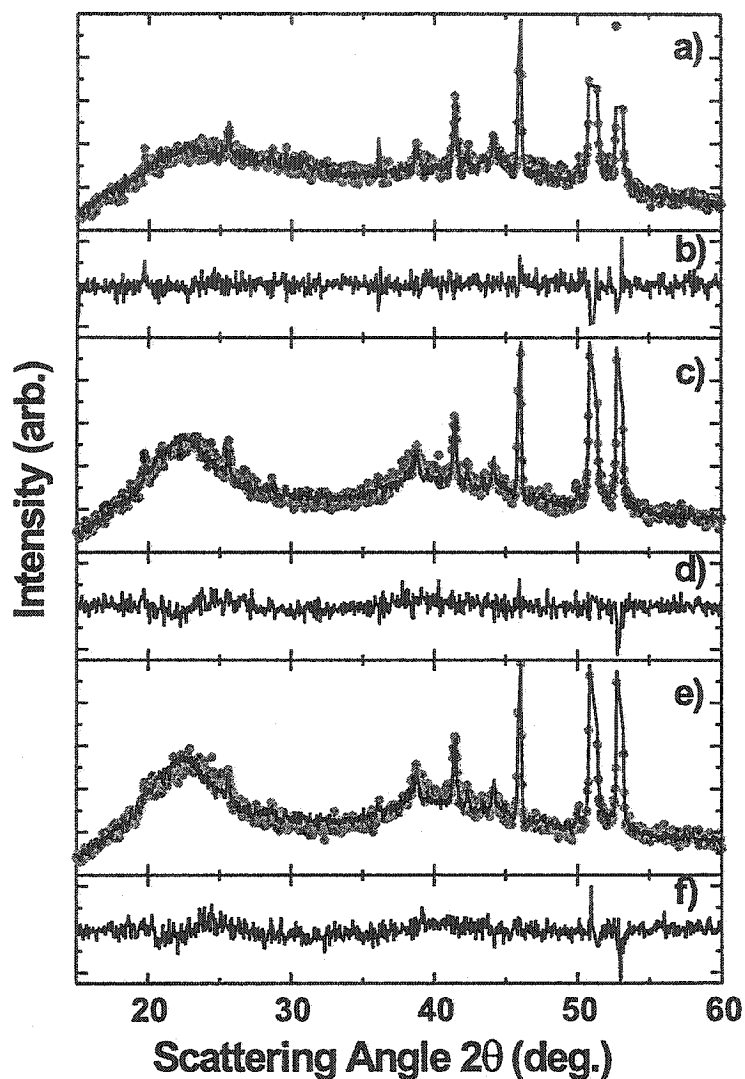


Figure 2.12: a) Solid grey dots show the x-ray diffraction pattern of scan 1 (scan 41 overall) of the second discharge cycle while the solid line shows the linear combination b) Difference between scan 1 and the linear combination. c) Solid grey dots show the x-ray diffraction pattern of scan 18 (scan 58 overall) of the second discharge cycle while the solid line shows the linear combination d) Difference between scan 18 and the linear fit. e) Solid grey dots show the x-ray diffraction pattern of scan 51 (scan 92 overall) of the second charge cycle while the solid line shows the linear combination f) Difference between scan 51 and the linear combination.

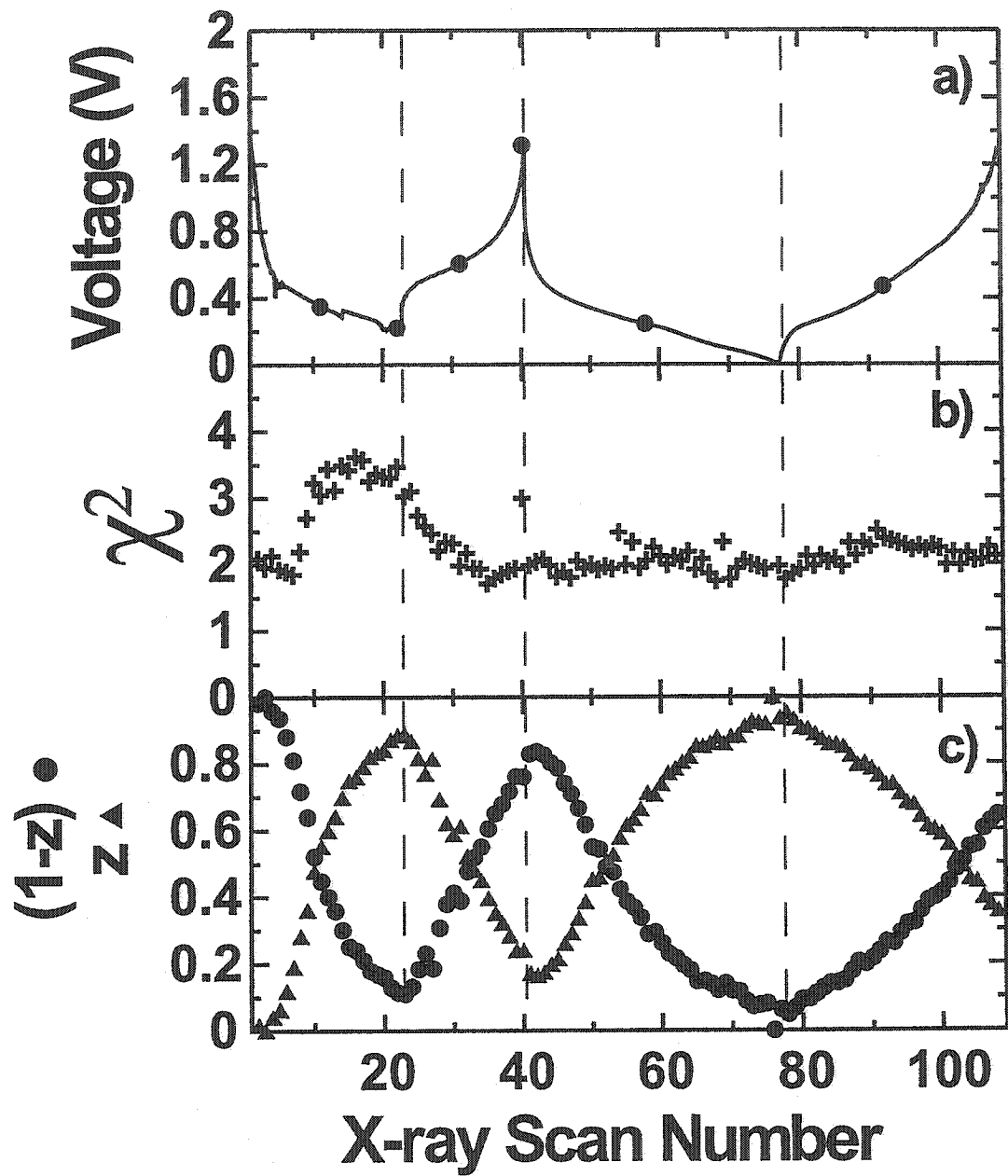


Figure 2.13: (a) Solid line shows the voltage versus x-ray scan number. Solid dots show the position of the x-ray diffraction patterns highlighted in figures 2.11 and 2.12. (b) Goodness of fit χ^2 as calculated by equation 2 versus x-ray scan number. (c) Numerical value of $(1-z)$ (circles) and z (triangles) of equation 1 versus x-ray scan number.

local structure of Sn and Si atoms found in $\text{Li}_{4.4}\text{Sn}$ or $\text{Li}_{4.4}\text{Si}$ may be predominantly formed at smaller lithium concentrations (say near $x = 2.5$) and hence z would approach 1 as observed. Adding further lithium would not impact the diffraction pattern significantly since its scattering power is small, if the correct local arrangement of Si and Sn atoms has already been established.

This *in situ* x-ray diffraction experiment clearly shows the room temperature electrochemical reaction of Li with this $\text{Si}_{0.66}\text{Sn}_{0.34}$ electrode proceeds via a relatively benign exchange reaction of the local environment of $\text{Si}_{0.66}\text{Sn}_{0.34}$ for the local environment of $\text{Li}_{4.4}\text{Si}_{0.66}\text{Sn}_{0.34}$. Since the material remains amorphous at all times during cycling and since there are no plateaus in the voltage-capacity plot it can only be assumed that these two local environments are distributed evenly throughout the bulk of the material. This reaction mechanism is perhaps the main factor contributing to the favorable cycling performance of this compound.

Finally, now that the reaction process is understood, it is possible to make some statements about the origin of the hysteresis between charge and discharge displayed in figure 2.1b. Figure 2.14 shows the voltage versus capacity for two $\text{Si}_{0.66}\text{Sn}_{0.34}$ cells cycled at 55°C (solid line) and 30°C (dashed line) at different current densities. In order to see the hysteresis more clearly, the voltage curves have been normalized to the same capacity during charge and discharge. The true discharge capacity has been plotted, and the charge curve has been scaled to have the same capacity. From this data, the difference in the average voltage between the charge and discharge cycle was measured for each charge cycle. The average voltage between the discharge/charge curves, or in other words the hysteresis, is plotted in figure 2.15 against the specific current.

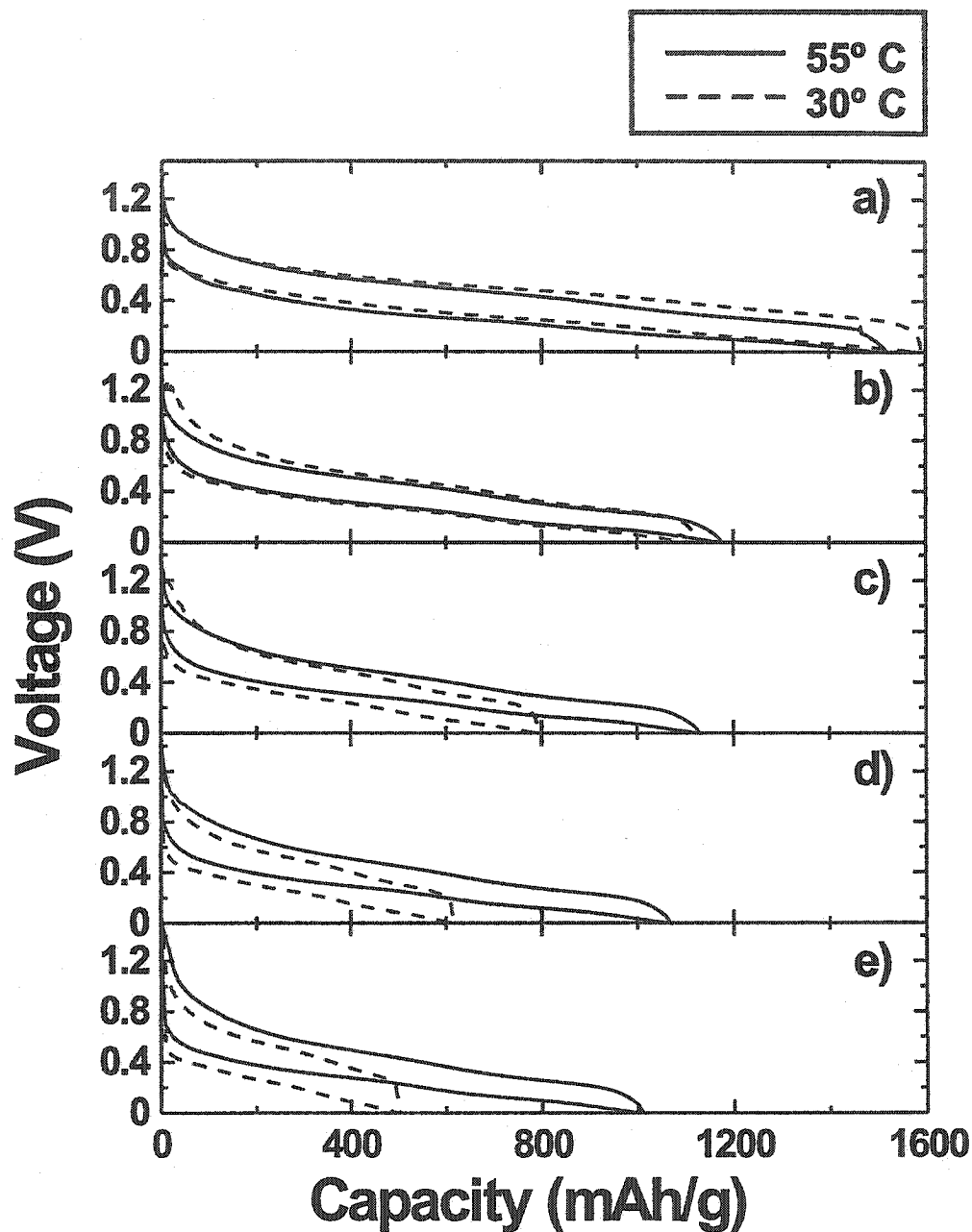


Figure 2.14: Graph of voltage versus capacity of two cells cycled at 55°C (solid line) and 30°C (dashed line). All voltage curves have been normalized. (a) Specific current of the 55°C cell is 14.3 mA/g and the specific current of the 30°C cell is 16 mA/g. (b) Specific current of the 55°C cell is 28.6 mA/g and the current density of the 30°C cell is 33 mA/g. (c) Specific current of the 55°C cell is 57 mA/g and the specific current of the 30°C cell is 66 mA/g. (d) Specific current of the 55°C cell is 114.3 mA/g and the specific current of the 30°C cell is 133 mA/g. (e) Specific current of the 55°C cell is 228.6 mA/g and the specific current of the 30°C cell is 266 mA/g.

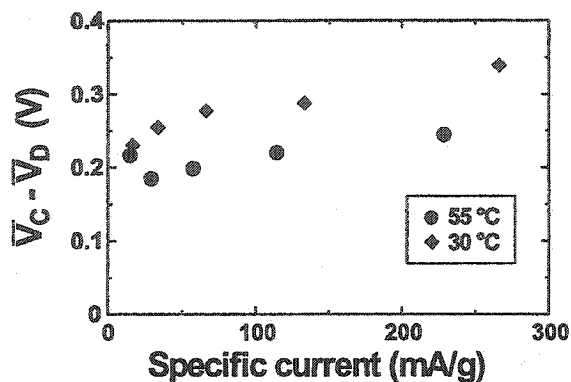


Figure 2.15: Difference between average charge and discharge potentials ($\bar{V}_C - \bar{V}_D$) versus specific current of two cells cycled at 55°C (circles) and 30°C (rhombuses).

As expected, the hysteresis of the 55°C cell (circles) is less than the hysteresis of the cell cycled at 30°C (rhombuses). The hysteresis of the cells does not approach zero as the current density approaches zero. Therefore, the hysteresis is inherent and the area between the charge and discharge curves represents the energy dissipated during one charge-discharge cycle. We speculate that the energy is dissipated by the changes in the local atomic environment around the host atoms that involve the breaking and creation of new bonds involving the host atoms and lithium.

Using the results in figures 2.14 and 2.15, we can estimate the magnitude of the energy dissipated by the hysteresis. Figure 2.15 shows that the offset between charge and discharge is about 0.2 V. Figure 2.14a, for the lowest charge-discharge rate, gives a capacity of about 4 Li atoms per $\text{Si}_{0.66}\text{Sn}_{0.34}$. Using equation 1.1 we can calculate the hysteresis energy to be about 0.8 eV per $\text{Si}_{0.66}\text{Sn}_{0.34}$ formula unit. Since chemical bonds generally have energies on the order of a few eV per bond, we feel that the measured energy is consistent with a change in the local environment of the Si and Sn atoms.

In this chapter we have shown by electrochemical and *in situ* x-ray diffraction

experiments how the reaction of Li with $\text{Si}_{0.66}\text{Sn}_{0.34}$ occurs via the exchange of two local environments. Since this material remains amorphous at all times during cycling and since the voltage profile is smooth, it can only be assumed that the two local environments are distributed evenly throughout the bulk of the material. This reaction mechanism is believed to be the reason that $\alpha\text{-Si}_{0.66}\text{Sn}_{0.34}$ can undergo reversible cycling over many discharge charge cycles without significant capacity loss.

Chapter 3

Introduction to Atomic Force Microscopy

Since its invention in 1986 [58], the atomic force microscope (AFM) has become an essential tool in materials science. AFMs can be used to study various materials from conductors to insulators in different media ranging from ultra high vacuum to liquid [59, 60, 61, 61]. AFMs have also been used to study chemical reactions such as corrosion of metals and electroplating [62, 63].

3.1 Working of an AFM

Figure 3.1 shows a schematic representation of an atomic force microscope. The central component of an AFM is the piezo electric tube (3.1a) [64], which is responsible for moving the nanoprobe (3.1b) over the surface of the sample (3.1c). During imaging, the deflection of the cantilever on the nanoprobe is detected by an optical system. A laser beam from a diode laser (3.1d) is incident on the back of the cantilever

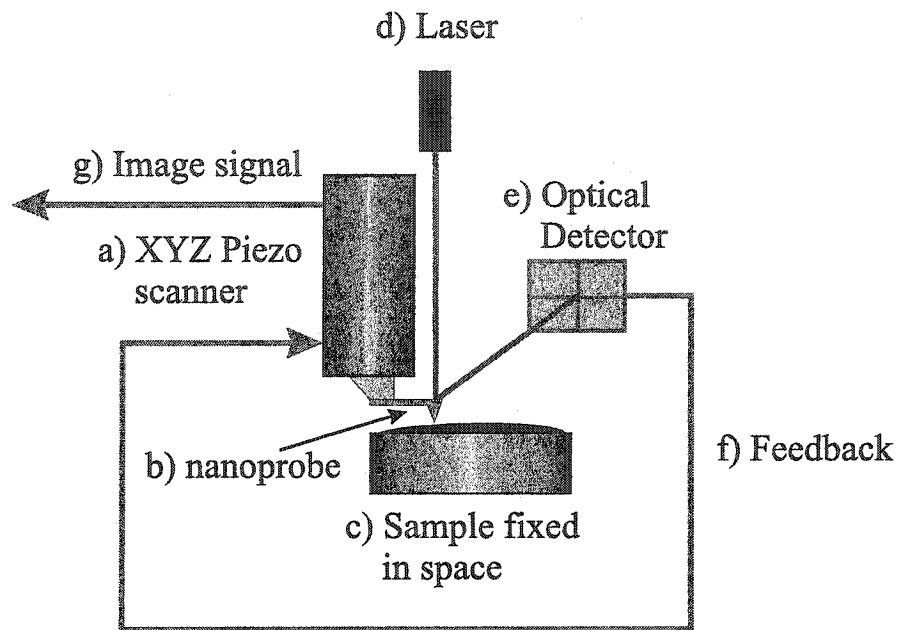


Figure 3.1: Schematic representation of an atomic force microscope.

and is reflected into a position-sensitive optical detector (3.1e). The signal obtained by the optical detector is then sent to the piezo scanner by means of a feedback loop (3.1f). The signal is then used by the scanner by a method dependent on the imaging technique employed¹. The final signal (3.1g) obtained from the piezo scanner is then sent to a computer where it is interpreted to construct the image.

The nanoprobes (Digital Instruments, Santa Barbara, Ca.) used in our experiments are shown in figure 3.2. The type of nanoprobe used is highly dependent on the imaging technique used during the analysis. The nanoprobes shown in figure 3.2 are V-shaped and are used mostly for imaging in contact mode. The nanoprobes are

¹As an example, while imaging in constant force contact mode, the signal from the optical detector is used to either elongate or contract the piezo in order to maintain a constant force of the cantilever on the sample.

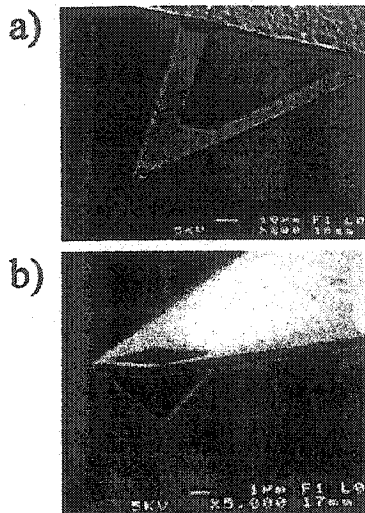


Figure 3.2: a) SEM image of a contact mode V-shape cantilever. b) SEM image of the pyramid-shaped tip under the cantilever.

made from Si_3N_4 and are gold-coated on the top to improve the reflectivity. The pyramidal tip under the cantilever is approximately $3.5 \mu\text{m}$ deep with a 35° half angle and a 5 to 40 nm radius at the apex. One of the most important parameters of these cantilevers is the spring constant. Due to its importance, many groups have attempted to calculate the spring constant from the geometry [65, 66, 67, 68, 69] while others have proposed experimental procedures [70, 71, 72, 73, 74, 75, 76, 77, 78]. For the cantilevers used in our work, the spring constant ranges, according to the manufacturer, from 0.58 to 0.06 N/m.

Today's AFM can be used to perform a multitude of tasks including surface imaging, force sensing, friction analysis and many more. In all of our experiments, the only imaging method used was *constant force contact mode*. In the next section, this imaging method will be discussed and other techniques will also be highlighted.

3.1.1 Contact Mode

The simplest imaging technique used in atomic force microscopy is *contact mode*. There are two types of imaging techniques that fall under the category of *contact mode*. The first one, which is the less common of the two, is called *constant height contact mode*. In this method, the height of the piezo is kept constant as it rasters over the surface of the sample. The change in height of the sample is detected by the deflection of the cantilever. Because the maximum deflection of the cantilever is small, this method is largely limited in the direction perpendicular to the sample, it is used almost exclusively for imaging at atomic resolution.

The second type of contact mode imaging is *constant force contact mode*. In this method, the force of the cantilever on the sample is kept constant by a continual readjustment of the piezo scanner. More precisely, as the scanner rasters over the sample, the changes in topography of the surface are registered instantly by a small deflection of the cantilever. When this deflection is observed by the optical detector, it sends a signal to the piezo scanner instructing it to change its length in order to restore a constant force of the cantilever on the sample. During the imaging process two images are collected: the topograph and the deflection image. The topograph image represents the AFM's interpretation of surface of the sample. This is done by converting the voltage used to elongate or contract the piezo to the distance by which the piezo moved. The deflection image gives the instantaneous deflection of the cantilever which can be interpreted as the error of the topograph. In the results presented in this thesis, only topographic images are shown.

3.1.2 Other imaging Techniques

There are many other imaging techniques practiced by atomic force microscopists. Among these, one of the most widely used is *tapping mode* or *intermediate contact mode*. In this method, as the scanner sweeps over the surface, the tip is made to tap the surface repeatedly. Since the tip is never in contact with the surface at a single point for more than an instant, there is no or little possibility for the tip to affect the surface under study. For this reason, tapping mode is used to image soft materials such as polymers and even bacteria. [79, 80, 81]

Another technique used is known as *lateral force microscopy* or simply LFM. This method is used to study the frictional forces between the AFM tip and the surface. This is done by monitoring the torque produced on the tip while it drags laterally over a surface. To study the interaction between different surfaces, it is possible to change the chemistry of the AFM tip.

As stated earlier, there are many other imaging techniques which can be used with an AFM. Therefore, instead of continuing this survey, the reader is simply referred to the following excellent references on atomic force microscopy [82, 83, 84, 85]

3.1.3 Imaging Artifacts

Imaging artifacts are a constant plague for atomic force microscopists. For this reason, a short outline of imaging artifacts is given below.

Tip Artifacts

Depending on the manufacture, AFM cantilevers (including the tip) can have different sizes, shapes and compositions. Despite this, tip artifacts are always present in AFM

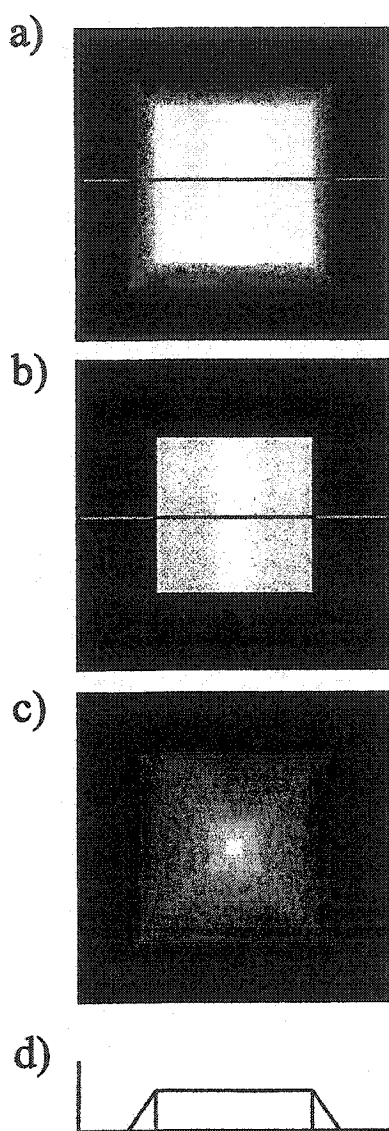


Figure 3.3: a) Numerical simulation of an AFM image of a b) square surface of constant height. Image was calculated with a c) pyramidal tip not shown to scale. d) Cross section of the image and surface shows the edges produced by the finite size of the tip.

images. The main tip artifact is due to the finite size of the tip. More precisely, each AFM topograph is a convolution of the actual surface of the sample and the shape of the tip (This is a generalization, as we will see in the next section. There are other artifacts that influence the final AFM image). Since it is not possible to show an example of an AFM image where the finite shape of the tip is the only artifact, we show a theoretical example. Figure 3.3a shows the results obtained from imaging

a single square step (3.3b) with a perfect pyramidal tip (3.3c). As can be seen, the image produced shows the effect of the shape of the tip. This can more clearly be seen in the cross-section shown in figure 3.3d. The tip displayed in figure 3.3c is not shown to scale. For the calculations, realistic values were used for both the tip shape and surface.

Other tip artifacts which can occur are due to damaged or imperfect tips. Figure 3.4 shows what is sometimes known as the double image effect. This occurs when

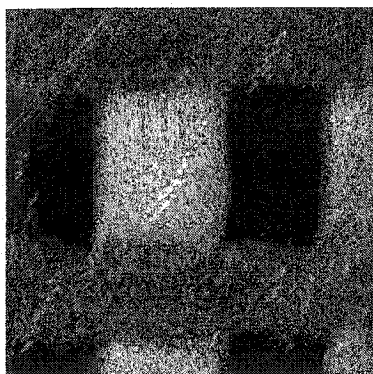


Figure 3.4: Effect known as double imaging produced by a defected tip with two minima. Image is $24 \times 24 \mu\text{m}$ in size. The vertical contrast scale from dark to light is 0 - 118 nm.

the tip has two distinct minima which both participate in the imaging process. The end result, as can be seen in figure 3.4, is a superposition of two images which are displaced by the distance between the two minima of the tip.

Scanner Artifacts

In the first AFMs, the cantilever was mounted below the intersection of three mutually perpendicular piezos. In more modern microscopes, the scanner has been replaced by a hollow tube piezoelectric ceramic with four metal plates on the outside and one metal plate on the inside, as shown systematically in figure 3.5a [64]. A piezoelectric material contains regions which carry a net dipole moment all pointing in the same direction. In order to make the piezo move, a potential difference is applied across the

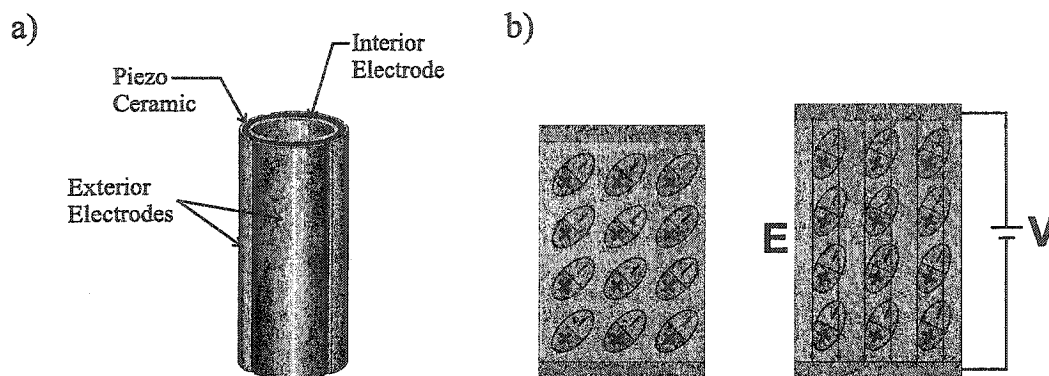


Figure 3.5: a) Schematic representation of a piezo tube used in the AFM scanner. b) Schematic representation of a piezoelectric material and the effect of applying a potential across it.

plates. The potential difference V , creates an electric field E , which in turn applies a force on the dipoles inside the piezo material. Depending on where and how the potential difference is applied, the net effect causes the piezo to contract, elongate, and/or bend. This is shown systematically in figure 3.5b.

Unfortunately, the piezo material is not an ideal, system because the strain is not directly proportional to the electric field. Figure 3.6 shows the displacement as a function of the applied voltage to the piezo material used in the AFM scanner. The change in length of the piezo was measured using a linear voltage displacement transducer (LVDT) connected to the same Keithley source-measure unit used to cycle our cells. The light colored circles in the data show the first elongation of the piezo. Starting from the rest position (0.0 V), the piezo is initially forced to elongate as the applied potential is increased from 0 to 200 V. Decreasing the potential causes the piezo to contract from approximately $4 \mu\text{m}$ to $-4 \mu\text{m}$ as shown by the solid line. The data also show that returning the piezo to the zero position requires an

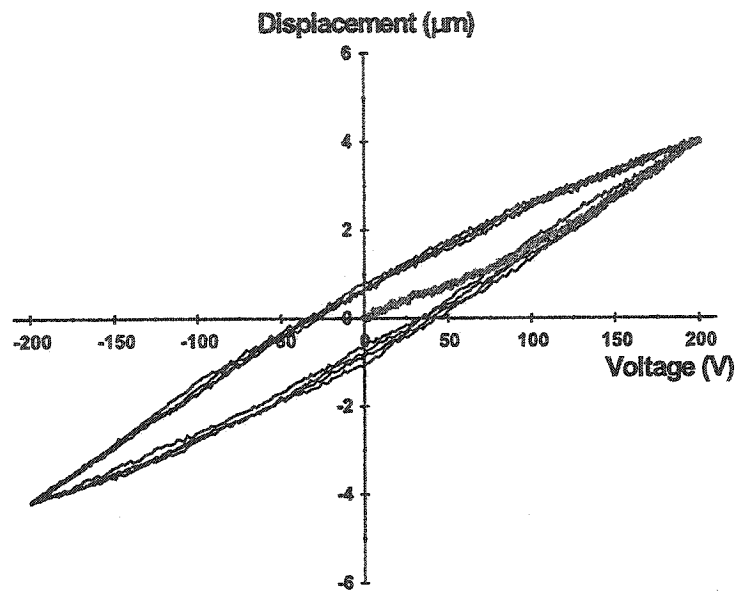


Figure 3.6: Displacement versus voltage plot showing the hysteresis of a piezo material in an AFM scanner.

additional voltage. The data in figure 3.6 show four full hysteresis loops displaying good reproducibility. This hysteresis is responsible for creating “shadows” on AFM topographs.

A piezo material also suffers from *creep*. When a rapid change in voltage is applied to a piezo its response can be separated into two parts: a *rapid* and a *slow* response [86, 84]. The rapid response of the piezo happens almost instantaneously, whereas the slow response will occur from 0.1 to 10 seconds or in the worse case up to 100 seconds later.

Because of the shape of the piezo tube and the bending it undergoes during the scanning process, the AFM cantilever travels along the inside surface of an elliptical paraboloid. Since the cantilever is not directly centered on the axis of the tube, the

elliptical paraboloid has two different radii of curvature along the two perpendicular axes (for example the x and the y axis in the cartesian coordinate system). This geometry causes AFM images to be curved instead of flat. This curvature is known as *cross coupling* [84] and can cause problems in converting raw AFM data to flattened topographs².

Figure 3.7 shows an example of the image artifacts due to tip shape, hysteresis, creep, and cross coupling discussed above. Figure 3.7a shows a typical AFM topograph of a commercial step grating. The image shown here has only been tilted. Figure 3.7b shows a cross section of the grating. As can be seen, the side walls B and D are not perfectly vertical due to the pyramidal shape of the tip under the cantilever. Also, due to hysteresis effects, the slope of each side B and D are not at the same angle. Hysteresis is also responsible for the difference in heights of points A and E as shown by the solid line. These effects are all due to the fact that the voltage required to contract the piezo is not the same as the voltage required to elongate it, as shown in figure 3.6. Close attention to figure 3.7b shows an *edge* at point C and a *dip* at point E. This effect is due to creep. As the piezo arrives at point A the feedback loop sends a voltage to the piezo causing it to contract to what it believes is the right height. However, creep in the piezo causes it to raise higher than the step giving the impression of an edge at point C. In order to maintain contact between the tip and the surface, the feedback loop must then send a voltage of opposite polarity to slightly elongate the piezo. The effect at point E is exactly the same but in the opposite direction. Finally, the cross section shows the cross coupling effect due to the shape of the piezo tube and the relative position of the cantilever. By the naked eye, the cross section data appears to be flat but it is only when we fit the data to

²A discussion on image flattening is given later in this chapter.

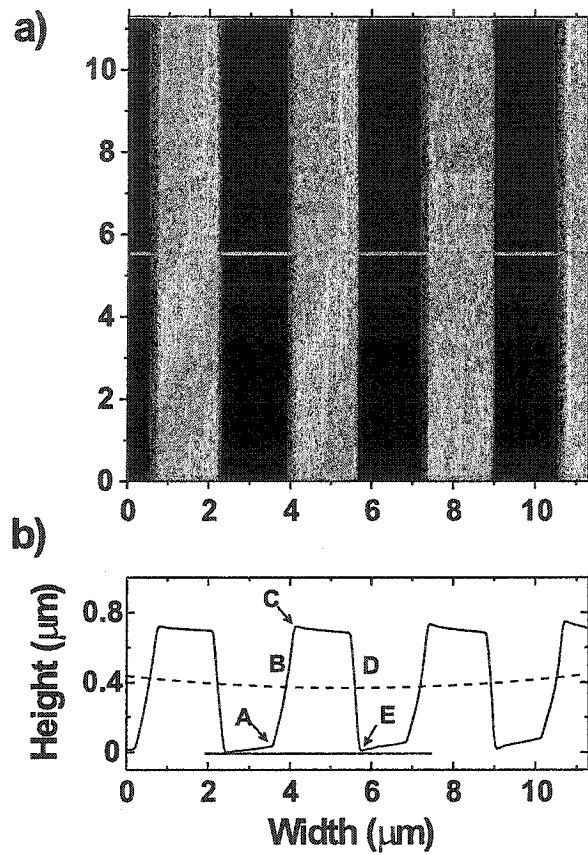


Figure 3.7: Combined effects of tip shape, hysteresis, creep, and cross coupling in an AFM image. a) AFM topograph of a step grating. b) Cross section of the AFM topograph along the line in a).

an equation of the form:

$$f(x) = \alpha_1(x - x_o)^2 + \alpha_2(x - x_o) + \alpha_3 \quad (3.1)$$

which describes a parabola (see dashed line in figure 3.7b), that the curvature can be observed.

3.2 Experimental Setup

Since lithium is air sensitive, our experiments had to be conducted in an inert atmosphere. For this reason, the AFM was placed inside an argon-filled glovebox and mounted on a specially designed and carefully built vibration damping system [87]. Figure 3.8 shows the AFM inside the glovebox prior to its closing. The AFM sits

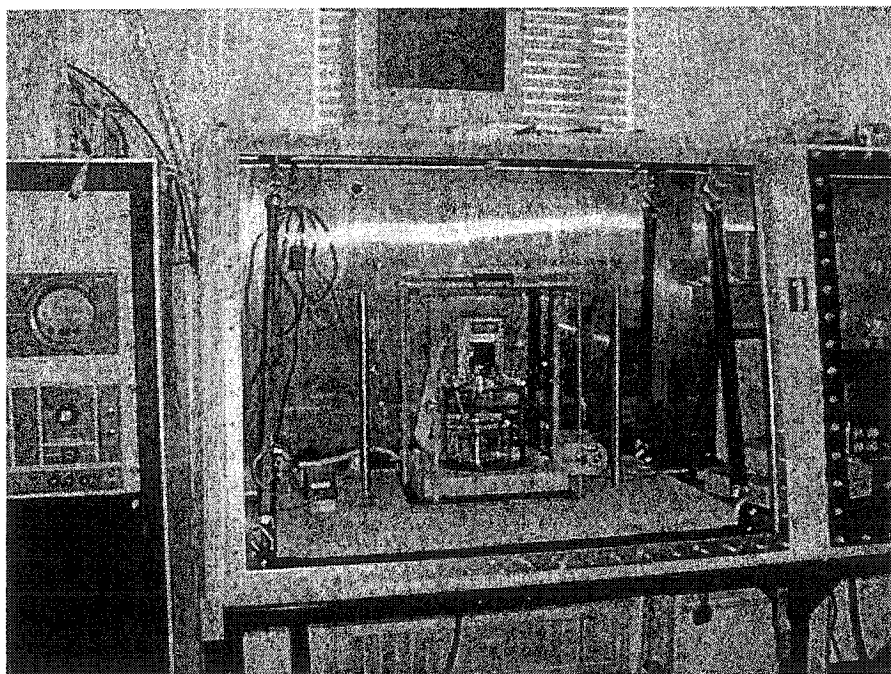


Figure 3.8: Picture of the AFM inside the glovebox.

on two granite slabs (a large one and a small one) suspended from the ceiling of the glovebox by a combination of springs and bungee cords. The AFM sits on the smaller granite block which in turn sits on the larger granite block separated by vibration dampers (Arbor Scientific). Because the AFM is sensitive to air currents, a draft shield was designed and constructed to allow for the continual circulation of argon

gas inside the glovebox by the purification system.

To reduce thermal drift, a single heating element (approximately $20 \times 20 \times 0.8$ cm in size) was placed directly in contact with the bottom of the small granite slab. The heat from the heating element was used to heat the small granite slab which in turn heats the microscope and sample by conduction and radiation. Due to the large thermal mass of the granite, the temperature inside the draft shield was maintained at a constant temperature of $(30 \pm 0.1^\circ\text{C})$.

To perform the *in situ* measurements a wetcell was designed and constructed in order to house the electrode under study as it reacts with lithium. Figure 3.9 shows

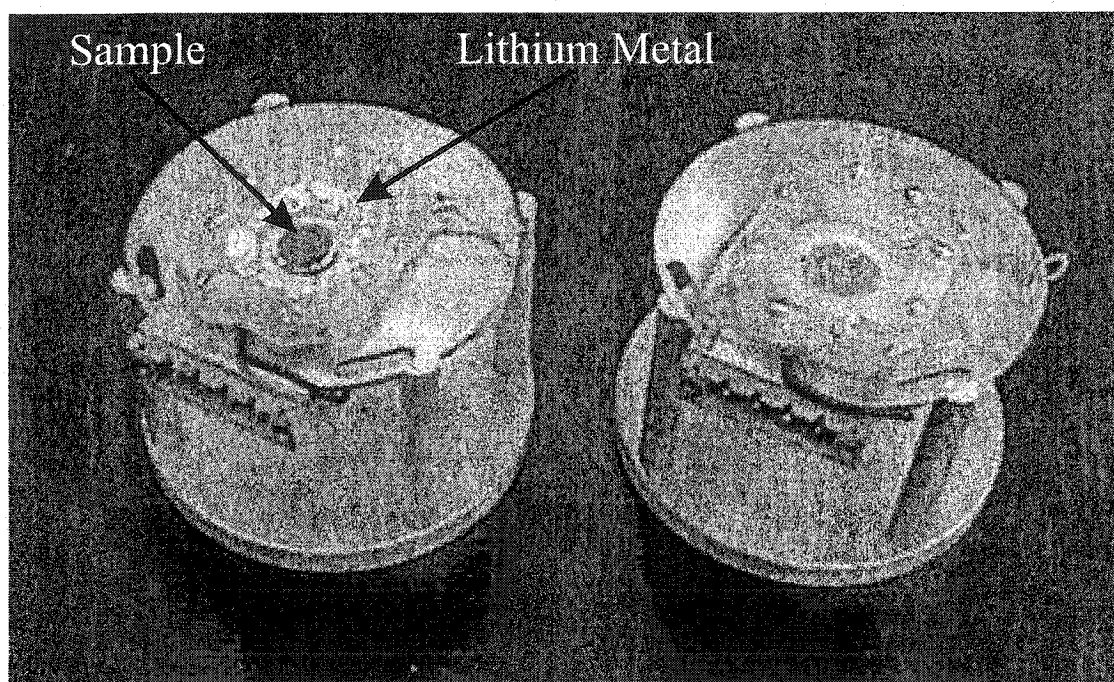


Figure 3.9: Wetcells used to house the sample during imaging. The wetcell on the left shows the position of the sample and the position of the lithium foil which acts as the counter electrode. The sample sits on a copper current collector which is visible in the wetcell on the right.

a picture of the wetcell used in our experiments. The wetcell on the left shows the position of the sample and the position of the lithium foil (FMC 99.5%) which acts as the counter electrode. The sample sits on a copper current collector which is visible in the wetcell on the right. The well is then filled with electrolyte (1M LiPF₆ in (1:1) EC/PC, EM Science) To measure the electrochemical data, a Keithley 236 system is used.

3.3 Imaging Analysis

AFM images by themselves only show a “picture” of the morphology of the sample under study. In order to extract any quantitative information it is necessary to engage in image analysis. In the experiments conducted in this work, continuous imaging occurred for many hours during which time hundreds of images were collected. Therefore, in order to analyze all these images, special image analyzing software was developed. The first step in any analysis of AFM topographs is *image flattening*.

3.3.1 Image Flattening

Programs to perform image flattening can be found in large abundance on the internet as freeware. However most of these work in a very specific manner and only analyze one image at a time. For our work, it was necessary to develop our own image flattening software.

Since it is impossible to mount our samples perfectly leveled, the AFM topographs collected are both inclined in space and curved with two distinct and perpendicular

radii of curvature. Therefore, the first step of our program was to fit (see Appendix D for an example of the fitting method used in this work) our AFM topographs to a plane of the form

$$z = a - bx - cy. \quad (3.2)$$

Figure 3.10 shows a two-dimensional schematic representation of geometry relating the position and motion of the AFM cantilever, the surface data (solid line) and the best fit plane (dashed line). Since the motion of the AFM cantilever is perpendicular

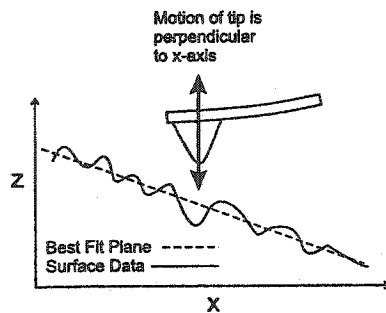


Figure 3.10: Two dimensional schematic representation of the geometry relating the position and motion of the AFM cantilever, the surface data (solid line) and a best fit plane (dashed line)

to the x and y axes of the fitted plane, the AFM topographs were tilted by taking the difference between the data and the plane as described by:

$$Image^{leveled}(x, y) = Image^{raw}(x, y) - Plane(x, y). \quad (3.3)$$

Once the image was leveled it was then necessary to remove the curvature. To do this, the leveled data was fitted to an elliptical paraboloid of the form:

$$z(x, y) = \alpha(x - x_o)^2 + \beta(y - y_o)^2 + \gamma. \quad (3.4)$$

However, because of the geometry of the system, the data could not simply be subtracted from the elliptical paraboloid. Figure 3.11a shows schematically that the

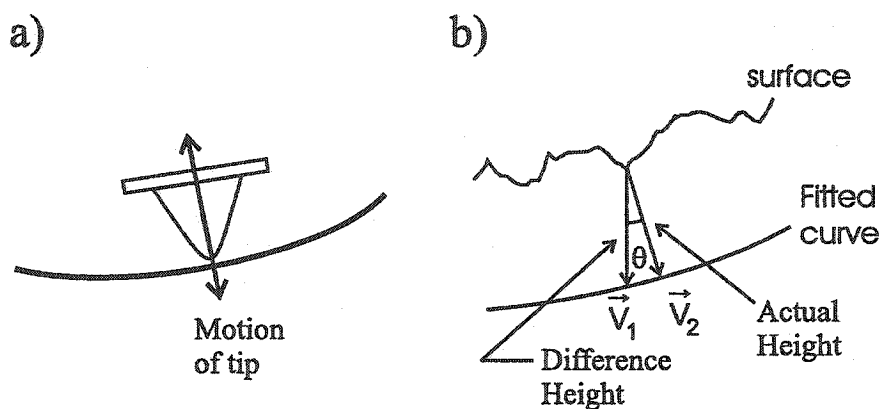


Figure 3.11: a) Motion of the AFM tip is perpendicular to the curvature of the image. b) The real image heights are equal to the difference in height between the sample and the fit times $\cos(\theta)$.

motion of the cantilever is perpendicular to the fitted paraboloid. Because of this it was necessary to find the closest distance between each point on the surface data and the fitted curve. In our case, this was approximated by taking the difference between the data and the fitted curve and multiplying by $\cos(\theta)$ as shown in figure 3.11b³. The $\cos(\theta)$ term is calculated by taking the scalar product of vectors \vec{V}_1 and \vec{V}_2 shown in figure 3.11b.

Figure 3.12 shows a comparison between an AFM topograph of a silicon grating

³Typical values of $\cos(\theta)$ are 0.99998 with a standard deviation of 0.00002.

(3 μm pitch) flattened with our flattening routine (3.12 a and c) and the commercial software used to control the AFM (3.12 b and d). Besides the different contrast scale, the AFM topograph flattened by our routine (3.12a) is the same as the topograph from the commercial software (3.12b). Figures 3.12 c and d show cross-sections of the AFM topograph taken at the same point in both images (black line on the topographs). Besides a small difference in heights, the two cross-sections are virtually identical.

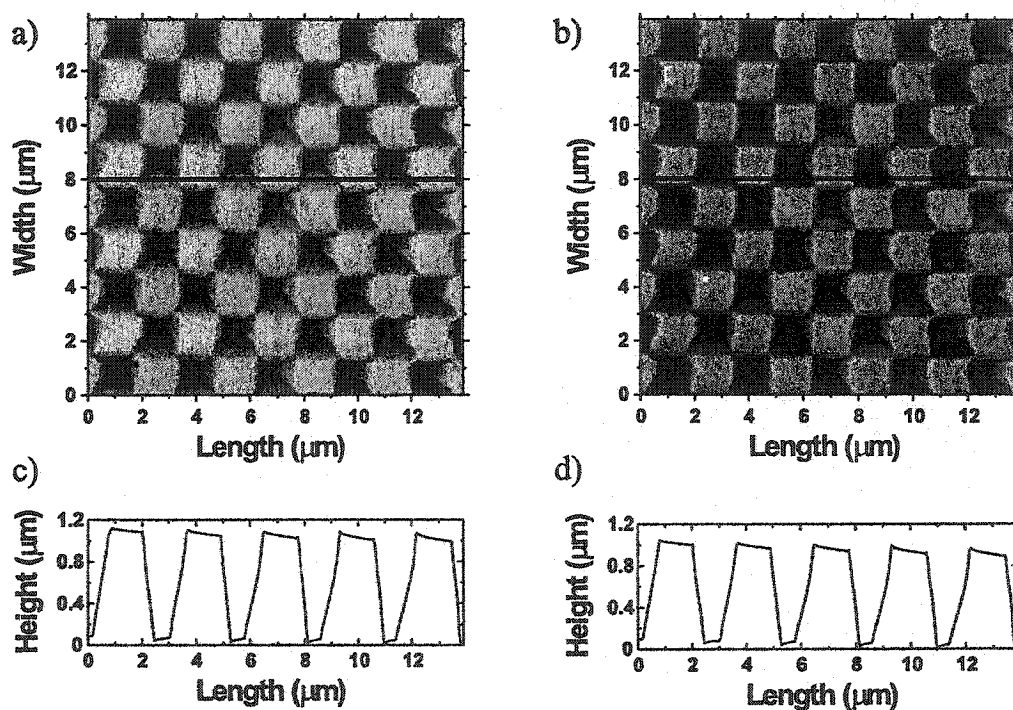


Figure 3.12: Comparison between images flattened by a) commercial and b) our software. Each image is $13.9 \times 13.9 \mu\text{m}$ in size.

Chapter 4

In Situ AFM characterization of Electrode Materials

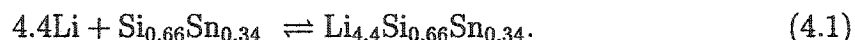
Until now, this thesis has been concentrated mostly on the electrochemical behavior of $\text{Si}_{0.66}\text{Sn}_{0.34}$ films. From this, a reaction mechanism was proposed where Li enters the $\text{Si}_{0.66}\text{Sn}_{0.34}$ compound and causes hitherto undefined volume changes. This chapter will discuss the volume changes undergone by $\text{Si}_{0.66}\text{Sn}_{0.34}$ and other electrode materials.

4.1 Morphology of $\text{Si}_{0.66}\text{Sn}_{0.34}$ Thin Film Electrodes

Some of the largest and best-known expansions in solids are those that occur when hydrogen is absorbed within metal hydrides [88, 89]. The reversible expansion is characterized by the so-called “hydrogen-induced volume change” which has been shown to be about $2.8 \pm 0.2 \text{ \AA}^3$ per incorporated hydrogen atom in most d-band metal hydrides [89]. Typical metal-hydride systems like H_xPd and H_xTi can react

to a level of $x = 1$ and $x = 2$ respectively, leading to overall volume expansions of about 20 and 32%, respectively [89]. Such expansions, which have been observed by various microscopy techniques, lead to particle fracture that can have important consequences for hydrogen storage alloys in fuel cell applications and for nickel/metal hydride battery electrodes [90].

The reaction of lithium atoms with a $\text{Si}_{0.66}\text{Sn}_{0.34}$ film can be described by the equation below:



As will be shown, this reaction is accompanied by a large volume increase in the metal film as discussed in chapter 1. Figures 4.1a and b show a schematic representation of a $\text{Si}_{0.66}\text{Sn}_{0.34}$ film before and after its first lithiation, respectively. As lithium reacts with a $\text{Si}_{0.66}\text{Sn}_{0.34}$ film, small clusters¹ within the film attempt to expand uniformly in all directions, as shown in figure 4.1e. However, since the metal is restricted in the plane of the substrate by the adhesion between the film and the sample and also by the rest of the film, the net force is found in the direction perpendicular to the substrate (4.1f). Therefore, the resulting volume expansion of the film is found largely (if not entirely) along the axis perpendicular to the plane of the film. For convenience, we will describe the plane of the sample as the x-y plane and the axis perpendicular to the sample as the z-axis. Removing Li for the first time from the fully discharged electrode causes the film to contract uniformly in all directions (4.1g). This causes the film to crack as shown in figure 4.1c. In some cases, poor adhesion between the metallic film and the substrate causes the film to curl during the removal of Li. This is shown schematically in figure 4.1d.

¹By cluster we simply mean any arbitrary small volume of material

The first *in situ* morphology studies on $\text{Si}_{0.66}\text{Sn}_{0.34}$ electrodes were performed using an optical microscope by Kevin Eberman at 3M USA. The cell used for *in situ* optical microscopy consisted of a glass chamber with a thin glass cover-plate. A $7.5\ \mu\text{m}$ $\text{Si}_{0.66}\text{Sn}_{0.34}$ film sputtered on $130\ \mu\text{m}$ thick copper foil was mounted as the working electrode in a two-electrode cell with lithium metal as the counter and reference electrode (the electrolyte was 1M LiPF_6 in 1:1 EC:DC). The holes used for leads and for injecting the electrolyte (1M LiPF_6 dissolved in equal volumes of ethylene carbonate and diethyl carbonate) were sealed with polypropylene hot melt glue. A Sony CCD Color Video Camera DXC-151AP mounted on the microscope was used to collect images of the sample magnified by either a $10\times$ or $20\times$ objective and a $0.55\times$ eyepiece. Digital images of the film surface were stored at 5 minute intervals during the discharge/charge cycles. A constant current was applied such that each cycle lasted 5 hours.

Figure 4.2 shows the results of an *in situ* optical microscopy experiment designed to determine the degree of in-plane strain induced during the addition of lithium to the film. The grid-lines are razor blade marks made prior to assembling the cell. Three interruptions were made during the first discharge to determine whether the metal film on the copper foil would expand in-plane over time. A careful analysis of the grid-lines from the sample in its initial state (Figure 4.2a) and in its discharged state (Figure 4.2b) showed that no measurable lateral expansion occurred despite the fact that x in $\text{Li}_x\text{Si}_{0.66}\text{Sn}_{0.34}$ reached 1.98, for which 145% volume expansion (based on the fact that x has a maximum of 4.4) is expected. We conclude that the metal expanded solely in the out-of-plane direction as it alloyed with lithium the first time.

After about one hour during the first charge (removing Li) the film shrinks and

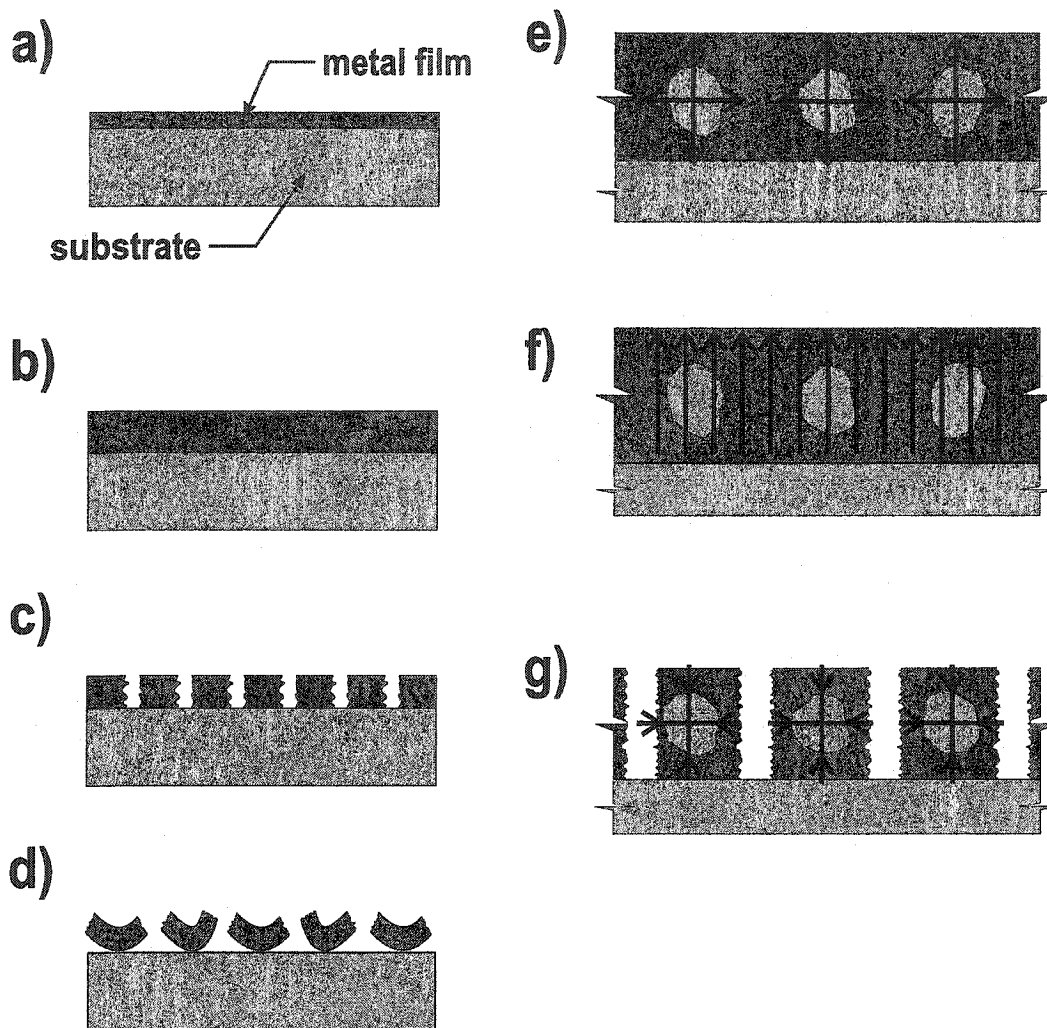


Figure 4.1: a) Geometry of a metal film (dark) on a substrate (light). b) The first reaction of Li with a film causes the film to expand along the axis perpendicular to the film-substrate boundary (z-axis). c) Removing Li for the first time from the fully discharged electrode causes the film to contract uniformly in all directions. This causes the film to crack. d) Poor adhesion between the metallic film and the substrate causes the film to curl upon the removal of Li from the electrode. e) Each cluster of $\text{Si}_{0.66}\text{Sn}_{0.34}$ (shown in light gray) wants to expand in all directions. f) The net force causes the film to expand in the direction perpendicular to the substrate. g) Removing the lithium causes the clusters to contract.

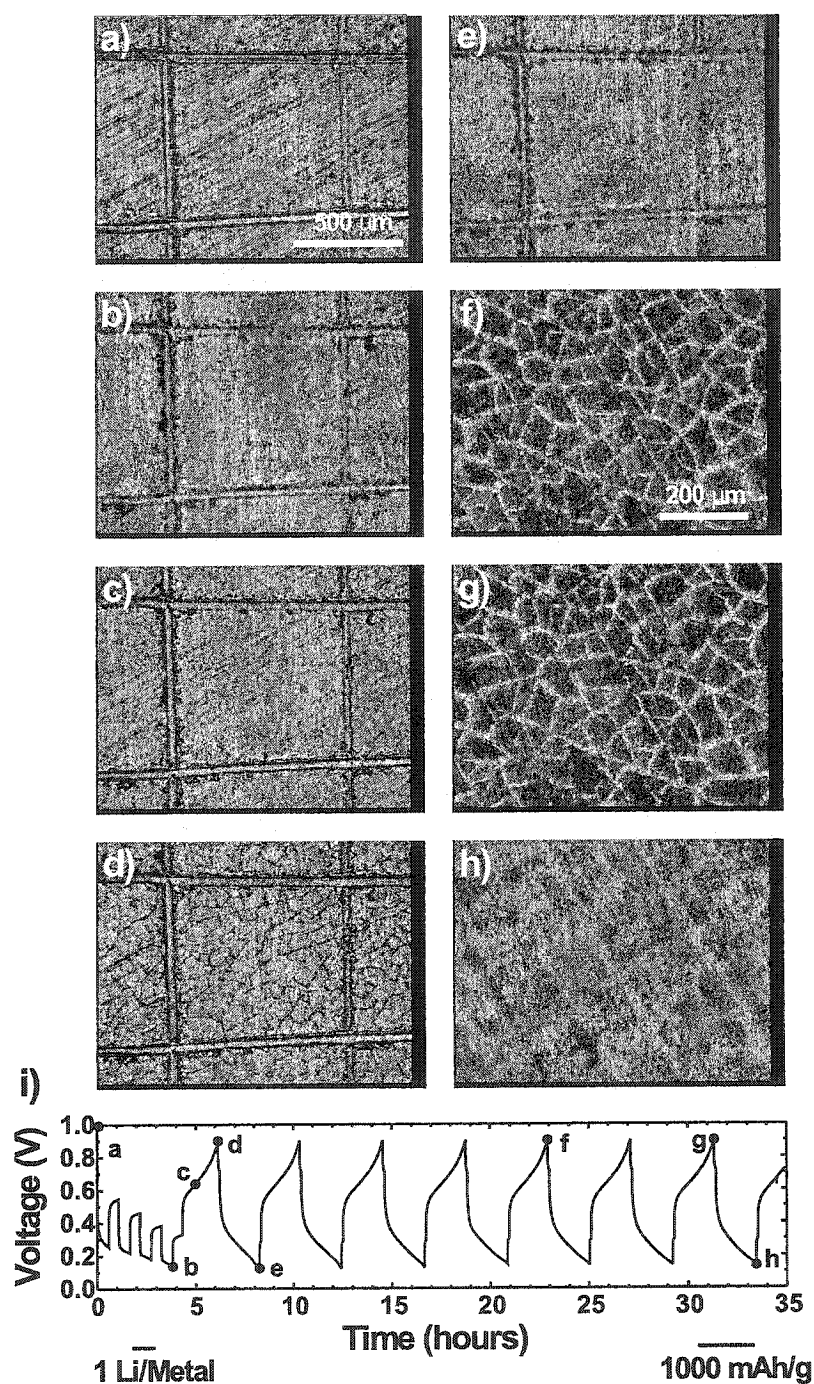


Figure 4.2: Selected optical micrographs corresponding to points labeled in the voltage curve below. A scale bar displays the length of time that corresponds to a charge transfer of 3.5 moles of lithium per mole of metal in the original film. Figures a through e are at the same lower magnification, and figures f through h are at higher magnification. j) Voltage versus time. The equivalent number of $\text{Li}/\text{Si}_{0.66}\text{Sn}_{0.34}$ and capacity in mAh/g are indicated by the scale bars at the bottom of the figure.

cracks (Figure 4.2c). At this magnification it is impossible to judge whether the cracks form all at once or not. Now the particles of metal film delimited by the crack edges shrink until almost all of the lithium has been removed (Figure 4.2d). This crack pattern is similar to the crack pattern observed by *ex situ* SEM studies performed by Brousse *et al.* on SnO₂ thin films [91]. However, in their case, the particles formed by the cracking were on the order of 100 nm while those shown here in figures 4.2 d, f, and g are on the order of 100 μm . Figure 4.2e shows that once the particles have alloyed with lithium again to the level of figure 4.2b, the cracks become too small to observe. The particle shape is almost perfectly preserved, causing the cracks in the film to seemingly disappear. Indistinguishable twin views at higher magnification (Figures 4.2 f and g) of the fully charged film show clearly that the particles maintain their shape. The last image shows that even on this fine scale the cracks seem to disappear. A “time-lapsed movie” of this experiment is available for viewing on the accompanying CD or on the web-site www.physics.dal.ca/~dahn/Luc-Thesis.html.

Using *in situ* optical microscopy, an analysis was performed on the average size of the particles formed by the cracks during the first charge cycle. Figure 4.3a shows the average particle size of a 5.9 (\bullet), 3.7 (\blacklozenge), and 3.5 (\blacksquare) μm thick film as a function of the first discharge capacity. The average particle size was calculated by taking the square-root of the number of particles per unit area obtained from the optical images. As can be seen, reducing the initial depth of discharge (less Li inserted) decreases the average size of the particles formed during the first charge cycle. Assuming the maximum capacity (2600 mAh/g) is accompanied by a 300 % volume expansion, we can derive the average particle size as a function of the thickness of the lithiated film. Figure 4.3b shows that plotting the average particle size as a function of the final

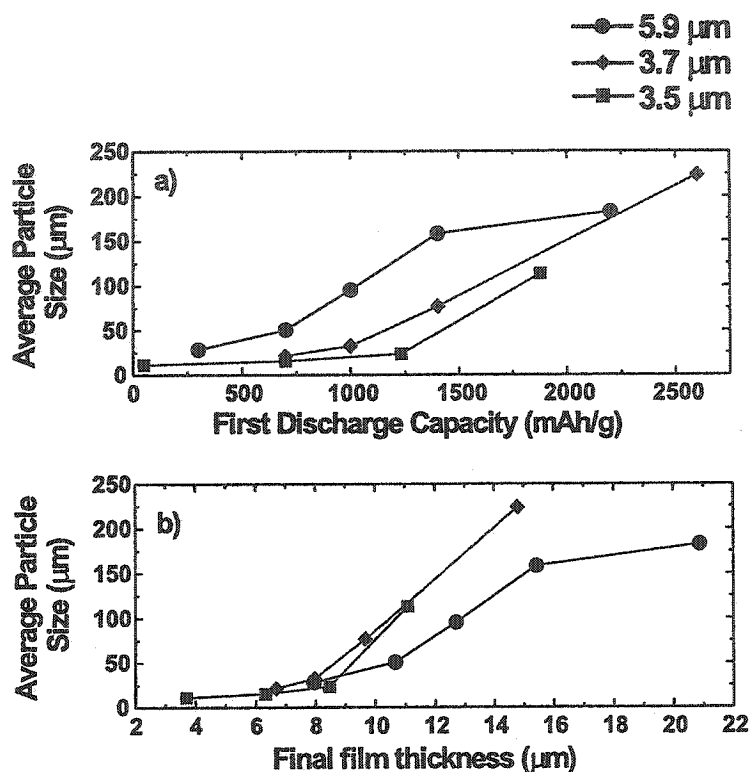


Figure 4.3: Average particle size of a 5.9 (●), 3.7 (◆), and 3.5 (■) μm $\text{Si}_{0.66}\text{Sn}_{0.34}$ film as a function of a) the first discharge capacity and b) the final film thickness.

film thickness gives a more consistent result. We can qualitatively understand these results by considering the stresses involved during the insertion and removal of Li. As shown schematically in figure 4.4, there are two stresses involved in the contraction of the film. The stress σ_1 is responsible for cracking the film (at the fracture point) while σ_2 , at the film/substrate interface, inhibits the lateral contraction of the film. If the forces at the film/substrate interface were greater than forces that cause the film to contract, the film would not crack but simply contract vertically when lithium is removed. However, in our case, since the film cracks, the interfacial forces must be

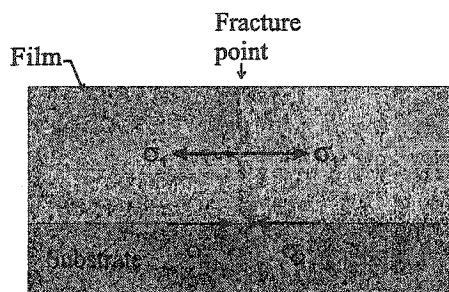


Figure 4.4: Schematic representation of the stress (σ_1 and σ_2) involved during the delithiation of a $\text{Si}_{0.66}\text{Sn}_{0.34}$ film.

less than the forces that cause the film to contract. Since σ_2 is constant, the results in figure 4.3 can be explained by monitoring the forces involved in σ_1 .

Two films of different thickness, both lithiated to same amount, will crack at the same value of σ_1 . However, in the thicker film, the forces that cause the contraction will be larger (since the cross-sectional area is larger) and therefore cause the film to shear away from the substrate more easily. This, in turn, causes bigger particles to form. The same results are obtained when two films of the same initial thickness are lithiated to different amounts. The more lithiated film, which has undergone a larger expansion, will exert a larger force (again due to the larger cross-sectional area) during the extraction of lithium. And, as for the case above, the larger force will cause the film to shear away from the substrate more easily and form bigger particles.

It appeared from this optical microscopy experiment that fracture occurs once during the first charge, after which the particles shrink and expand reversibly without further cracking. In order to determine whether the fracture does occur on a scale finer than that perceptible with optical microscopy, AFM experiments were performed.

Figure 4.5 shows the results of a typical AFM experiment. The open circuit voltage of the freshly assembled cell was 2.0 V. In order to reduce the average size of the particles formed by the cracks during the first discharge, the cell was discharged

to 0.5 V, and then the experiment began. Figure 4.5a shows the AFM image collected after this initial discharge to 0.5 V. The vertical distance corresponding to maximum contrast (white to black) and the lateral scan range are given in table 4.1. Figure 4.5b shows an image of the same region of the film after all available lithium has been removed from the film. A crack can be seen in the lower right corner of the image. Figure 4.5c shows the same region of the film after lithium had been added again to the same level as in figure 4.5a, demonstrating that the crack closed as the segments of the film expanded to their previous size. The scan range was then increased to 37

Table 4.1: Description of the images displayed in figure 4.5.

Images in figure 4.5	Value of x in $\text{Li}_x\text{Si}_{0.66}\text{Sn}_{0.34}$	Lateral Image Size (μm)	Maximum contrast from black to white (nm) ^a
a	0.3	19	150
b	0	19	138
c	0.3	19	140
d	0	37	185
e	0.3	37	150
f	1.0	37	185
g	0.5	37	270
h	0	37	440
i	1.0	37	175
j	0.06	37	1040
k	2.5	37	290
l	0.4	37	1900

a-Images were flattened to remove tilt.

μm to view more of the crack pattern, and selected to include the region previously scanned (indicated by the white square in figure 4.5d). Figure 4.5d shows the AFM image (lithium removed) after 5 discharge/charge cycles between 1.3 and 0.5 V with two cracks present. The cracks closed as lithium was inserted to 0.5 V (figure 4.5c),

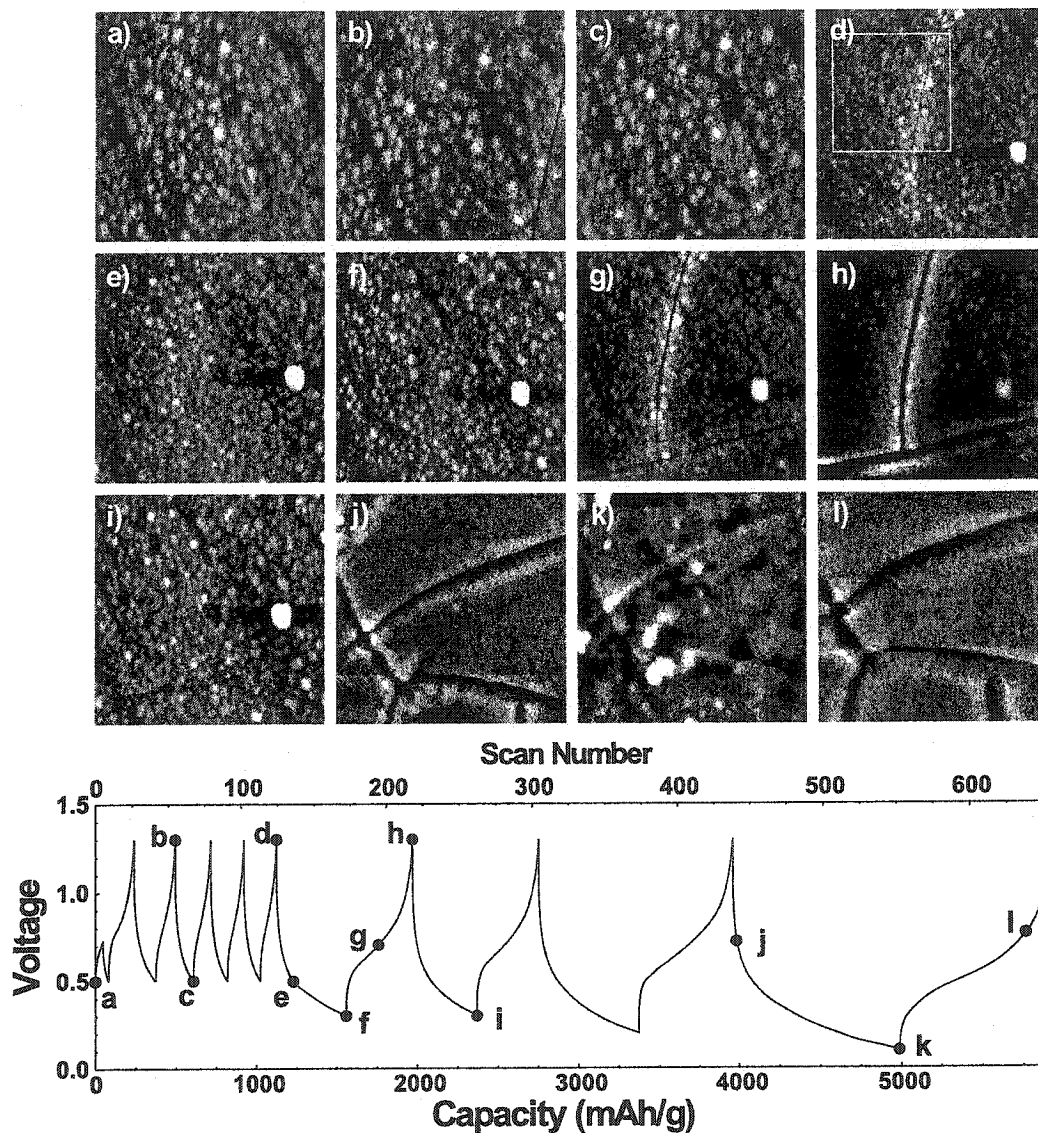


Figure 4.5: Selected AFM images with scan ranges and contrasts given in table 2. The images 4.5a-l were collected at the corresponding points indicated in the voltage-time curve. A scale bar displays the length of time that corresponds to a charge transfer of 1000 mAh/g and another scale bar displays the time that corresponds to the reaction of one mole Li per mole $\text{Si}_{0.66}\text{Sn}_{0.34}$.

as shown in figure 4.5e. Up to this point only about 0.3 Li per $\text{Si}_{0.66}\text{Sn}_{0.34}$ had been added and removed and the volume changes were completely reversible. Then, further lithium (about 1 more Li per $\text{Si}_{0.66}\text{Sn}_{0.34}$) was added to 0.3 V (figure 4.5f). No cracking or peeling occurred, suggesting that all volume expansion takes place in the vertical direction. When lithium was subsequently removed, as shown in figures 4.5g and 4.5h, the original cracks (see 4.5d) opened to a much wider extent, but no further cracking was observed from these images. In addition, the particles curled substantially near their edges where they had detached from the substrate. Notice the vertical distance corresponding to maximum contrast changed dramatically as the edges curled (see table 2). Finally, figure 4.5i shows that the cracks closed and the film flattened again when lithium was added once again to 0.3 V. Figure 4.6 shows three-dimensional views of the film corresponding to figures 4.5h and 4.5i.

The cell was cycled a few more times and a different region of the film was selected for imaging. Figure 4.5j shows the image when almost all the Li was removed. Lithium was then added to a level of 2.5 Li per metal at 0.1 V (figure 4.5k). The cracks closed and the curling of the edges was eliminated. Note that the cracks first closed at 0.3 V (not shown), so between 0.3 V and 0.1 V, all of the expansion of the film must have been in the vertical direction. Lastly, (figure 4.5l) almost all the Li was removed and larger cracks between more curled particles— but in the same places as those initiated before — were observed. Most of the scan sequence (about 400 images) described here is available for viewing as a “time-lapsed movie” on the accompanying CD or on the web-site www.physics.dal.ca/~dahn/Luc-Thesis.html.

The sequence of events shown in figures 4.2 and 4.5 can be qualitatively understood by considering the desiccation of mud. As an example, Figure 4.7 compares an optical

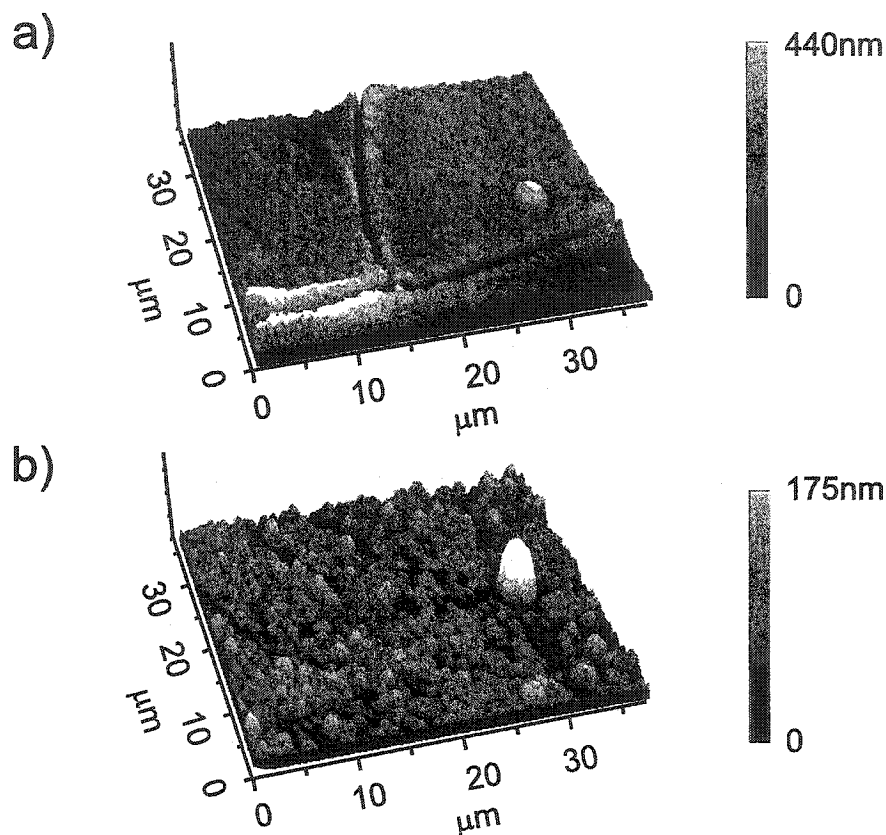


Figure 4.6: Three dimensional views of a) image 4.5h, and image 4.5i. The out-of-plane distance is shown using the contrast scale given to the right of each image.

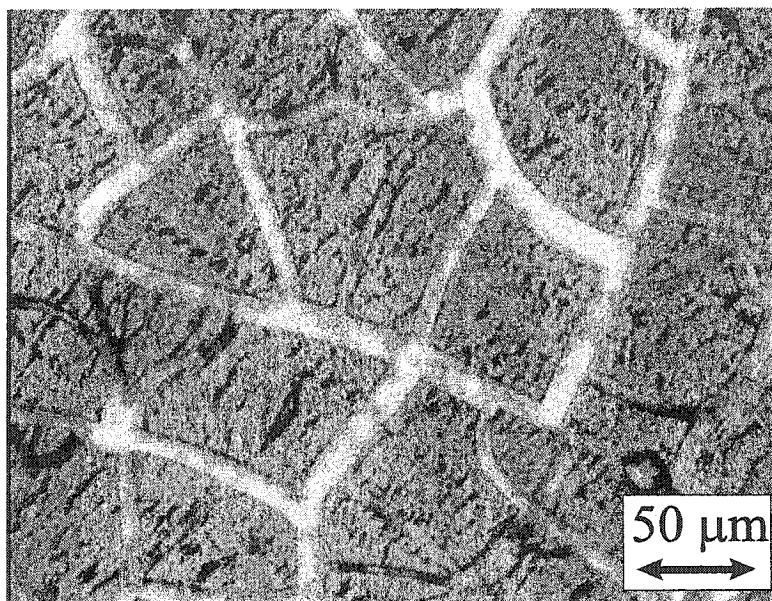
image of a film after a discharge/charge cycle with a photograph of dried mud. The similarities are clear. There have been a number of experimental and theoretical investigations of mud drying [92, 93] that are useful to our experiments. Groisman and Kaplan [92] show that when the volume of a mud layer in a glass dish is reduced by drying, cracks that extend to the base of the dish form at approximately the same time, separating the mud film into separate “cells”. Further volume reduction is accomplished by the shrinking of these cells without further cracking. Kitsunezaki

[93] shows that during this shrinking, the edges of the cells slide with respect to the stationary dish, while a "patch" at the center of the cell remains fixed with respect to the dish. This is clearly shown in figure 7c of ref. [93].

The same sequence of events that occurs during the drying of mud also occurs here as lithium is removed from the alloy film. First, a series of cracks form, creating separate flake-like particles. The edges of the particles move with respect to the substrate as shrinking occurs and the particle centers appear to remain firmly attached. It is fortunate that the particle centers do remain attached, for the electrical connection to the substrate is necessary for the transfer of the needed electrons to complete the electrochemical reaction. Once the particles are formed, they are able to expand and contract reversibly over a remarkable range as Li is added and removed. If enough Li is added to cause the particles to touch, and then if further Li is added, the particles must expand in thickness, or buckle away from the substrate. We have seen evidence for both events in our studies, but have not shown examples of particles buckling away here.

It is difficult to obtain a sense of the changes in film thickness from the images presented in figure 4.5. In fact, images 4.5e and 4.5f look almost identical to the eye. It is only when one performs a statistical analysis that one learns image 4.5e (RMS roughness = 33.5 nm) is much rougher than 4.5f (RMS roughness = 26.9 nm). This suggests that the film has expanded vertically in a perfectly proportional manner. The top two panels (a and b) of figure 4.8 schematically show that if the thickness of a thin film on a smooth substrate increases everywhere, so does the roughness. To study the changes in roughness of the film, it is very important that the area analyzed remain well adhered to the substrate. It is also important that the area chosen be

a)



b)



Figure 4.7: The resemblance of an optical micrograph of a) a Li-alloy film after expansion and contraction to b) cracked mud in a dry lake bed.

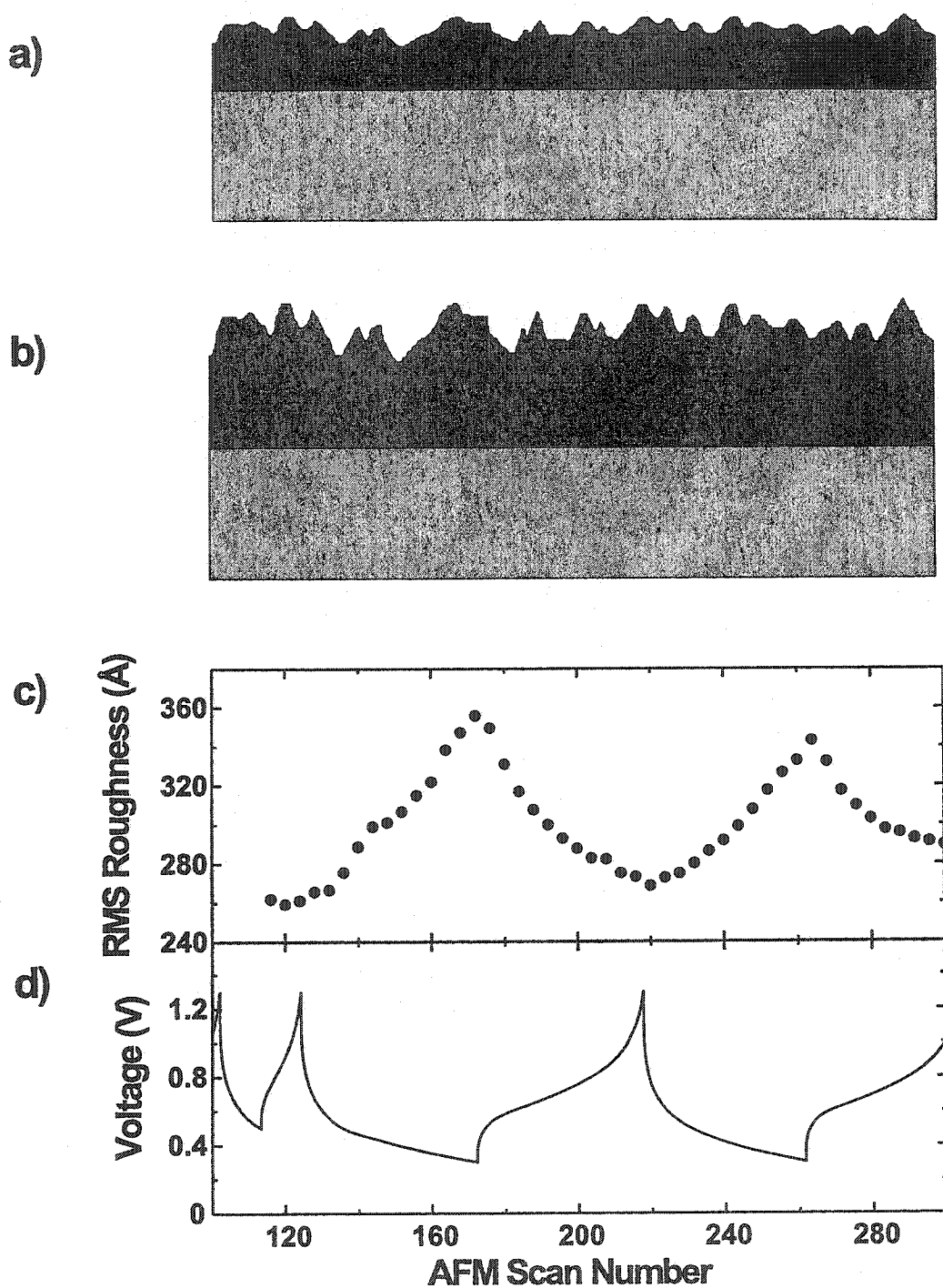


Figure 4.8: (a) Schematic representation of a rough film on a smooth substrate. (b) Schematic representation of the film in (a) which has doubled in thickness. (c) Change in RMS roughness of the electrode surface compared to (d) the voltage versus AFM scan number.

the same for all measurements. Therefore, the region shown by the white square in figure 4.5e was chosen for the statistical analysis. From the images collected for the experiment shown above, the RMS roughness (standard deviation) was calculated as a function of lithium content. As is customary, the RMS roughness R_{RMS} was defined as:

$$R_{RMS} = \sqrt{\frac{\sum_{i=1}^N (z_i - z_\mu)^2}{N - 1}} \quad (4.2)$$

where N is the total number of data points, z_i is the vertical coordinate of the image and z_μ is the mean value of the z_i 's. The bottom panels in figure 4.8 show the RMS roughness (4.8c) of the highlighted area in figure 4.5g compared to the voltage curve collected during the experiment (4.8d). The RMS roughness is a function of the lithium content in the electrode. As lithium is added to the electrode (scan numbers 124 to 172 and 217 to 262) the roughness increases. Similarly, as the lithium is removed from the electrode (scan numbers 172 to 217 and 262 to 304) the roughness decreases.

Equation 4.2 shows that if all points of the film double (for example) in height, then so does the RMS roughness. Hence, from the fractional change in roughness, one could then deduce the total growth of the film. This analysis, however, assumes that the underlying substrate is perfectly smooth. In the next section we will show how to obtain the change in height of an electrode material from the RMS roughness measurements.

4.2 Measuring Volume Changes

4.2.1 Volume Changes from RMS Roughness

An *in situ* AFM study of thickness changes in nickel hydroxide electrodes has been reported in [94, 95]. In both these previous studies, the change in thickness of the electrode was studied by single point scanning. This method consists of maintaining the AFM tip of the nanoprobe at a constant point on the electrode while monitoring the elongation and contraction of the piezo necessary to maintain a constant force of the cantilever on the sample. Also, in both these cases, the height changes were observed over a span of only a few minutes. Although this method can be used to obtain changes in thickness, it has two disadvantages. In the first case, single point scanning does not allow for the morphology of the surface to be studied while the thickness changes are occurring. This potentially represents a huge loss of information on the topological properties of the sample. Secondly, due to the high temperature sensitivity of most SPMs, it is very difficult to measure the thickness changes of a sample for long periods of time. A change of 1° can easily induce sample drift which can cause uncertainties in the measurements described above. In this section, we introduce a new method for monitoring thickness changes *in situ* by AFM, while obtaining, at the same time, information regarding the surface topography.

As discussed in the previous section, the fractional change in RMS roughness is related to the total growth of a film. This analysis, however, assumes that the underlying substrate is perfectly smooth. The average roughness of a thin film sample is a convolution of the roughness of the substrate and of the film. To illustrate this point, consider a hypothetical film with surface height $z(x, y)$ of average thickness t

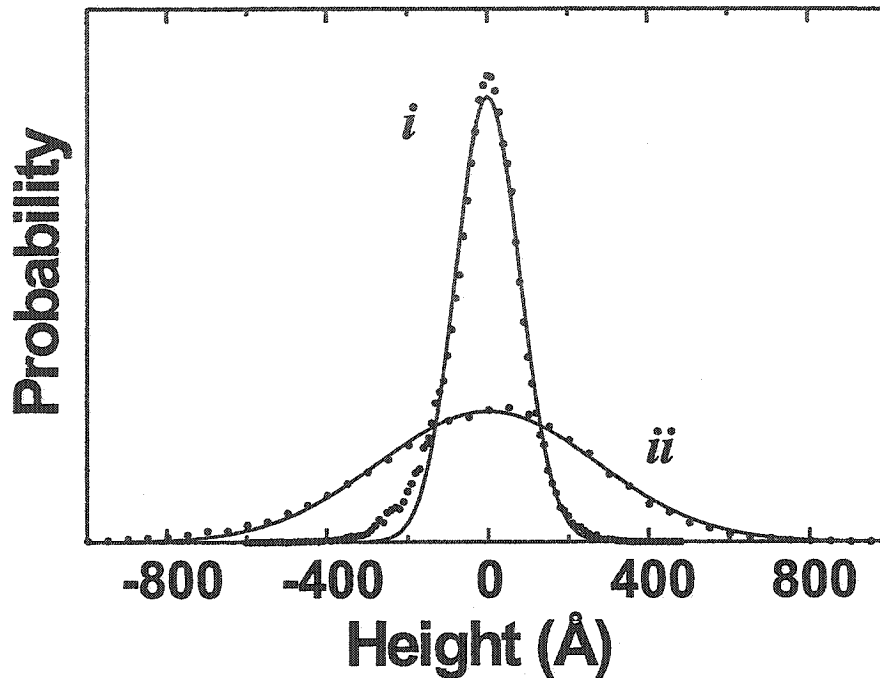


Figure 4.9: i) Height distribution of stainless steel substrate and ii) height distribution of the Si-Sn film.

with an inherent roughness $\Delta z(x, y)$, deposited on an initially rough substrate with height $s(x, y)$. With these definitions we obtain:

$$z(x, y) = s(x, y) + t + \Delta z(x, y). \quad (4.3)$$

Assume that a Gaussian distribution $P(s)$ can describe the surface roughness of the substrate. In the same way, a Gaussian distribution $P(\Delta z)$ can be used to describe the inherent roughness of the film. Figure 4.9 shows the height distributions of both the substrate (4.9i) and the sample (4.9ii). The circles represent the data and the straight lines represent the Gaussian fits. As can be seen, excellent agreement is

obtained. These distributions are written as follows:

$$P(s) = Ae^{-s^2/2\sigma_s^2} \quad (4.4)$$

$$P(\Delta z) = Be^{-\Delta z^2/2\sigma_{\Delta z}^2} \quad (4.5)$$

where A and B are normalization factors, and σ_s and $\sigma_{\Delta z}$ are the standard deviations of the substrate height and the film thickness, respectively. To obtain the standard deviation of the film surface, we take the convolution of the substrate height and the film thickness as follows:

$$\begin{aligned} P(z) &= AB \int e^{-s^2/2\sigma_s^2} e^{-((z-t)-s)^2/2\sigma_{\Delta z}^2} ds \\ &= Ne^{-(z-t)^2/2(\sigma_s^2+\sigma_{\Delta z}^2)} \end{aligned} \quad (4.6)$$

From equation 4.6 we obtain the RMS roughness of the film height: $\sigma_z = \sqrt{\sigma_s^2 + \sigma_{\Delta z}^2}$. This equation shows how the roughness of the substrate influences the roughness measurements of the film surface. Doing the same analysis for a film which expands α times its initial height ($t \rightarrow \alpha t$ and $\Delta z(x, y) \rightarrow \alpha \Delta z(x, y)$) we get an RMS roughness, σ_{lf} (*lf* - lithiated film), equal to $\sigma_{lf} = \sqrt{\sigma_s^2 + (\alpha\sigma_{\Delta z})^2}$. Taking the ratio σ_{lf}/σ_z we get a function of the form $\sqrt{(q^2 + \alpha^2)/(q^2 + 1)}$ where $q = \sigma_s/\sigma_{\Delta z}$. This function, plotted in figure 4.10 for $\alpha = 2$, shows the effects of the rough substrate. Since $\sigma_{\Delta z}$ is fixed, increasing the roughness of the substrate quickly prevents direct determination of the change in film height from the change in surface roughness.

Figure 4.11c shows the voltage versus both time (bottom abscissa) and AFM scan number (top abscissa) collected during the first complete discharge (insertion of lithium into the electrode) of this cell. During the discharge, the AFM topographic

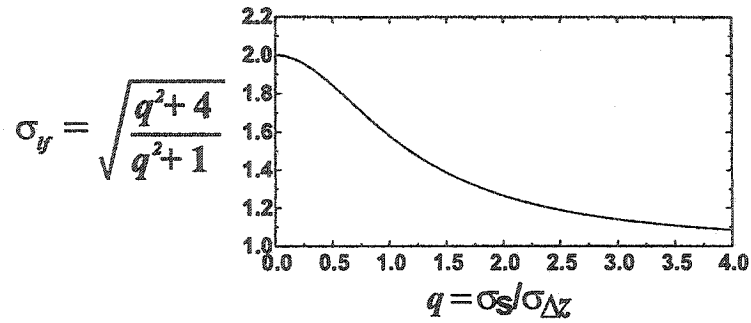


Figure 4.10: a) RMS roughness of a lithiated film $\sigma_{lf} = \sqrt{(q^2 + 4)/(q^2 + 1)}$ plotted as a function of $q = \sigma_s / \sigma_{\Delta z}$ showing the effect of substrate roughness on the ability to measure the doubling of film thickness.

images were collected continuously. In order to minimize effects due to thermal drift, the system was maintained at $30.0 \pm 0.05^\circ$ using a Watlow (Winona, Mn.) heating element and controller. Figure 4.11a shows the change in height calculated from the unflattened raw data collected during this experiment. Each image was fitted to a plane and then the average distance between the first image (scan number 9) and each subsequent image was calculated. This analysis gives a film growth of $1.5 \pm 0.2 \mu\text{m}$ which, when added to the original film thickness of $1.2 \pm 0.1 \mu\text{m}$, gives an overall film thickness of $2.7 \pm 0.2 \mu\text{m}$ at the bottom of the discharge. Figure 4.11b shows the results of monitoring the RMS roughness of the AFM images collected during the discharge. The samples studied in this section were sputter-deposited at 3M. In order to improved adhesion, an initial layer of Cu (approximately 10 nm) was first deposited. Following, a $1.2 \mu\text{m}$ layer of $\text{Si}_{0.66}\text{Sn}_{0.34}$ was deposited. Since we did not get a direct measurement of the RMS roughness of the Cu layer, the value of $\sigma_s = 10 \pm 0.1 \text{ nm}$ found from averaging the RMS roughness of the stainless steel substrate

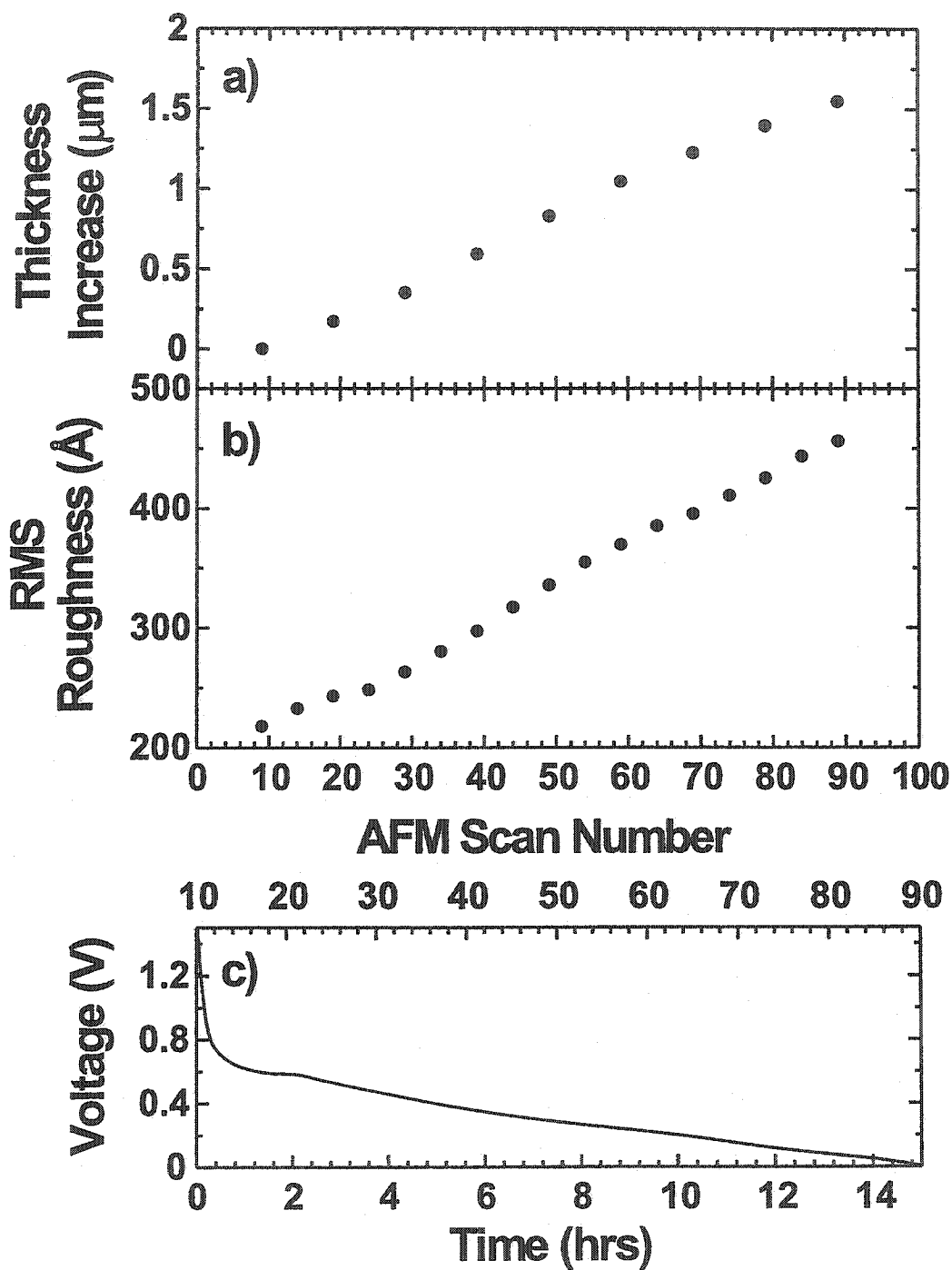


Figure 4.11: Change in height of $\text{Si}_{0.66}\text{Sn}_{0.34}$ occurring during the first discharge measured using a) the raw data, b) the change in surface RMS roughness compared to c) the voltage curve collected during the experiment.

measured from several samples was used. Hence, the analysis presented above gives a value of $\alpha = 2.1 \pm 0.2$ using $q = 0.52 \pm 0.06$. Applying this value to the initial thickness gives an overall thickness of $2.6 \pm 0.2 \mu\text{m}$ which agrees well with the results obtained from monitoring the piezo in the scanner.

The advantage of using the roughness measurements to extrapolate the thickness changes over that of monitoring the contraction and/or elongation of the piezo ceramic in the scanner is that roughness changes are independent (up to a limit) of thermal changes. For example, the geometry of our system is such that the sample is held beneath the scanner by three stainless steel supports approximately 1 cm in length. A one-degree change in temperature can cause linear expansion in these supports of over 100 nm. This elongation is then transmitted directly to the piezo as it tries to maintain a constant force of the cantilever on the sample (in the case where constant force contact mode is being used) and is registered as a spurious sample growth. However, as long as the sample is still within reach of the scanner, the roughness measurements are completely unaffected by changes in temperature.

For the sake of completeness, tip effects on our roughness measurements have also been considered. All AFM images are a convolution of the actual surface of the sample and the shape of the cantilever tip. It can easily be shown that for samples with small surface features, the measured roughness is much smaller than the actual surface roughness [96]. Figure 4.12 shows a typical cross section of an AFM image of one of our $\text{Si}_{0.66}\text{Sn}_{0.34}$ films and a sketch of the tip, to scale. The size of the predominant surface features is in the micrometer range, while the radius of the tip is in the 40 nm range. It is clear that the finite radius of the tip is not influencing the measurements.

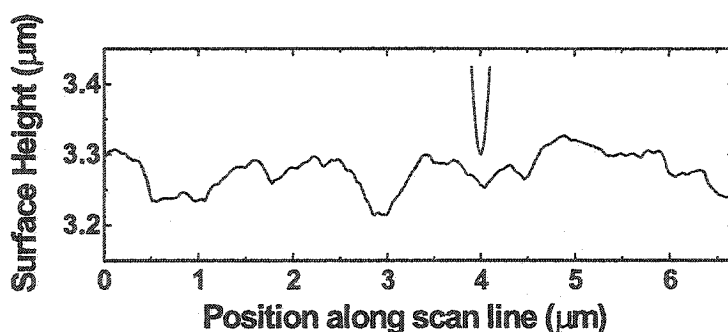


Figure 4.12: Cross-section of an AFM image compared to an AFM tip described by a parabola with a 40nm radius apex.

In this section we have shown, using a simple experiment and analysis, that AFM roughness measurements can be used to infer film thickness changes, in cases where the film thickness changes proportionally at all points of the film. However, the roughness of the substrate on which the film is initially deposited is an important factor to be considered, for it influences the experimental results profoundly. When quantitative results are needed, the use of smooth or previously well-characterized substrates is recommended. In the next section we develop a better method to measure total volume changes of electrode materials.

4.2.2 Volume Changes from Patterned Surfaces

In the previous section we showed how to calculate the change in thickness of a thin $\text{Si}_{0.66}\text{Sn}_{0.34}$ film as it reacts with Li. The goal of this work, however, is to measure total volume changes of small sized electrode materials. This, we believe, would give us a better indication of how powdered samples would behave in an actual battery

electrode. In order to measure these volume changes, patterned samples were prepared by using a fine mesh (SPI supplies, West Chester, PA. $7.6 \times 7.6 \mu\text{m}$ square openings as shown in figure 4.13) as a sputtering mask. Since the sputtering process is not as ballistic as expected, the mesh had to be held in perfect contact with the surface of the substrate. Figure 4.14 shows a schematic representation of the holder used to prepare

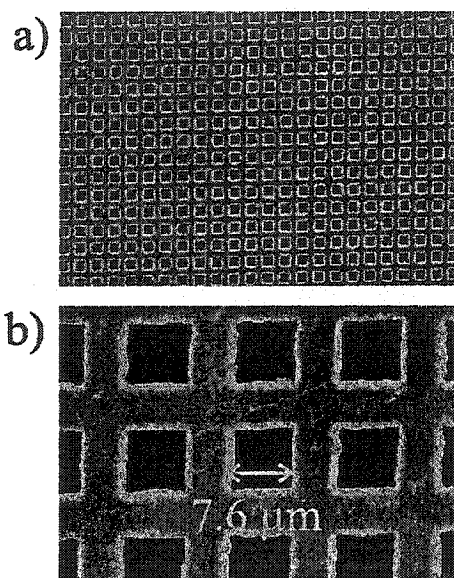


Figure 4.13: Mesh used to produce patterned electrode materials.

patterned electrodes. The shop-made holder presses the mesh onto the substrates with a coarse concave-shaped grid. Since the concave grid has larger openings than the mesh, the atoms or clusters of atoms ejected from the target during the sputtering process can travel through the grid and on the mesh or through the openings of the mesh onto the substrate.

Volume Corrections

In section 3.1.3 we showed how an AFM with a finite-sized tip would interpret a single square step. During the imaging process samples are tilted in space, typically on the

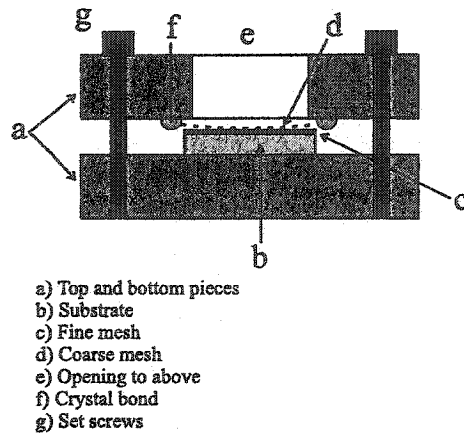


Figure 4.14: Assembly for making patterned surface electrodes.

order of about 1 to 2 degrees, as shown schematically in figure 4.15a. In such a case, the AFM topograph would appear skewed as shown in figure 4.15b. Therefore, in

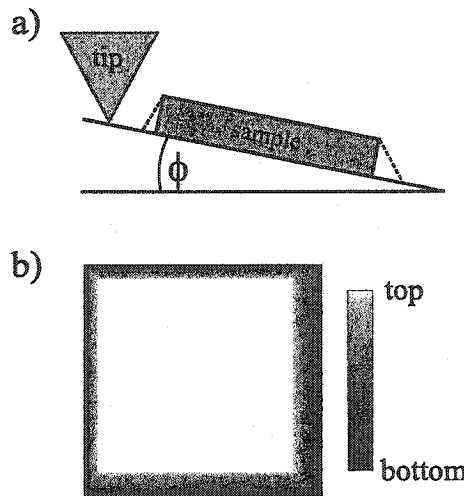


Figure 4.15: a) Schematic representation of an AFM tip and a square pulse sample inclined by an angle ϕ . b) Schematic representation of an AFM topograph of a tilted square pulse sample.

order to understand the measured volume changes we calculate the change in volume of the object shown in 4.15b.

Consider a square step sample of height h , width w , and length l . Assume the sample is tilted in two mutually orthogonal directions by angles φ and β . Lastly, let

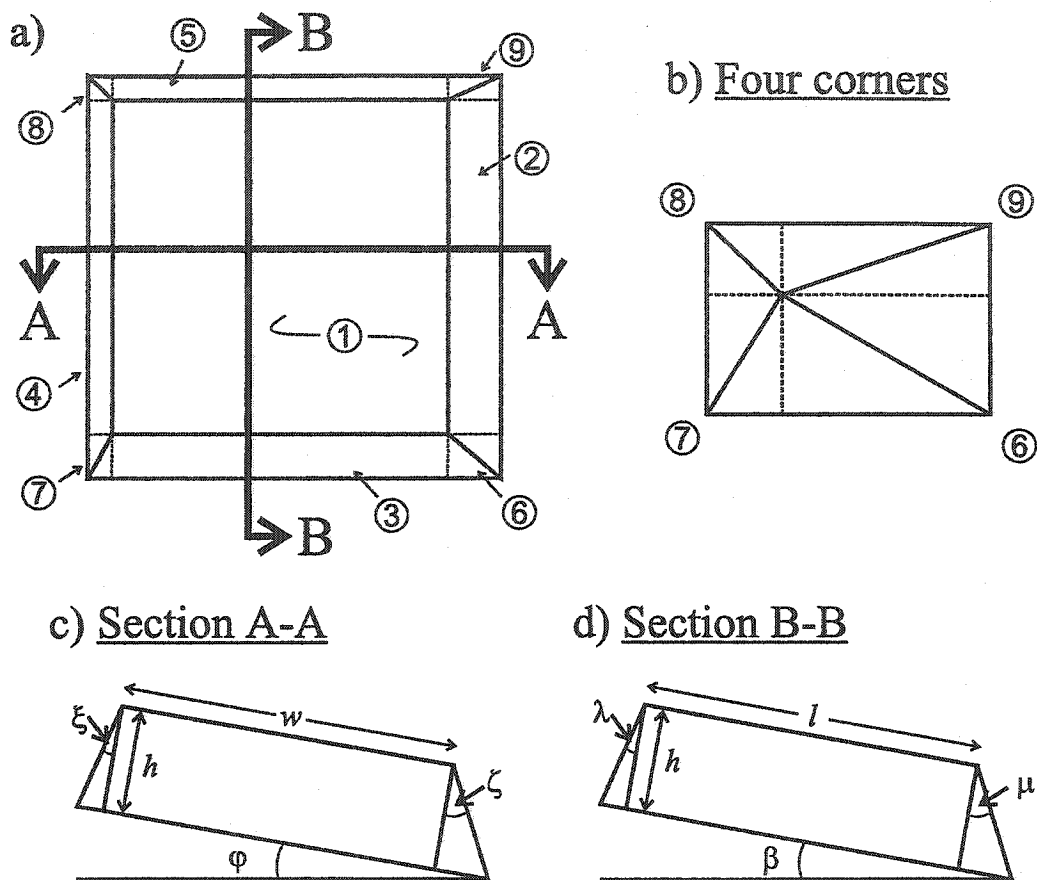


Figure 4.16: Volume analysis of a square pulse as seen with an AFM. a) Schematic representation of an AFM image of a square pulse. b) Four corners of the measured volume shown in a). c) Cross-section A-A d) Cross-section B-B.

the AFM tip have a half-angle of θ . The measured volume of the square pulse can be broken down into 9 regions as shown schematically in figure 4.16. The volume of

the first five areas is given below:

$$\begin{aligned}
 \text{Region 1} &= hwl \\
 \text{Region 2} &= \frac{1}{2}wh^2 \tan(\lambda) \\
 \text{Region 3} &= \frac{1}{2}wh^2 \tan(\mu) \\
 \text{Region 4} &= \frac{1}{2}lh^2 \tan(\xi) \\
 \text{Region 5} &= \frac{1}{2}lh^2 \tan(\zeta)
 \end{aligned} \tag{4.7}$$

where $\xi = \theta + \phi$, $\zeta = \theta - \phi$, $\mu = \theta + \beta$, and $\lambda = \theta - \beta$. Regions 6 to 9 are the four corners of the AFM topograph. As shown in figure 4.16b, the four corners form a pyramid of height h . The volume of the pyramid can be calculated by summing the cross-sectional areas perpendicular to the height in the following way:

$$\begin{aligned}
 V_p &= \int_0^h (\tan(\lambda) + \tan(\mu))(\tan(\xi) + \tan(\zeta))x^2 dx \\
 &= \frac{1}{3}(\tan(\lambda) + \tan(\mu))(\tan(\xi) + \tan(\zeta))h^3
 \end{aligned} \tag{4.8}$$

Using equations 4.7 and 4.8, the total volume of the square step as measured by the AFM is given by:

$$\begin{aligned}
 \text{Volume} &= lwh + \frac{1}{2}lh^2(\tan(\xi) + \tan(\zeta)) + \frac{1}{2}wh^2(\tan(\mu) + \tan(\lambda)) \\
 &\quad + \frac{1}{3}(\tan(\lambda) + \tan(\mu))(\tan(\xi) + \tan(\zeta))h^3
 \end{aligned} \tag{4.9}$$

Figure 4.17 shows a plot of the percent error of the measured volume (calculated by $100 \times (\text{measured volume} - \text{real volume}) / (\text{real volume})$) as a function of the tower

height for the case where $\theta = 35^\circ$, $l = w = 10 \mu\text{m}$, $\phi = 1.0^\circ$ and $\beta = 1.5^\circ$. As can be seen, for a height of about 500 nm, the error on the volume is about 7 percent. In our measurements we desire to reduce as many sources of error as possible. Fortunately, the percent volume change of equation 4.9 as a function of the height h is the same as the percent volume change of real volume = hwl . Therefore, in what follows we will quote percent volume and percent height changes. Also, the percent volume change is irrespective of the actual height measured by the AFM which can be inaccurate if the AFM scanner is not properly calibrated.

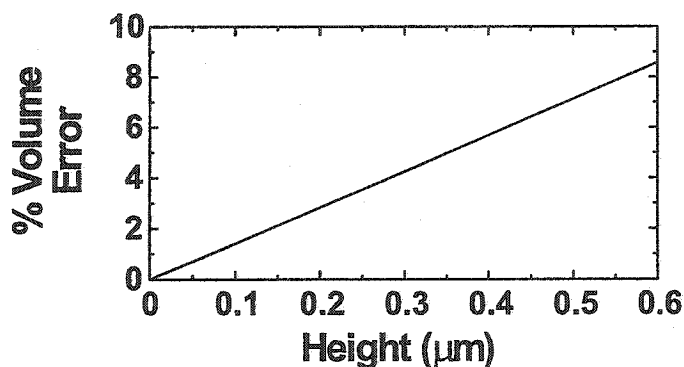


Figure 4.17: Percent volume error of a square step as measured with an AFM plotted versus the height of $10 \times 10 \mu\text{m}$ square step.

4.3 Volume Changes of Patterned α -Si Electrodes

Si samples were prepared by RF magnetron sputtering on highly polished stainless steel substrates. To prepare patterned electrodes, the substrates were mounted in the holder shown in figure 4.14. Si was also sputtered on Cu foil for x-ray diffraction analysis and for electrochemical testing in standard coin cells.

Figure 4.18 shows the x-ray diffraction pattern of sputtered Si on Cu foil. As shown by upside down triangles, the Si sample is amorphous (α -Si). The sharp peaks

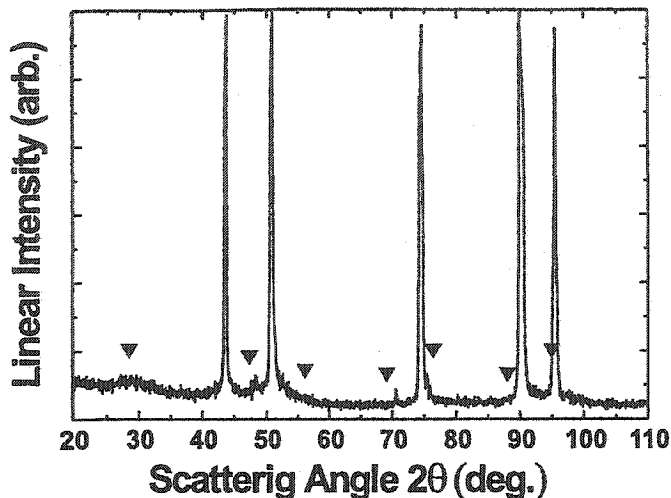


Figure 4.18: X-ray diffraction pattern of an *a*-Si film. Sharp peaks come from the Cu substrate on which the film was deposited.

in figure 4.18 come from the Cu foil substrate. Figure 4.19 shows the voltage versus capacity (4.19a) and capacity versus cycle number (4.19b) for *a*-Si cycled versus Li metal. The voltage profile of a Li/*a*-Si cell is very similar to the voltage profile of the Li/Si_{0.66}Sn_{0.34} cell shown previously. However, unlike Si_{0.66}Sn_{0.34}, *a*-Si does not show good capacity retention.

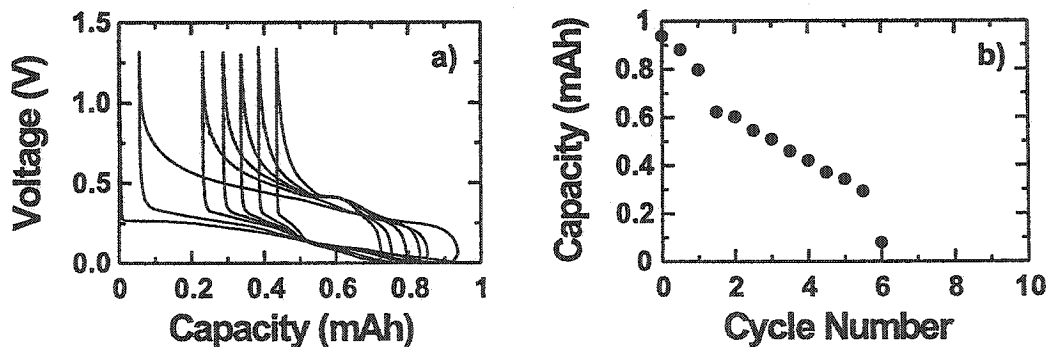


Figure 4.19: a) Voltage versus capacity and b) Capacity versus cycle number for a Li/Si cell.

Since Si reacts so readily with oxygen, elemental analysis was performed on an α -Si tower. Energy dispersive spectroscopy (EDS) was used to detect Si (from the sample), Fe and Cr (from the substrate) and wavelength dispersive spectroscopy (WDS) was used to detect O. Figure 4.20a shows an SEM secondary electron micrograph of a Si tower. Figure 4.20b shows the atomic percentage of Si (left ordinate) shown by rhombuses and the atomic percentage of oxygen (right ordinate) shown by circles. For clarity, the atomic percent of Fe and Cr have been omitted. The white dots in 4.20a show the approximate size ($1\ \mu\text{m}$) and location where the electron beam interrogated the sample. The size of the white circles also show the approximate diameter of the electron beam used during the analysis. As can be seen from figure 4.20b there is only a minute amount of oxygen present in the sample. It is unlikely that oxygen is only located on the right hand side of the sample. The reason why oxygen is only detected on a single side is probably due to the location of the diffraction crystal in the WDS spectrometer.

Figure 4.21 shows topographic images taken during an *in situ* AFM experiment performed on a Li/ α -Si cell. In order to view the towers more easily, the AFM topographs have only been tilted instead of flattened. The maximum value of the contrast scale as well as the approximate height of each tower is given in table 4.2.

The α -Si towers appear to be smooth and show virtually no lateral changes from the reaction with Li. Because of the vertical contrast scales of these AFM topographs are all from dark (minimum height) to light (maximum height), it is not possible to observe the change in height of the tower. This information can only be obtained from an analysis of the AFM topographs.

Figure 4.22 shows the results from the analysis of the *in situ* AFM experiment

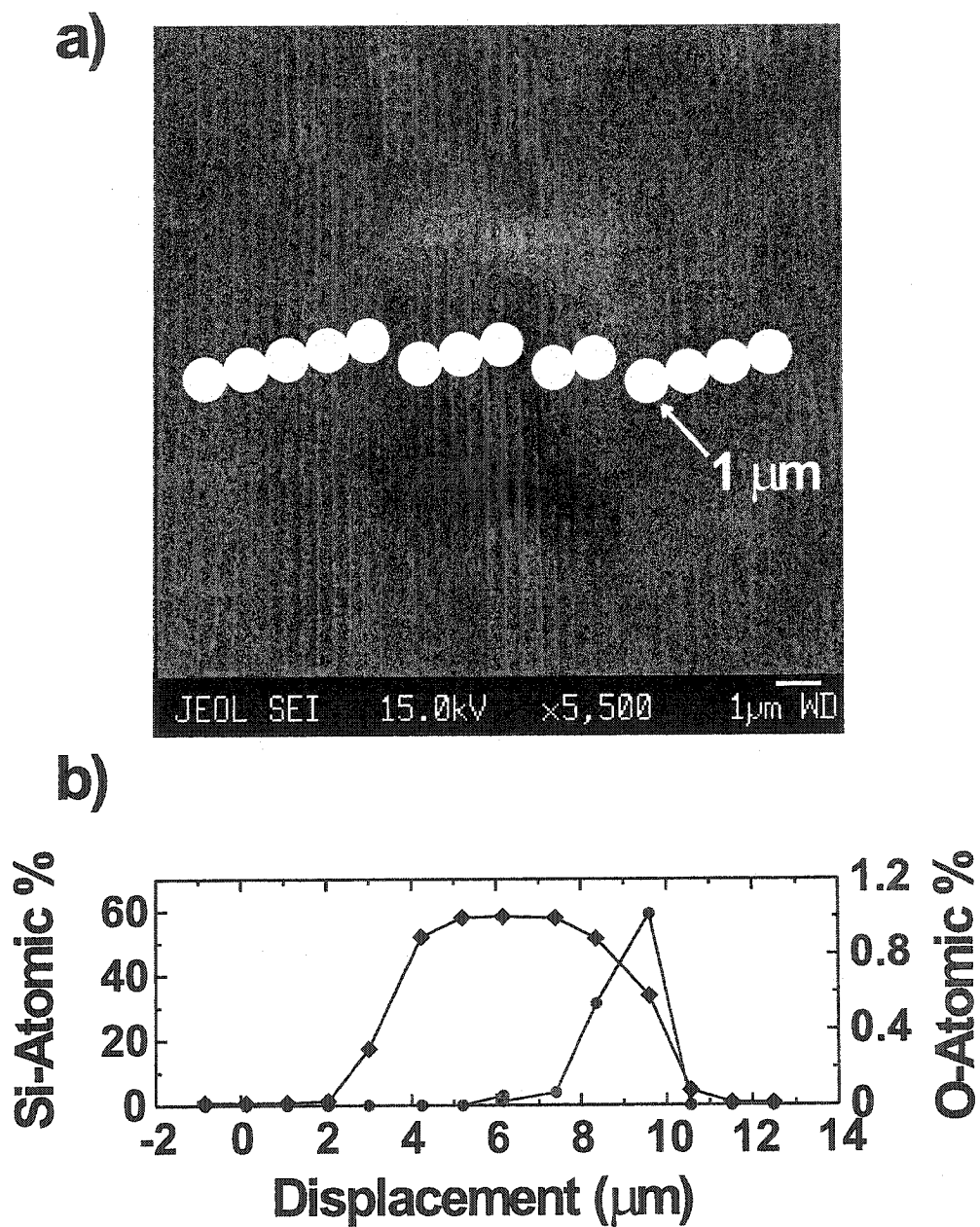


Figure 4.20: Elemental analysis of an α -Si tower. a) scanning electron micrograph of a Si tower. The white dots show the approximate location and size of the electron beam. b) Amount of Si and O in the sample. The contributions of Fe and Cr are not shown.

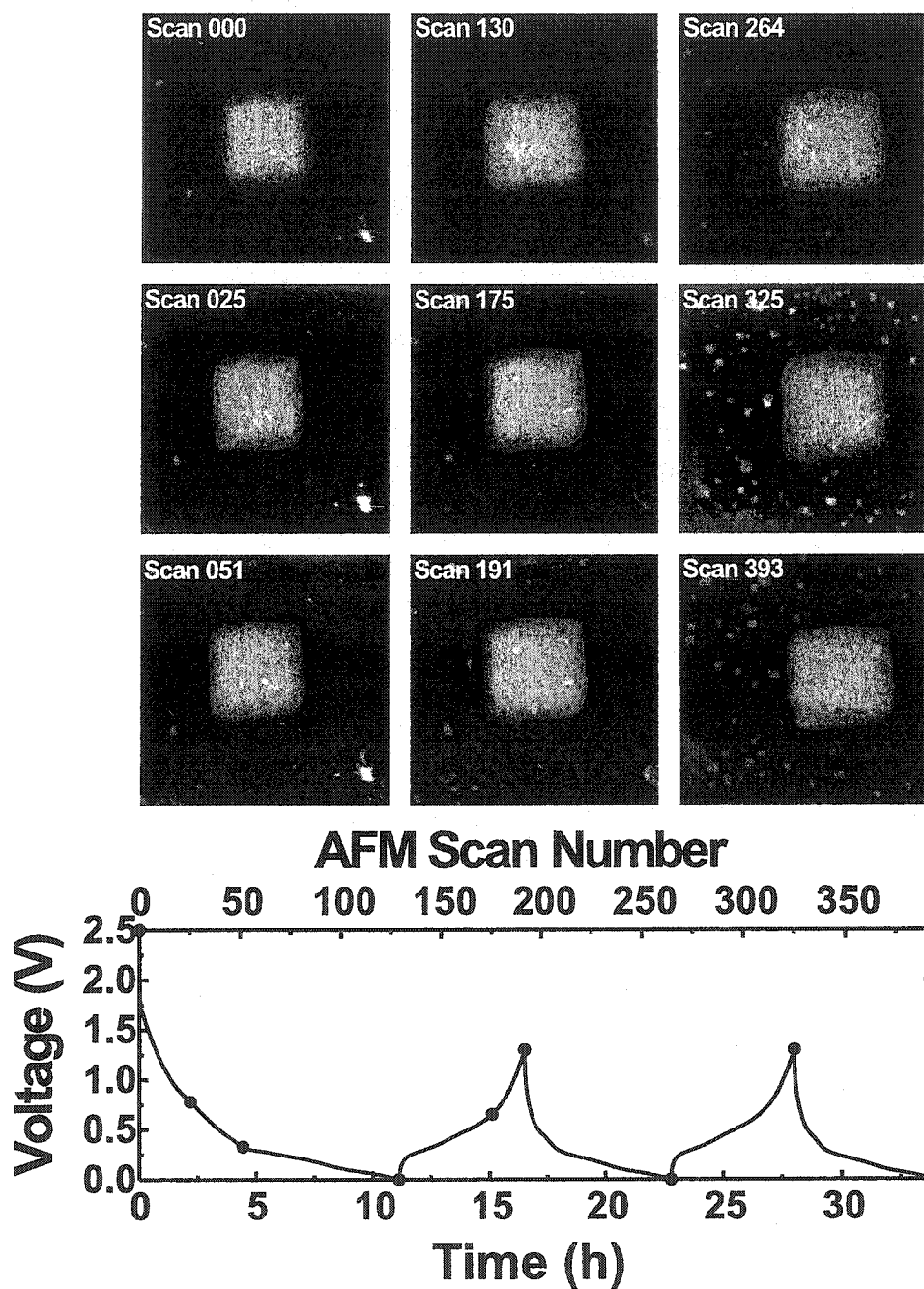


Figure 4.21: Topographic images obtained from an *in situ* AFM experiment on a patterned *a*-Si sample. The solid dots on the voltage versus time (bottom abscissa) and AFM scan number (top abscissa) curve shows the state of charge where the AFM topographs were obtained.

Table 4.2: Height changes of a Si tower as it reacts with Li.

AFM Number	Maximum height	Approximate Height of Tower
000	280 nm	210 nm
025	235 nm	215 nm
051	240 nm	221 nm
130	850 nm	757 nm
175	320 nm	303 nm
191	260 nm	249 nm
264	900 nm	742 nm
325	320 nm	254 nm
393	1000 nm	715 nm

shown in figure 4.21. Panel 4.22a, b, and c show the change in area, height and volume respectively, undergone by the tower during the reaction with lithium compared to the voltage profile shown in figure 4.22d. The first discharge (4.22d) shows a spurious capacity during which no change in height or volume is detected. As we discuss below, this irreversible capacity comes from various components of the wetcell. The fact that there is no change in both height and volume makes this argument probable. The change in height and volume are a direct function of the lithium content in the electrode. Figure 4.22 also shows that the α -Si electrode does not return to its initial volume after the first cycle. The change in volume obtained from this experiment is approximately 300%. In crystalline Si, each Si atom occupies a volume of 20 \AA^3 [†]. When Si reacts with Li to form $\text{Li}_{4.4}\text{Si}$, each Si atom occupies a volume of 82 \AA^3 . This represents a 311% volume expansion. This value is consistent with that measured on α -Si.

As mentioned above, the first discharge of patterned α -Si cycled versus Li is very

[†]Amorphous Si adopts a short range diamond structure similar to crystalline Si. Therefore assuming each Si atom occupies the same volume in α -Si as in crystalline Si is a fair approximation.

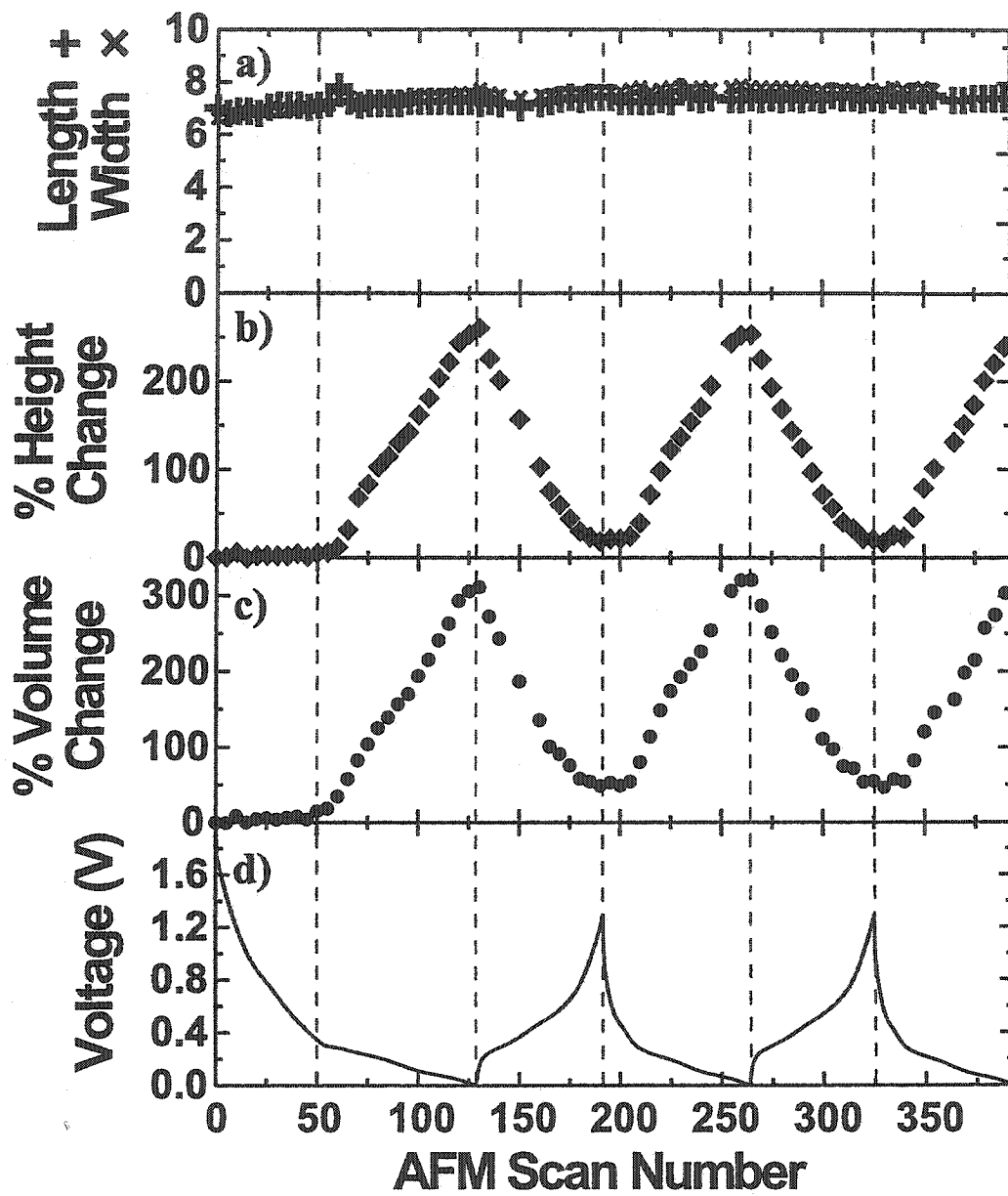


Figure 4.22: Change in a) Length (+) and width ((x)) b) height c) volume of the *a*-Si tower shown in figure 4.21 compared to d) voltage versus AFM scan number.

different from that of an *a*-Si film cycled versus Li measured in a coin cell. As can be seen from figure 4.23, the voltage of the patterned electrode is much higher for the first half of the discharge. In a standard coin cell, approximately 6 drops of electrolyte are used, whereas in our wet cell, approximately 1 ml of electrolyte (about 80 drops) is used. Also, coin cells are typically cycled with currents on the order to 20 μ A. The patterned electrodes that we study are cycled at approximately 2 to 5 μ A. Therefore, any contaminations in our electrolyte, which would not be noticeable in coin cell data, would be amplified many times over in our wet-cell. It is also suspected that the Cu current collector may be a source of the irreversible capacity. Previously, part of the

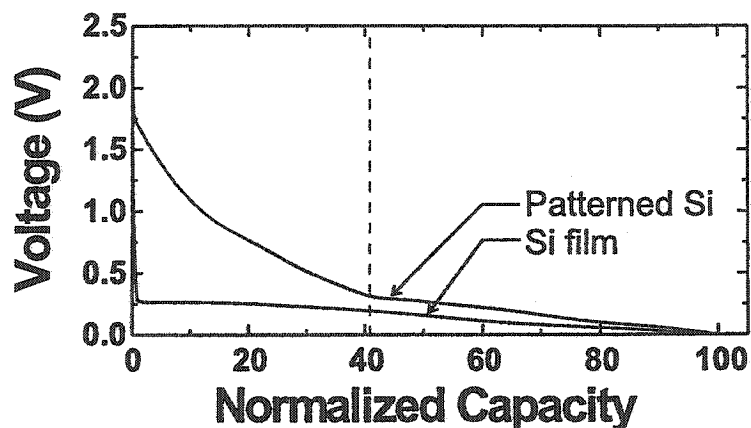


Figure 4.23: Comparison between the voltage curve of a coin cell made from a *a*-Si film and an *a*-Si patterned electrode cycled in our AFM wetcell.

cleaning procedure for our wet-cell involved drying it in an oven at approximately 80-100°C for several hours in order to remove the moisture from the washing process. Unfortunately, heating the wet-cell at these temperatures favors the formation of CuO

on the Cu foil. During the initial discharge, lithium therefore reacts irreversibly with the oxygen at the surface of the current collector.

4.4 Volume Changes of Patterned Sn Electrodes

Recently it has been reported that pure Sn, (made by electrodeposition, sputtering, and powdered Sn from different manufacturers) when allowed to react with lithium, acts as a catalyst for the decomposition of electrolyte [97, 98, 99]. In this section we will show, using *in situ* atomic force microscopy, the decomposition of electrolyte on the surface of pristine Sn. We will also show, using the method described in reference [97], how the decomposition process can be “bypassed” enabling the volume changes of Sn to be measured.

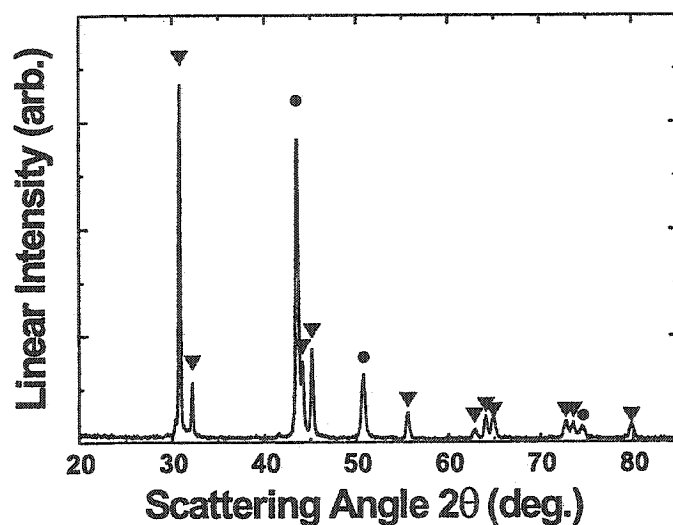


Figure 4.24: X-ray diffraction pattern of Sn on Cu foil. The Diffraction peaks of Sn are shown by upside down triangles while those of Cu are shown by solid dots.

Sn electrodes were made by sputter deposition on stainless steel substrates and on Cu foil. Figure 4.24 shows the x-ray diffraction pattern of sputtered Sn on Cu foil.

The sputtered Sn is crystalline, giving sharp diffraction peaks shown by triangles. The other diffraction peaks shown by solid dots come from the Cu foil used as the substrate.

Patterned Sn samples were also prepared using the method described above. Figure 4.25a shows an SEM secondary electron micrograph of patterned Sn. The surface morphology of Sn is quite different than *a*-Si shown in the previous section. The features of the Sn towers are a result of the fact that Sn is a strong diffuser and prefers to aggregate in large clusters of Sn. This is exactly as shown by reference [35]. Figure 4.25b shows an SEM backscatter image of patterned Sn taken at a slightly larger magnification. Since Sn has more electrons than both Fe and Cr (in the substrate), it appears bright in an SEM backscatter image. Therefore, from figure 4.25b we see that there is no Sn between the towers.

In order to detect any oxygen, electron probe analysis was performed on the same sample. Figure 4.26 shows a compositional analysis of a single Sn tower. As above, energy dispersive spectroscopy was used to detect Sn, Fe, and Cr while wavelength dispersive spectroscopy was used to detect oxygen. Figure 4.26a shows the SEM micrograph of a Sn tower as well as the position and approximate size of the electron beam. Figure 4.26b shows the atomic percentage of Sn (left ordinate) and oxygen (right ordinate). In this graph the atomic percentage of Cr and Fe are not shown. Figure 4.26b shows there is no detectable oxygen in our Sn samples.

We now discuss the electrochemical reaction of Li with Sn in an organic electrolyte. As mentioned above, when Sn is allowed to react with Li electrochemically, the surface of Sn acts as a catalyst for the decomposition of Sn. It is proposed that this decomposition occurs until a thick layer of electrolyte byproducts is formed on

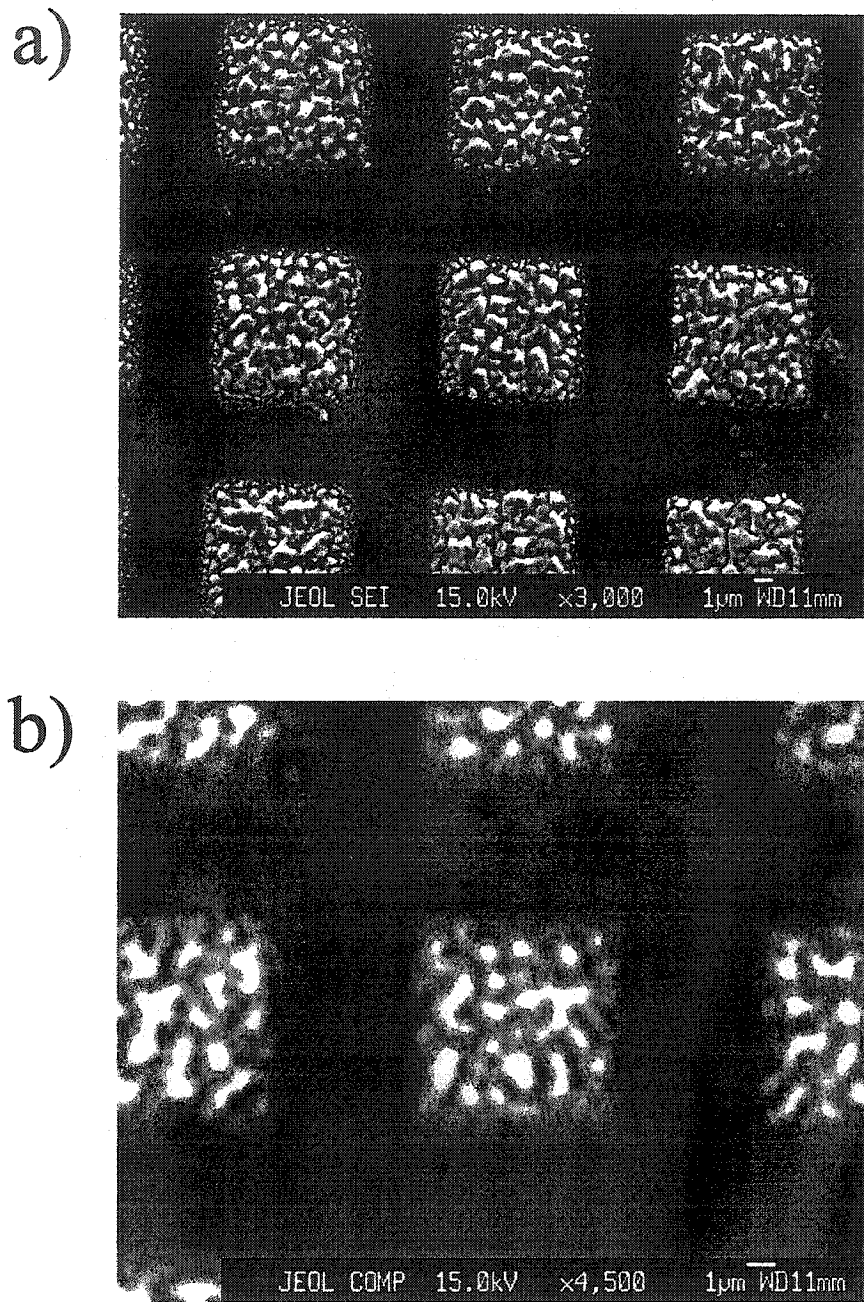
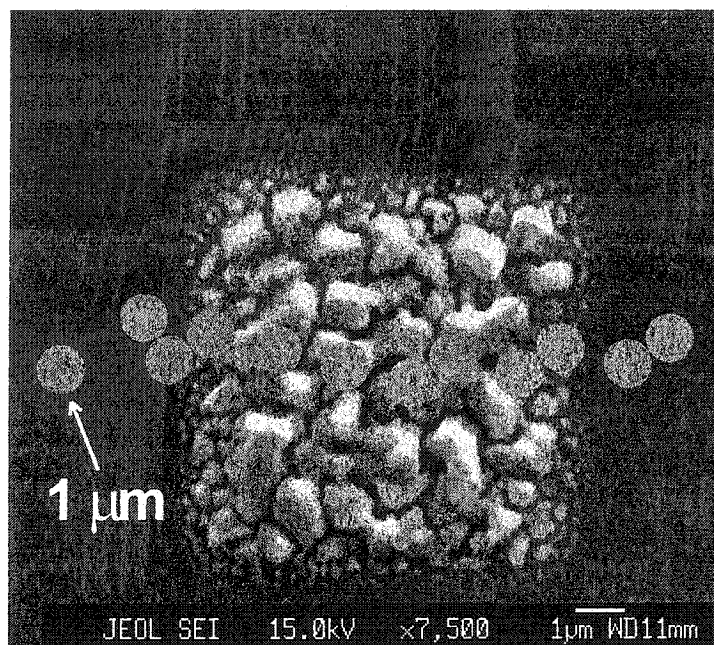


Figure 4.25: a) SEM secondary electron image of patterned Sn.
b) SEM backscattered image of pattern Sn

a)



b)

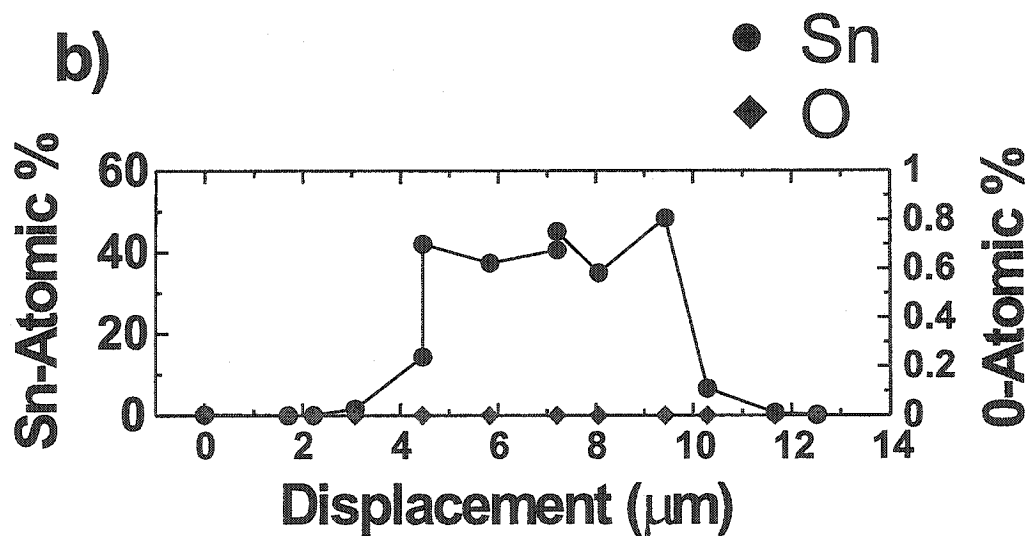


Figure 4.26: Electron probe analysis of a Sn tower. a) Solid dots on the SEM micrograph show the approximate size and position of the electron beam used to interrogate the sample. b) Atomic percent Sn and atomic percent O in the Sn tower. The contributions of Fe and Cr are not shown.

the surface of Sn which then prevents any future decomposition. In other words, the decomposition process is not a function of the amount of electrolyte present in the cell. Once formed, this layer then acts as a passivating film which retards (but not prevents) the further reaction of Li with Sn. Below we give an example of this reaction using sputtered Sn on a stainless steel substrate.

Figure 4.27 shows the results of an *in situ* AFM experiment, taken at 3M, performed on a Sn film sputtered on a stainless steel substrate. The voltage versus time (bottom abscissa) and AFM scan number (top abscissa) shows the voltage profile as it is now understood. The first part of the voltage profile shows a long plateau at approximately 1.6 V. The decomposition of electrolyte occurs during this plateau. Once a sufficiently thick passivating layer is formed, the voltage profile of Sn progresses as expected normally. The top of figure 4.27 shows three of the AFM topographs taken during the early stages of discharge. The time at which images 000, 025, and 056 were taken is shown on the voltage curve by solid dots. As shown by the labels on the AFM images, the change in morphology of the AFM images from 000 to 056 is accompanied by a large change in surface height. The contrast scale from dark to light of image 000 is 0 to 136 nm. As lithium reacts with the Sn electrode, the surface features increase as shown in images 025 and 056 where the contrast scale is 0–460 nm and 0–660 nm respectively. After scan 056 it was not possible to take proper images of the Sn surface due to the increased changes in surface height. These same results have also been observed in other experiments performed on both sputtered and electroplated Sn.

In their work, Beattie *et al.* proposed that the decomposition of electrolyte could be bypassed if the cell was first discharged quickly to approximately 0.8 V. At this

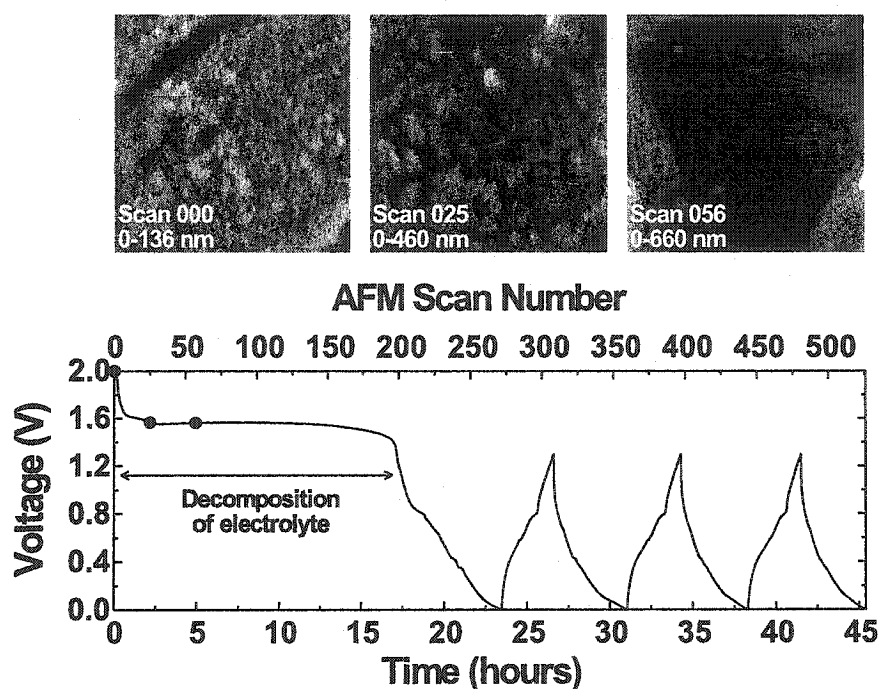


Figure 4.27: The reaction of Sn with lithium shows the decomposition of electrolyte. AFM images show the change in morphology of the Sn surface. The voltage profile of the Li/Sn cell shows the irreversible capacity due to the decomposition process of electrolyte.

point, the first Li-Sn phase, Li_2Sn_5 , is formed which does not act as a catalyst for the decomposition of electrolyte. Attempts were made to study Sn films but unfortunately keeping the film at 0.8 V resulted in the formation of bubbles due to the high current densities which had to be used. These bubbles interfered in the AFM scanning process making it impossible to image the surface of the Sn electrode. Therefore, patterned Sn electrodes were used. Since these electrodes have less sample, much lower currents were needed in order to maintain the electrode at 0.8 V.

Figure 4.28 shows the AFM images taken during the electrochemical reaction of

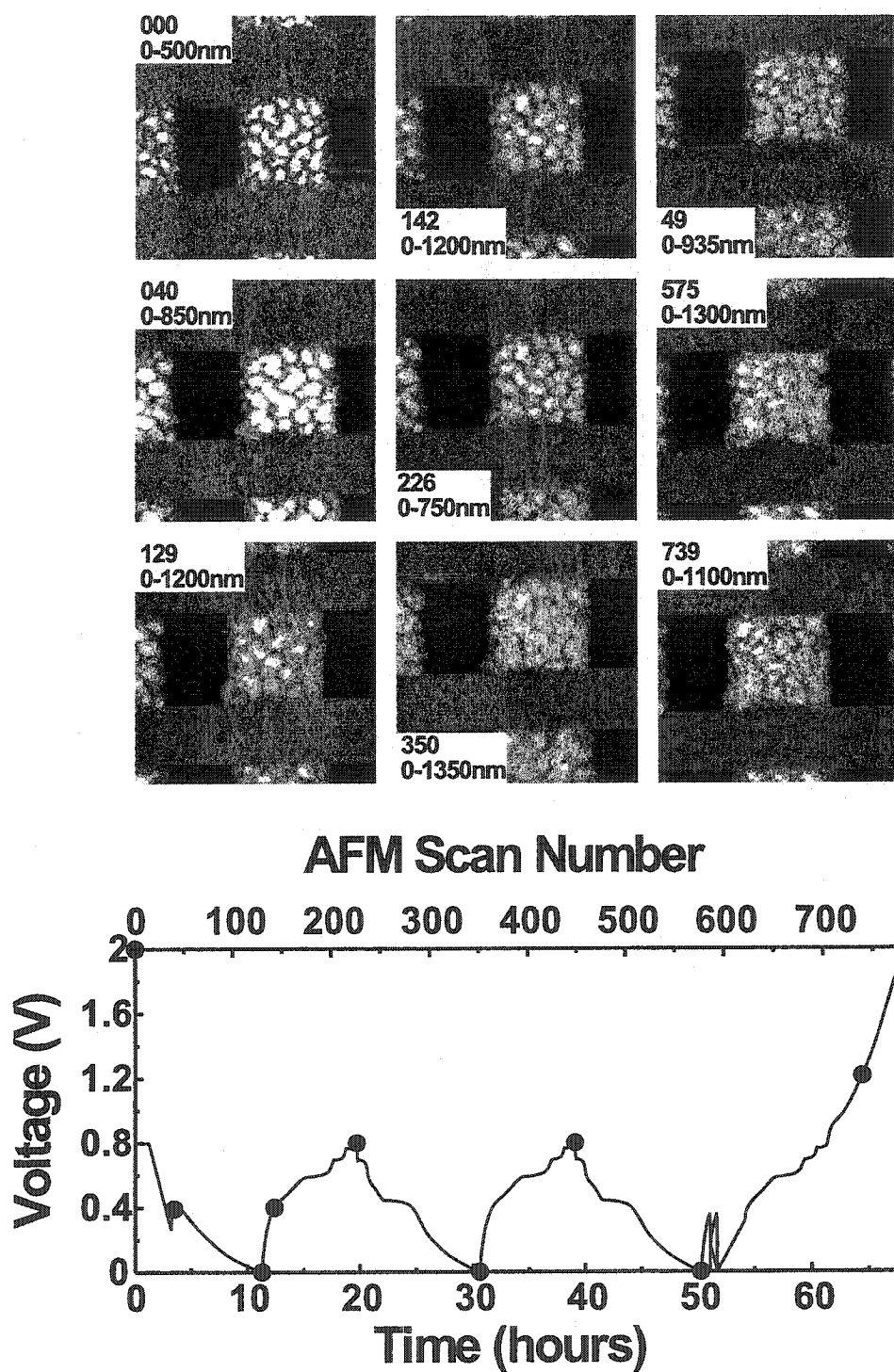


Figure 4.28: *In situ* AFM images taken during the electrochemical reaction of Li with patterned Sn. AFM images show the evolution of the Sn tower. The point at which each AFM images was taken is shown on the voltage versus both time (bottom abscissa) and AFM scan number (top abscissa) by solid dots.

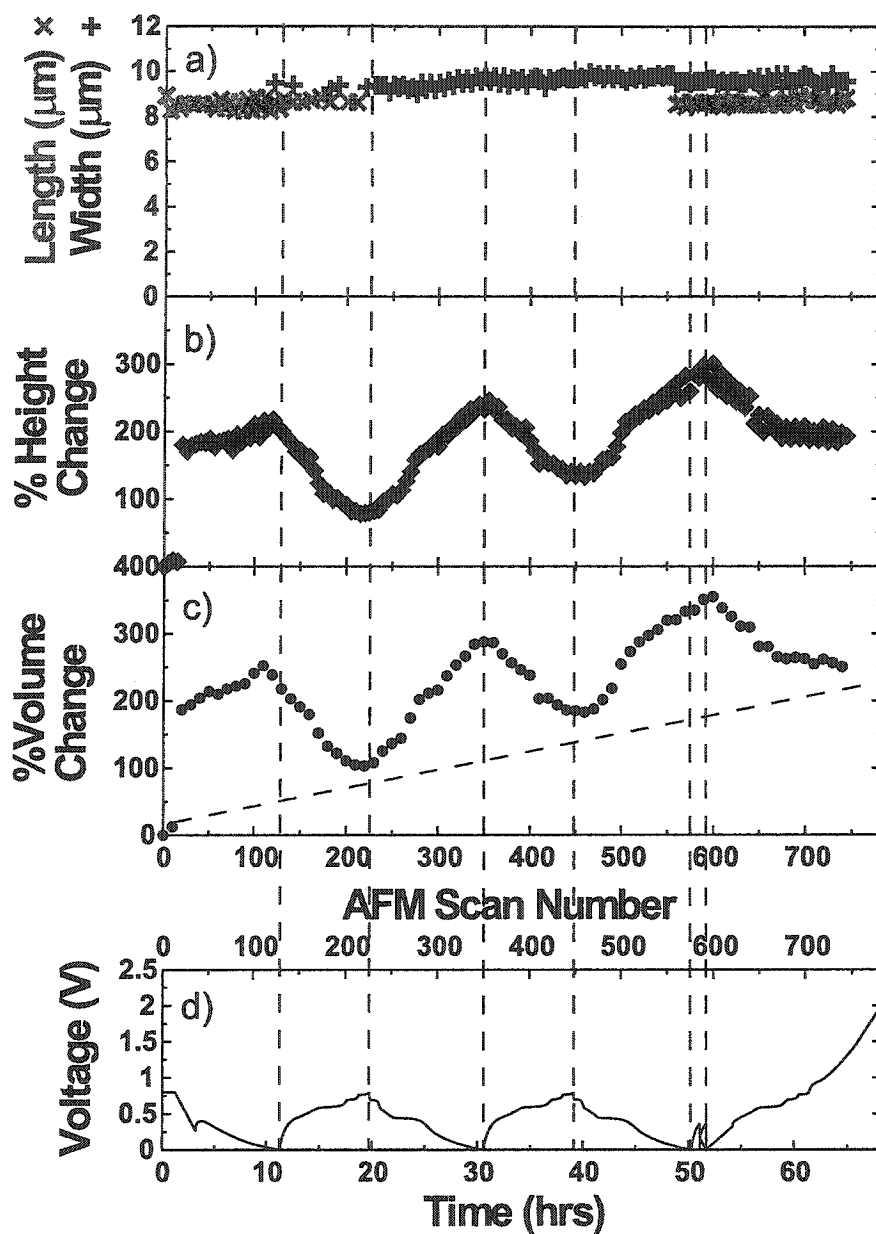


Figure 4.29: *In situ* AFM images taken during the electrochemical reaction of Li with patterned Sn. AFM images show the evolution of the Sn tower. The point at which each AFM images was taken is shown on the voltage versus both time (bottom abscissa) and AFM scan number (top abscissa) by solid dots.

could be observed when the cell's capacity goes to zero.

The constant change in the electrode surface can be seen when the AFM images collected at the top of charge (1.3 volts) are compared. Figure 4.30 shows images 000 (a and b), 226 (c and d), and 449 (e and f) in two and three-dimensional representation. Comparing these images shows that the features of the Sn tower become dilated in size as they press against each other. In the same manner, the three dimensional images (all shown with the same vertical scale and orientation), show how the electrode's height is also increasing. Because the cell was shorted in the early stages, a second experiment was performed on a patterned Sn sample.

Figure 4.31 shows the change in volume (4.31a) compared to the voltage curve (4.31) as a function of the AFM scan number. As in the previous case, the cell was held at a constant 0.8 V until the current was equal to $0.2 \mu\text{A}$, at which point the cell was discharged at a constant $0.2 \mu\text{A}$. After the first discharge cycle the cell was allowed to relax before it was discharged again. Subsequently, the cell was charged to 1.3 volts and again allowed to relax before undergoing the final discharge/charge cycle. The volume changes for this experiment show the same features as the previous results shown in figure 4.29. As lithium is inserted and then removed, the electrode does not return to its initial state.

A curious feature in the volume expansion of Sn as a function of lithium content is the steps as shown in figures 4.29 and 4.31. Figure 4.32 shows the volume change (figure 4.32a, solid dots) and voltage profile (figure 4.32b) of the first discharge taken from figure 4.31. In an attempt to explain the observed volume changes, the theoretical volume changes calculated from table 4.3 are shown in panel 4.32a by rhombuses connected by a solid line. Although the expected values of the percent volume changes

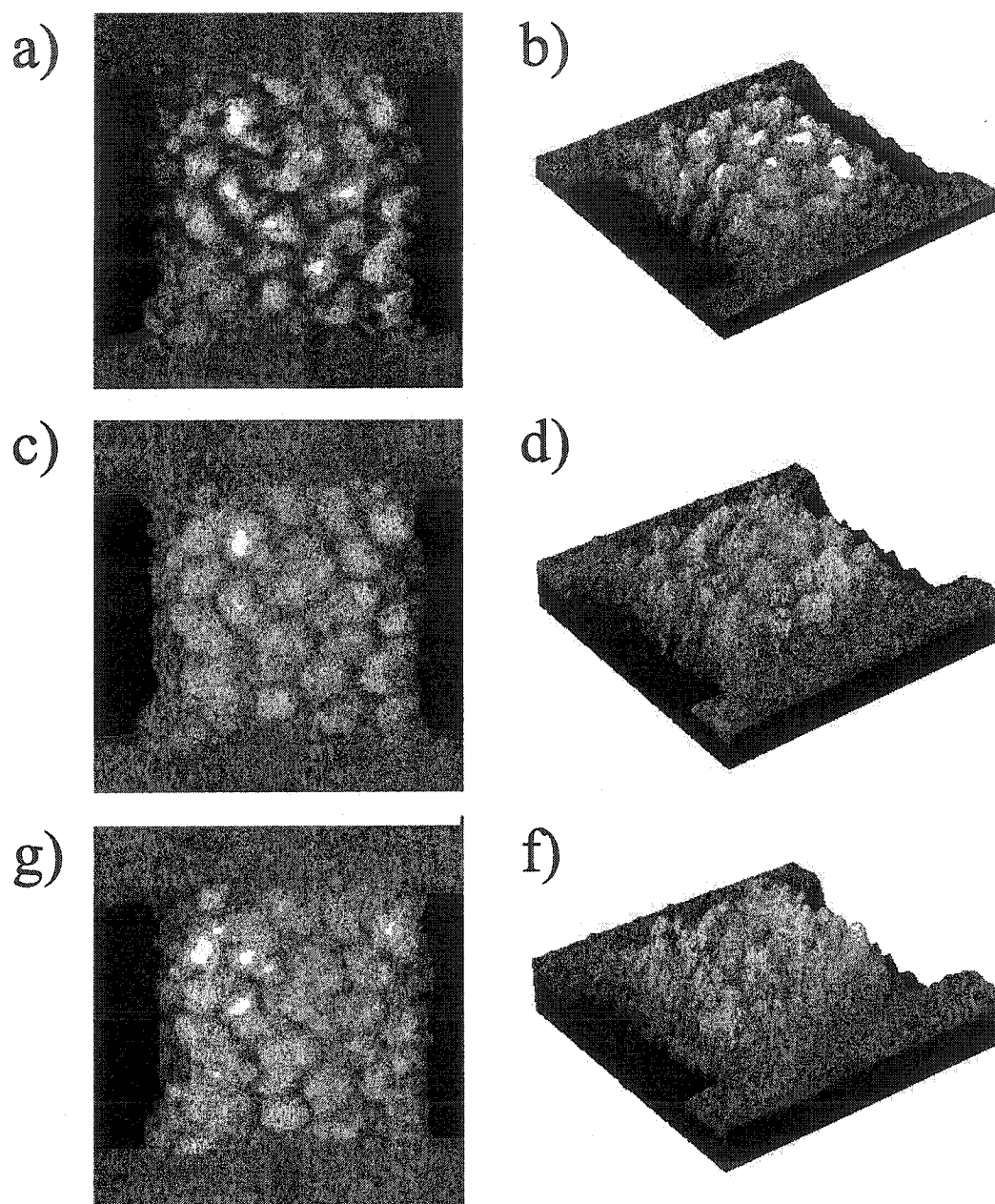


Figure 4.30: Selected AFM images from figure 4.29 show the change in morphology of the Sn tower. 2 and 3-Dimensional images of a) scan 000, b) scan 226, and c) scan 449.

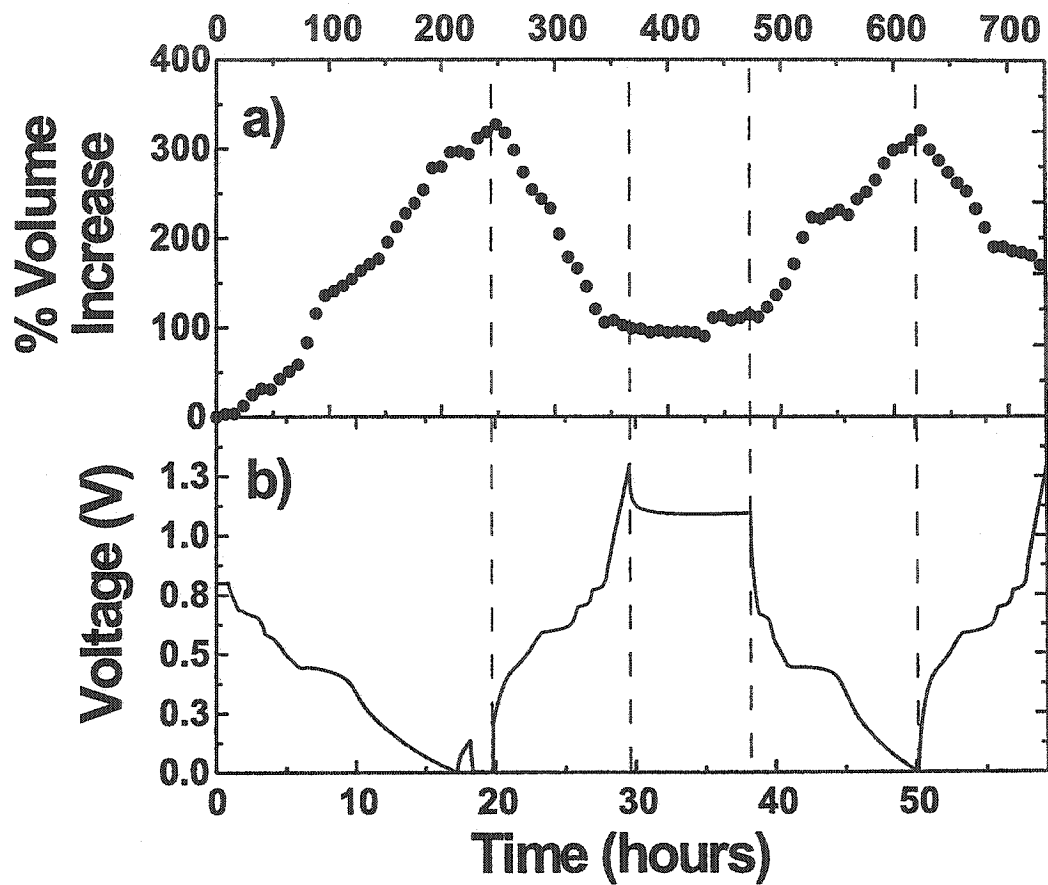


Figure 4.31: a) Change in volume of a Sn tower and b) voltage of a Li/Sn cell plotted versus time (bottom abscissa) and AFM scan number (top abscissa).

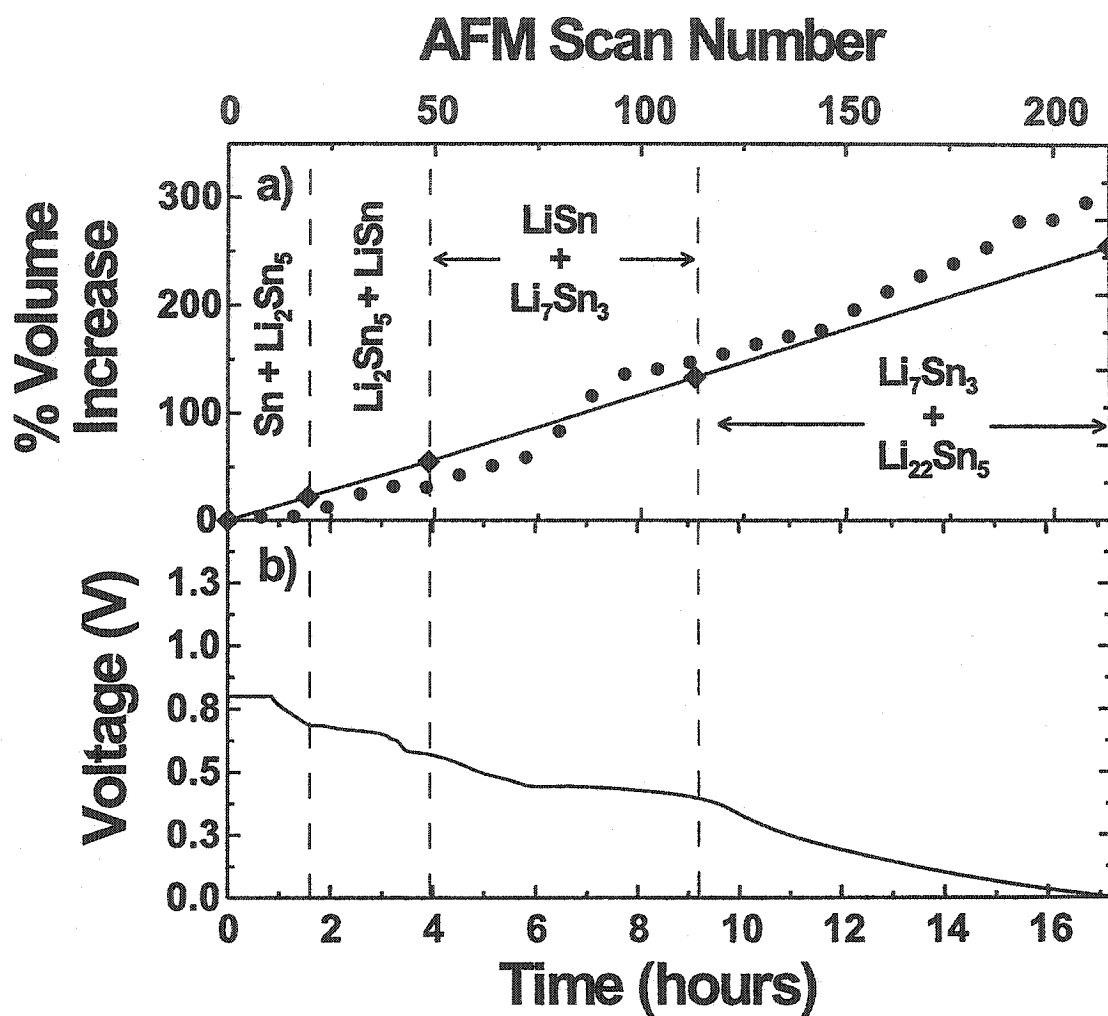


Figure 4.32: a) Comparison between the experimental volume change of a Sn tower (solid dots) to the theoretical volume changes based on the crystallographic volumes of the different Li-Sn alloys (rhombuses connected by a straight line) b) the voltage versus time (bottom abscissa) and AFM scan number (top abscissa) for a second in situ AFM experiment.

are close to the measured values, we suspect an as yet unknown mechanism causing

Table 4.3: Volume per Sn and percent depth of discharge for different Li-Sn phases.

Phase	Volume $\text{\AA}^3/\text{Sn}$	% of Discharge
Sn	27	0
Li_2Sn_5	33	9
LiSn	42	23
Li_7Sn_3	63	53
$\text{Li}_{22}\text{Sn}_5$	96	100

the altered profile of the measured volume change.

4.5 Volume Changes of Patterned Si-Sn Electrodes

Patterned Si-Sn samples were prepared by sputter deposition at Dalhousie University as described above. In order to ensure that the samples had the proper structure, samples were also deposited on Cu foil for x-ray analysis. Figure 4.33 shows the x-ray diffraction pattern of the Si-Sn samples. The x-ray diffraction pattern shows that the Si-Sn film is amorphous. The sharp peaks in figure 4.33 come from the Cu foil used as the substrate. Scanning probe microscopy was used to study the morphology and composition of our patterned Si-Sn materials. Figure 4.34a shows the secondary electron micrograph of a patterned Si-Sn electrode. As can be seen the towers are well formed. Figure 4.34b shows a backscatter image of the same towers. Since Sn in the Si-Sn towers has more electrons than both Fe and Cr from the substrates, the Si-Sn towers appear brighter in a backscatter image.

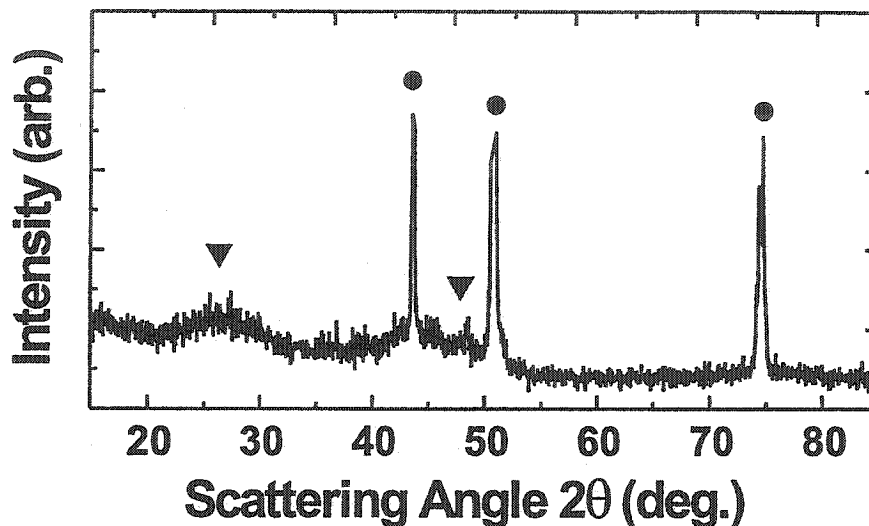


Figure 4.33: X-ray diffraction pattern of sputtered Si-Sn. Triangles show the position of the Si-Sn peaks while the dots show the position of the peaks from the Cu foil used as a substrate.

In order to measure the stoichiometry of the Si-Sn towers, energy dispersive spectroscopy was used to detect Sn, Si, Fe, and Cr while wavelength dispersive spectroscopy was used to detect O. Figure 4.35a shows a secondary electron micrograph of a Si-Sn tower. The white dots show the approximate size and position of the electron beam used to interrogate the sample. Figure 4.35b shows the atomic percentage of Sn, Si, and O across the tower. For clarity, the atomic percentage of Fe and Cr have been omitted. As can be seen from figure 4.35, the samples do not have the expected stoichiometry of $\text{Si}_{0.66}\text{Sn}_{0.34}$. These Si-Sn towers show only about 60 atomic percent Si. This different composition is not crucial since we are more interested in

the fact that the material is amorphous.

Figure 4.36 shows topographic images obtained from an *in situ* AFM experiment on a patterned $\text{Si}_{0.6}\text{Sn}_{0.4}$ sample cycled versus Li metal. Each image is approximately $24 \times 24 \mu\text{m}$ in size. The AFM image number and the vertical contrast scale is shown for each image. The voltage versus time (bottom abscissa) and AFM scan number (top abscissa) is shown at the bottom of figure 4.36. The Li/ $\text{Si}_{0.6}\text{Sn}_{0.4}$ cell was initially discharged to 0.0 V and then held at 0.01 V for 1 hour to assure maximum capacity. At 0.0 V Li begins to plate on the surface of the electrode; therefore, to prevent this, the cell was held at 0.01 V. The solid dots on the voltage curves indicate the positions where the AFM images were taken. As can be seen by the dark area between the towers, the images show the effects of the piezo hysteresis discussed in the previous chapter. The surface of the tower is smooth and flat and shows no change in morphology due to the reaction with lithium. The only change suffered by the $\text{Si}_{0.6}\text{Sn}_{0.4}$ towers is in the direction perpendicular to the substrate.

Figure 4.37 shows the analysis of the *in situ* experiment shown in figure 4.36. Panel 4.37a shows the change in area of the tower as a function of AFM number. Because of the surface features on the left-hand side of the tower, it was not possible to obtain a reliable measure on the width of the tower. Therefore, the area shown in figure 4.37a is calculated from the measured height and volume. As can be seen, little change is observed in the lateral dimensions of the tower. Panel 4.37b shows the change in height undergone by the tower during the electrochemical reaction with lithium. As can be seen, the change in height is completely dependent on the lithium content in the electrode. Panel 4.37c shows the change in volume undergone by the tower during the electrochemical reaction with lithium. As expected, the change in

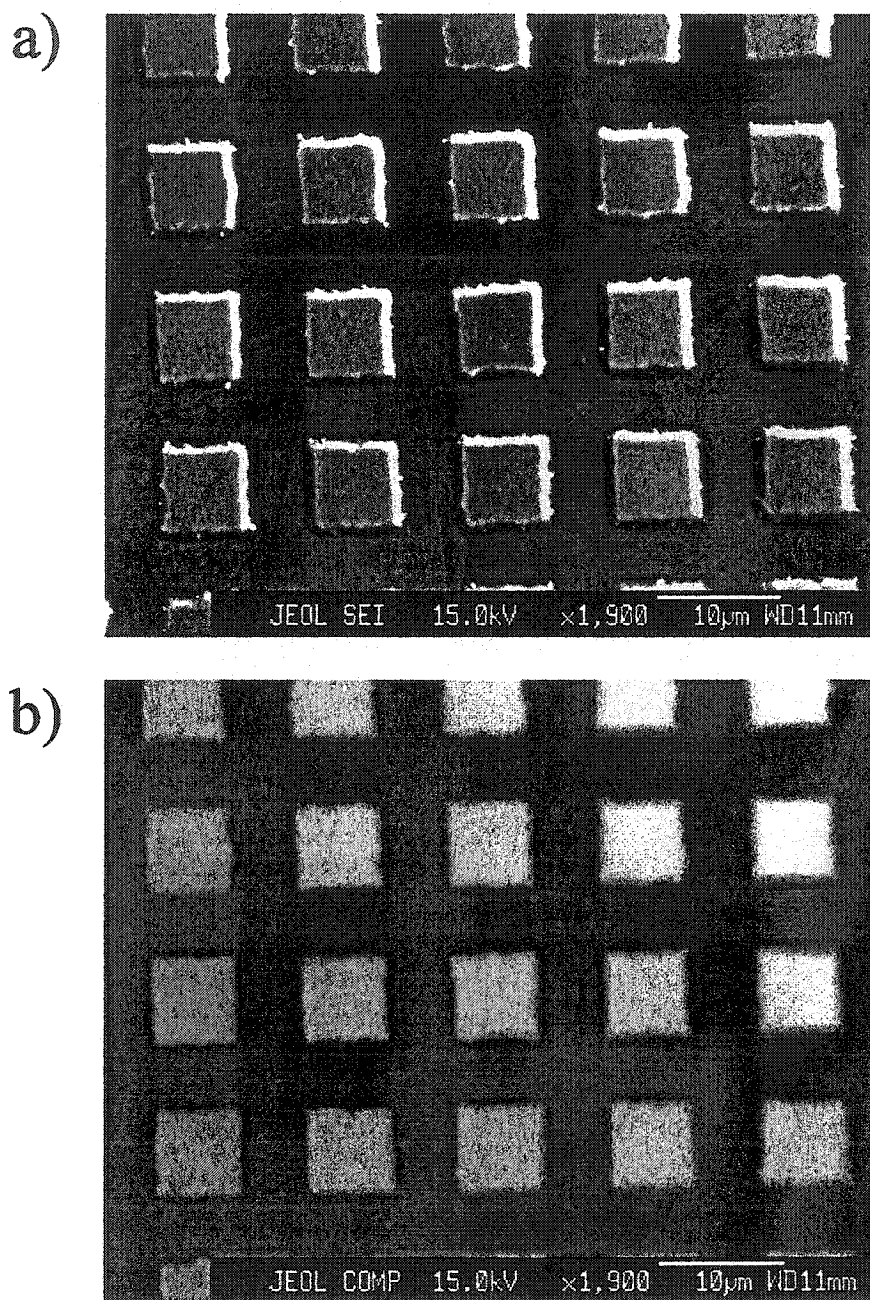


Figure 4.34: a) Secondary electron micrograph of $\text{Si}_{0.6}\text{Sn}_{0.4}$ towers. b) Backscattered SEM images of $\text{Si}_{0.6}\text{Sn}_{0.4}$ towers.

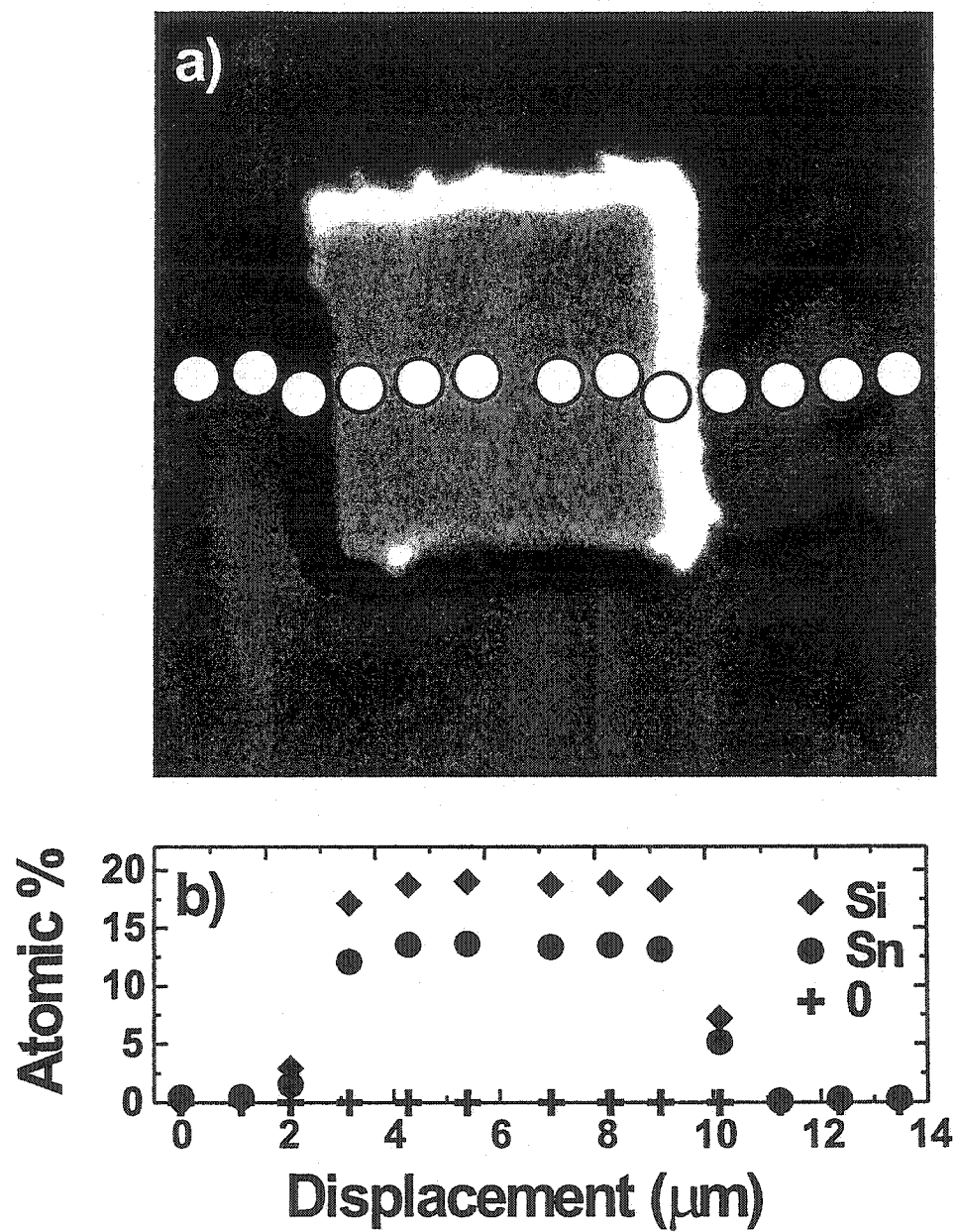


Figure 4.35: a) Secondary electron micrograph of a $\text{Si}_{0.6}\text{Sn}_{0.4}$ tower. The white dots show the approximate position and size of the electron beam used to interrogate the sample. b) Atomic percent of Si, Sn and O as a function of position. The contribution of Fe and Cr are not shown.

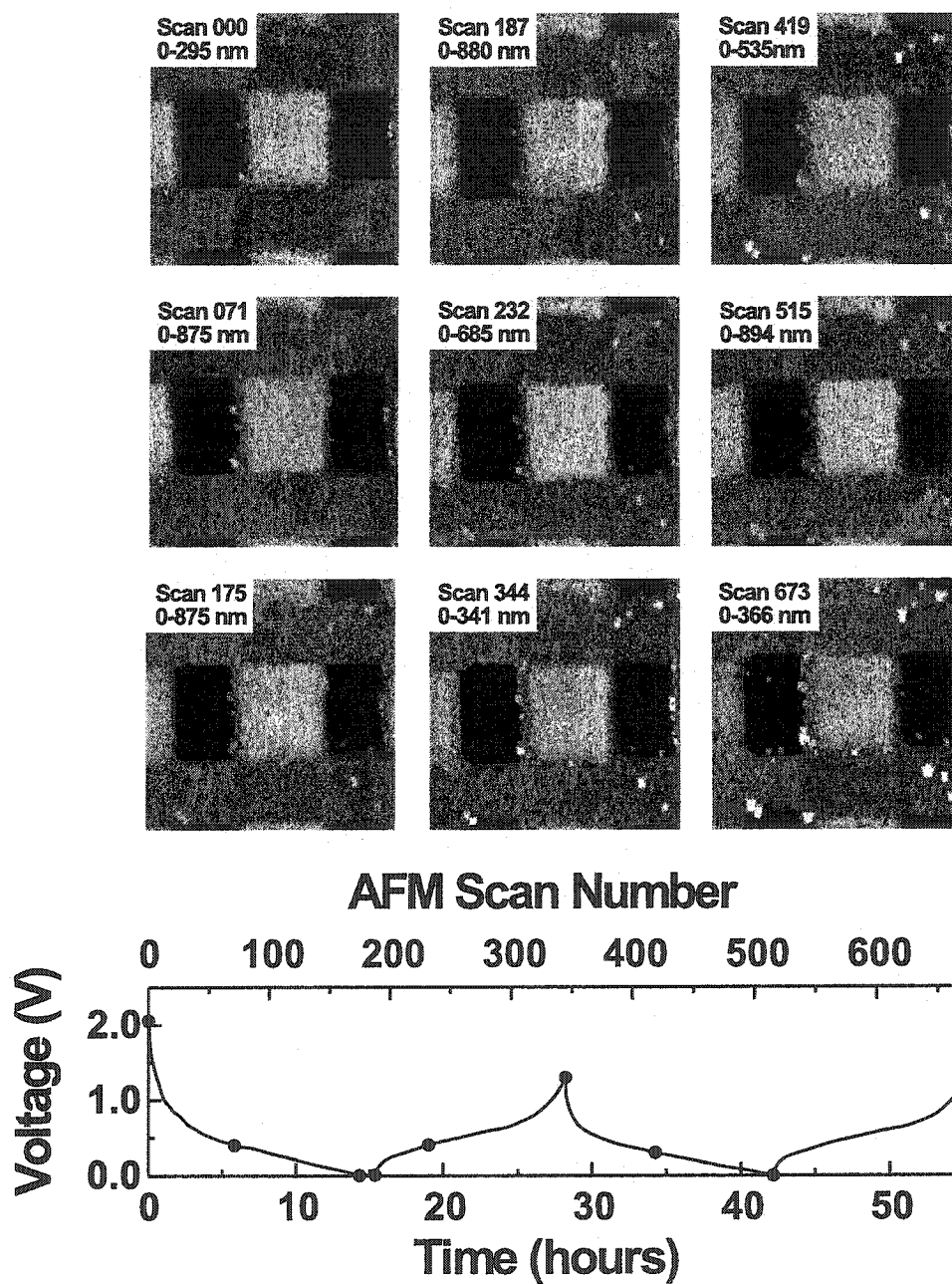


Figure 4.36: Topographic images obtained from an *in situ* AFM experiment on a patterned $\text{Si}_{0.6}\text{Sn}_{0.4}$ sample. The solid dots on the voltage versus time (bottom abscissa) and AFM scan number (top abscissa) curve shows the position where the AFM topographs were obtained.

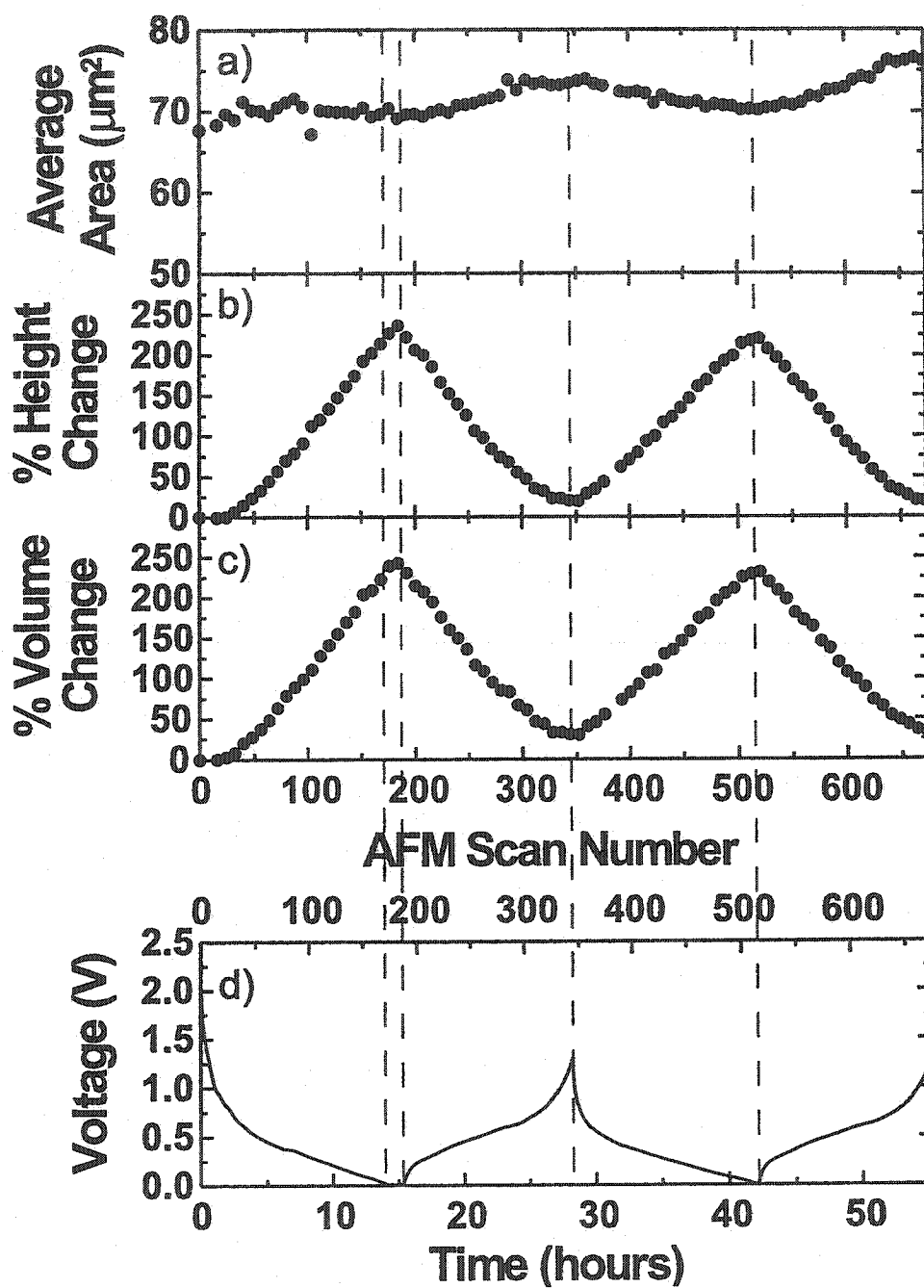


Figure 4.37: Analysis of an *in situ* AFM experiment on a patterned $\text{Si}_{0.6}\text{Sn}_{0.4}$ electrode cycled versus Li. a) The change in area b) percent change in height c) percent change in volume d) voltage versus time (bottom abscissa) and AFM scan number (top abscissa).

volume is also a function of the lithium content.

The change in volume measured is approximately 250 % which is much larger than the value obtained from the RMS roughness analysis. There are several factors that may have influenced the values obtained from the RMS roughness measurements. Since the $\text{Si}_{0.66}\text{Sn}_{0.34}$ films used in the RMS roughness analysis were made at 3M with a different sputtering system than the patterned samples made at Dalhousie, it is possible that the $\text{Si}_{0.66}\text{Sn}_{0.34}$ films are more porous than the $\text{Si}_{0.6}\text{Sn}_{0.4}$ towers. Porosity within the film would allow for a more uniform expansion (not only vertical) to occur. Attempts were made to image cross sections of $\text{Si}_{0.66}\text{Sn}_{0.34}$ and $\text{Si}_{0.6}\text{Sn}_{0.4}$ films by SEM. Unfortunately, due to the limited resolving power of the microscope, it was not possible to observe any features within the film.

It is also possible the measured results have been affected by the hysteresis suffered by the piezo material in our AFM scanner. As we showed in figure 3.6, the piezo material in our AFM scanner suffers from large hysteresis. However, what is not shown is that the hysteresis curve for shorter applied voltage ranges is inclined at a lesser angle with respect to the positive abscissa. This observation has also been observed by others [100]. This behavior would have the effect of reducing the observed height changes in our electrode material during the roughness experiment.

Another factor which certainly influenced the results taken from the RMS roughness measurements stems from the fact that the roughness of the substrates, σ_s , was never measured. In the construction of the samples used to perform the RMS roughness analysis, stainless steel disk were pre-sputtered with a copper tie-layer to improve the adhesion between the film and the substrate. Once the copper layer reached 4 μm in thickness, the power supplied to the Cu target was slowly decreased at the

same time as the power supplied to the $\text{Si}_{0.66}\text{Sn}_{0.34}$ target was slowly increased. This procedure was used to create a 10 nm integrated boundary between the Cu and the $\text{Si}_{0.66}\text{Sn}_{0.34}$ film in the hopes to further improve the adhesion of the $\text{Si}_{0.66}\text{Sn}_{0.34}$ film. Following the integrated boundary layer, a 1.2 μm layer of $\text{Si}_{0.66}\text{Sn}_{0.34}$ was deposited. Because the deposition was performed in one operation, we did not measure the RMS roughness of the Cu tie-layer. However, judging from the results in figure 4.11 It is very unlikely that the reason for the discrepancy in the RMS roughness results and those of the tower analysis are due to the fact that σ_s was not properly measured. If this was the case, we would not have obtained good agreement between the RMS roughness measurements and those from the z-bias of the AFM scanner (in other words we were lucky in choosing our value of σ_s). Since both methods gave the same value of film thickness, we believe that the discrepancy originates from the possible difference in porosity of the films and/or the hysteresis of the scanner. However, there has been observed cases where using the average voltage applied to the z-bias has given erroneous results due to changes in temperature.

Close attention to figure 4.37 shows that the electrode's height and volume increases while the electrode is at 0.01 V. This suggests that the electrode does not initially reach its full capacity. In order to verify this, *in situ* AFM measurements were performed on a $\text{Li}/\text{Si}_{0.6}\text{Sn}_{0.4}$ cell discharged to 0.0 V and held at 0.01 V for 8 hours. In order to assess the ability of Li to diffuse into $\text{Si}_{0.6}\text{Sn}_{0.4}$, the cell was discharged at a rapid rate of 10 μA . Figure 4.38 shows the change in volume (4.38a) compared to the voltage curve (4.38b) both plotted versus time (bottom abscissa) and AFM scan number (top abscissa). The electrode reaches a change in volume of approximately 250% after the initial discharge. Following, the volume change of the $\text{Si}_{0.6}\text{Sn}_{0.4}$ tower

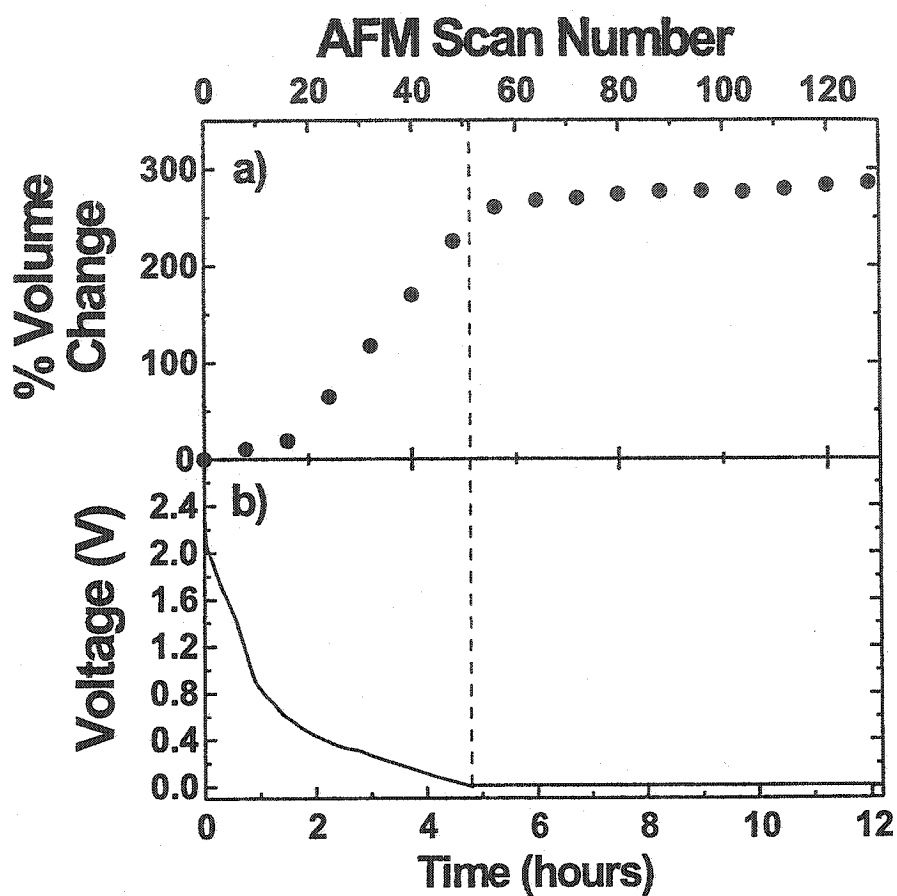


Figure 4.38: a) Change in volume of a $\text{Si}_{0.6}\text{Sn}_{0.4}$ tower and b) Voltage curve of a $\text{Li}/\text{Si}_{0.6}\text{Sn}_{0.4}$ cell plotted versus time (bottom abscissa) and AFM scan number (top abscissa).

increases slowly to almost 300%. This graph shows that $\text{Si}_{0.6}\text{Sn}_{0.4}$ reaches most of its full capacity even when discharged quickly.

Figures 4.37 b and c show that the change in height and volume of the tower does not return to zero once the lithium has been extracted from the electrode. This suggests that the $\text{Si}_{0.6}\text{Sn}_{0.4}$ tower undergoes some irreversible volume change during the first discharge. This irreversible volume change may be due to Li atoms which

have remained trapped inside the $\text{Si}_{0.6}\text{Sn}_{0.4}$ tower or the growth of a solid electrolyte interface (SEI) which is known to form on anode materials during cycling.

Unfortunately, from the analyses performed on *a*-Si and $\text{Si}_{0.6}\text{Sn}_{0.4}$ towers, it was not possible to correlate the change in thickness to the change in RMS roughness. The reason for this can be understood by comparing AFM images from a $\text{Si}_{0.66}\text{Sn}_{0.34}$ film and a $\text{Si}_{0.6}\text{Sn}_{0.4}$ patterned material. Figures 4.39 a and b show the difference between AFM topographs of a $5 \times 5 \mu\text{m}$ portion of a $\text{Si}_{0.6}\text{Sn}_{0.4}$ tower (4.39a) and a $5 \times 5 \mu\text{m}$ portion of a $\text{Si}_{0.66}\text{Sn}_{0.34}$ film (4.39b). The surface of the $\text{Si}_{0.6}\text{Sn}_{0.4}$ tower has much smaller surface features than those of $\text{Si}_{0.66}\text{Sn}_{0.34}$. This can also be seen from the RMS roughness (the standard deviation STD). The RMS roughness of the $\text{Si}_{0.6}\text{Sn}_{0.4}$ tower is 18 Å whereas the RMS roughness of the $\text{Si}_{0.66}\text{Sn}_{0.34}$ film is 256 Å. Figures 4.39 c and d show typical cross-sections of the tower (4.39c) and the $\text{Si}_{0.66}\text{Sn}_{0.34}$ film (4.39d). The cross-section of the $\text{Si}_{0.6}\text{Sn}_{0.4}$ tower is characterized by small features which, as shown by Dongmo *et al.*, give large uncertainties on the AFM RMS roughness measurements [96].

In this chapter we have shown how the volume changes of Si-Sn, Si, and Sn electrodes could be measured by atomic force microscopy. It is surprising that a brittle solid like $\text{Si}_{0.66}\text{Sn}_{0.34}$ can reversibly react with Li and undergo such large volume changes. As mentioned previously, the expansion and contraction of this material is completely analogous to the expansion and contraction of dirt as water is absorbed and removed. This is also similar to absorption of solvents by polymers. However, in both of these previous cases the host materials are much more malleable than $\text{Si}_{0.66}\text{Sn}_{0.34}$.

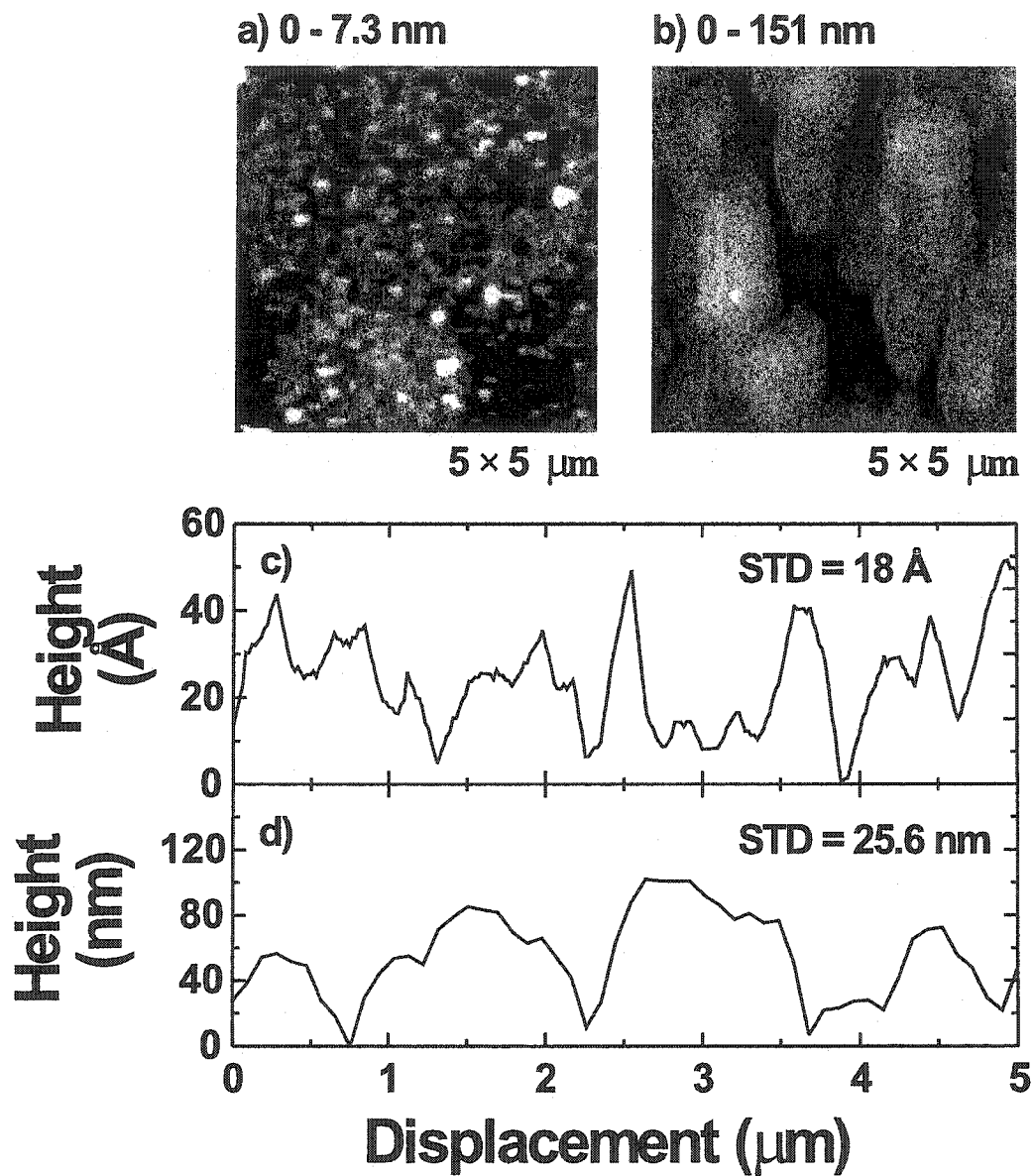


Figure 4.39: $5 \times 5 \mu\text{m}$ AFM topographs of the top of a $\text{Si}_{0.6}\text{Sn}_{0.4}$ tower a) and a $\text{Si}_{0.66}\text{Sn}_{0.34}$ film b). Typical cross-sections of the surface of a $\text{Si}_{0.6}\text{Sn}_{0.4}$ tower c), and a $\text{Si}_{0.66}\text{Sn}_{0.34}$ film d).

Chapter 5

Comparison to Other Systems

The previous chapter showed how our AFM workstation could be used to study samples of Si, Sn and $\text{Si}_{0.66}\text{Sn}_{0.34}$ as they react with Li. In each of these cases we showed how the AFM could monitor volume changes of electrode materials which exceeded 100%. In this chapter we report on two other systems which behave very differently to Si, Sn and $\text{Si}_{0.66}\text{Sn}_{0.34}$.

5.1 $\text{Mo}_{1-x}\text{Sn}_x$ System

As stated in the introduction of this thesis, many groups have attempted to synthesize *Active/Inactive* materials for application as anode materials for Li-ion batteries. This attempt has led to the study of the Mo-Sn system [101]. During this study, it was found that Sn atoms could be substituted into the BCC Mo structure to form $\text{Mo}_{1-x}\text{Sn}_x$ where $0 \leq x \leq 0.45$. Moreover, it has been shown by *in situ* x-ray diffraction that the reaction of Li with this BCC $\text{Mo}_{1-x}\text{Sn}_x$ phase causes only a small change in the lattice parameter [102].

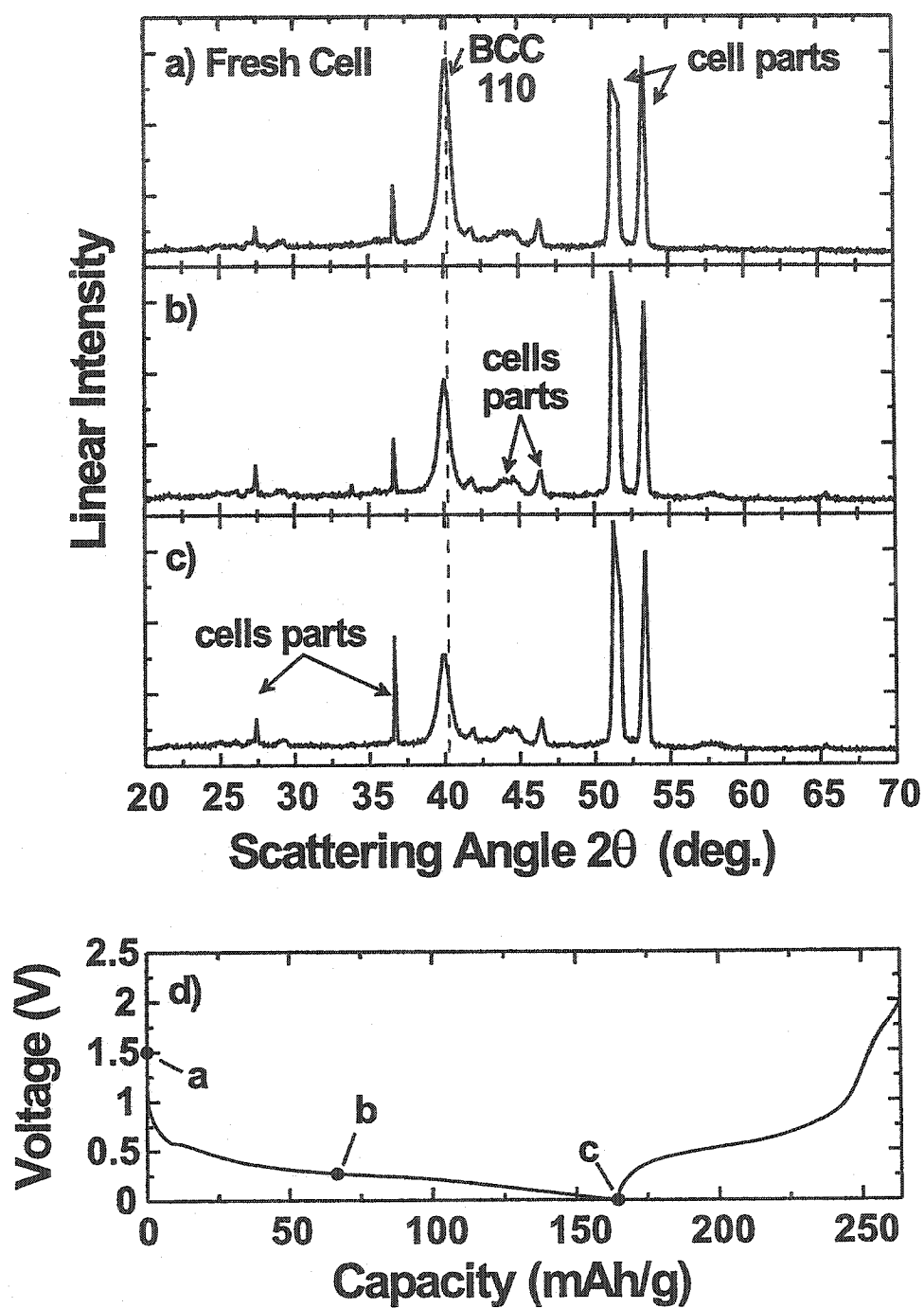


Figure 5.1: a-c) *In situ* x-ray diffraction experiment of a $\text{Mo}_{0.66}\text{Sn}_{0.34}$ electrode cycled versus Li metal. d) Voltage versus capacity of the Li/ $\text{Mo}_{0.66}\text{Sn}_{0.34}$ cell. The solid dots on the voltage curve show the position where the x-ray diffraction patterns were collected.

Figure 5.1 shows data taken by Arman Bonakdarpour of our lab. The x-ray diffraction patterns in figures 5.1 a to c show the (110) peak of BCC $\text{Mo}_{0.66}\text{Sn}_{0.34}$. Figure 5.1d shows the voltage versus capacity for the first discharge/charge cycle of the $\text{Li}/\text{Mo}_{0.66}\text{Sn}_{0.34}$ cell. The solid dots on the voltage curve show the position where the x-ray diffraction patterns were collected. The x-ray diffraction patterns show a small shift in position of the (110) peak. This change in peak position to a lower angle signifies an increase in lattice parameter. The x-ray diffraction patterns also show a decrease in peak intensity which may be due to an increase in surface texture of the electrode. It has been found that the intensity of the (110) peak does not return to its starting point when the lithium is removed from the electrode. In fact, the intensity of the peak stays the same for the rest of the electrode's life which implies that the roughness of the electrode increases during the first cycle and then stays constant throughout. *In situ* atomic force microscopy experiments performed on a $\text{Mo}_{0.58}\text{Sn}_{0.42}$ film as it cycled versus Li metal. Figure 5.2 shows the RMS roughness (5.2a) and voltage (5.2b) as a function of AFM scan number for a $\text{Li}/\text{Mo}_{0.58}\text{Sn}_{0.42}$ cell. Discharging the cell causes the RMS roughness to increase to approximately 80 Å which then remains constant for the subsequent cycles.

Figure 5.3 shows the evolution of the lattice parameter of the $\text{Mo}_{0.66}\text{Sn}_{0.34}$ electrode for several discharge/charge cycles. The lattice parameter increases by only approximately 0.02 Å during the reaction with Li. The results for each cycle are very reproducible which implies that the change in lattice parameter is not an artifact of the experimental data.

The data shown in figures 5.1 and 5.3 show strong evidence that the $\text{Mo}_{0.66}\text{Sn}_{0.34}$ phase is a *true intermetallic insertion material* for Li. Although many such systems

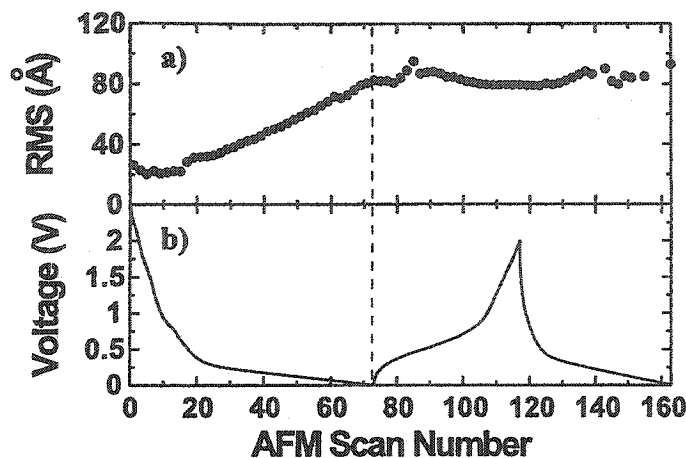


Figure 5.2: a) RMS roughness and b) voltage versus AFM scan number of a Li/Mo_{0.58}Sn_{0.42} cell.

exist for hydrogen, no intermetallic insertion materials have ever been reported for Li. As stated in the introduction of this thesis, the reaction of Li with most Sn containing materials occurs through an alloying process where different Li-Sn phase are formed in sequence [36, 57]. In the case of Mo-Sn, no new x-ray diffraction peaks are observed during the discharge. The conclusions obtained from the *in situ* x-ray diffraction results can be verified by *in situ* atomic force microscopy on a Mo-Sn electrode as it cycles versus Li metal.

Figure 5.4 shows AFM topographs of a Mo_{1-x}Sn_x sample (where x is approximately 0.35) cycled versus Li metal taken during the first discharge/charge cycle. The AFM images show that the Mo-Sn tower is relatively unchanged by the insertion and extraction of Li. The position at which each AFM image was taken is shown by black dots on the voltage curve in figure 5.4b. The analysis of the images presented in figure 5.4 is shown in figure 5.5. Panel 5.5a shows the height of the Mo-Sn tower (right ordinate, circles) and the percentage change in height (left ordinate, rhombuses). Panel 5.5b shows the volume of the Mo-Sn tower (right ordinate, squares)

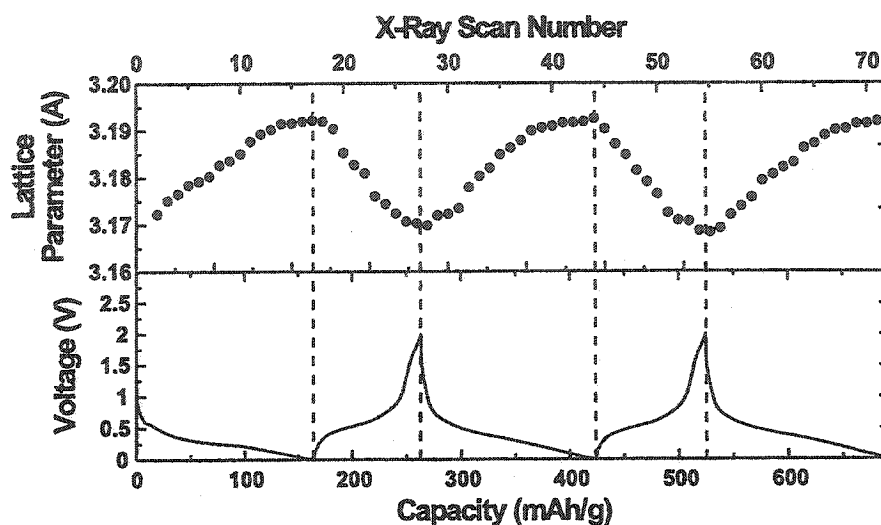


Figure 5.3: a) Lattice parameter of the BCC $\text{Mo}_{0.66}\text{Sn}_{0.34}$ phase during the reaction with Li. b) Voltage curve of a $\text{Li}/\text{Mo}_{0.66}\text{Sn}_{0.34}$ cell plotted versus capacity (bottom abscissa) and x-ray scan number (top abscissa).

and the percentage change in volume (left ordinate, crosses). The voltage versus AFM scan number is shown in panel 5.5c. As this analysis shows, the Mo-Sn tower displays no change in height or volume within expected error.

From the lattice parameter obtained from the *in situ* x-ray diffraction experiment we can calculate the expected changes in both height and volume during the reaction with Li. During the insertion of lithium, the lattice parameter of the BCC Mo-Sn phase changes from roughly 3.169 Å to 3.193 Å. This represents a volume change of less than 3%. Such a minute volume change is very difficult to measure with the AFM over a long period of time. These AFM measurements are consistent with the *in situ* x-ray diffraction measurements which imply that Li atoms are being inserted into interstitial sites of the Mo-Sn BCC phase.

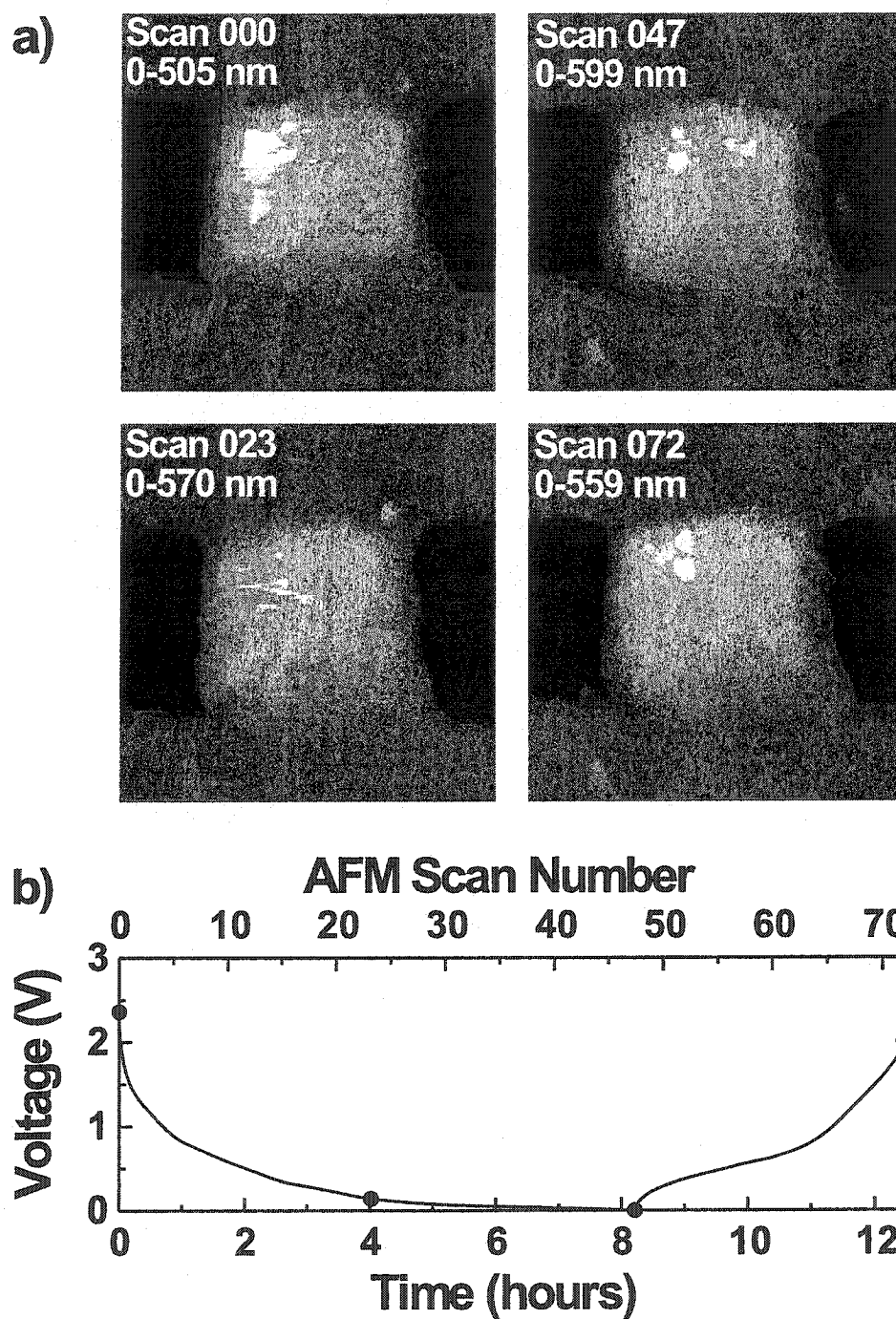


Figure 5.4: Result of an *in situ* AFM experiment on a $\text{Mo}_{0.65}\text{Sn}_{0.35}$ electrode cycled versus Li metal. (a) AFM images and (b) voltage versus both time (bottom abscissa) and AFM scan number (top abscissa). The position at which the AFM images were taken is shown on the voltage curve by solid circles.

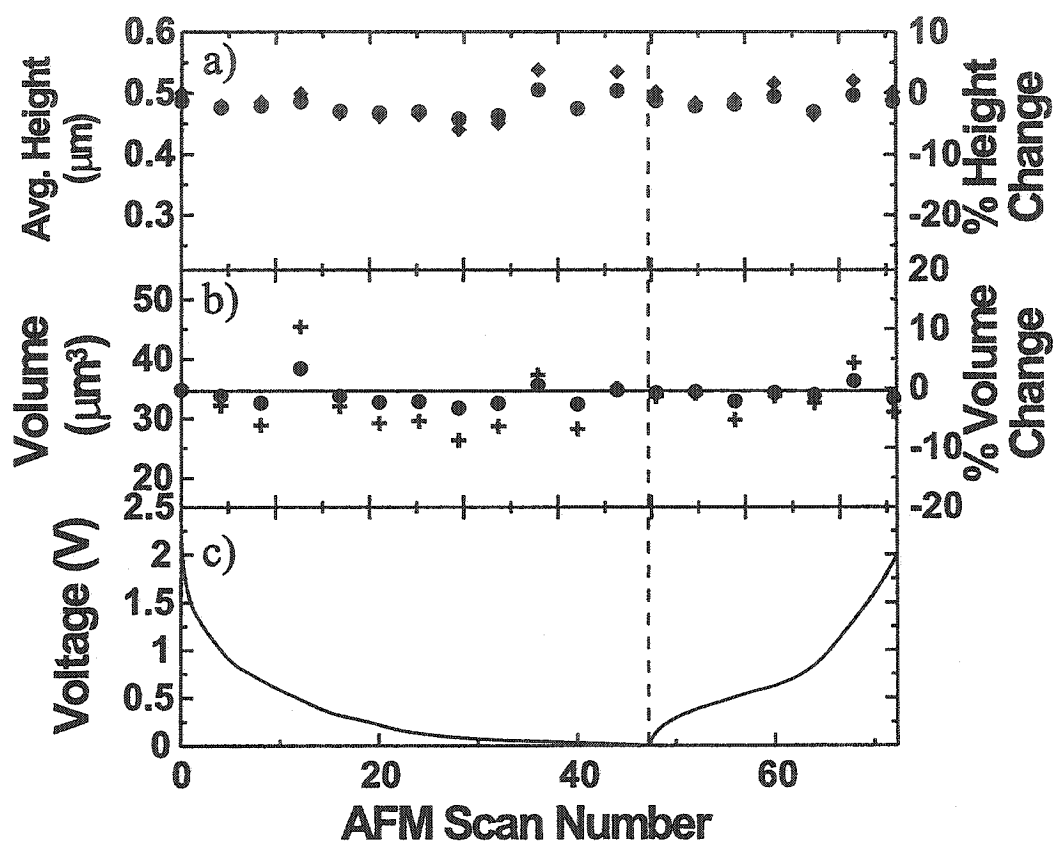


Figure 5.5: Analysis of the *in situ* AFM experiment for a $\text{Mo}_{0.65}\text{Sn}_{0.35}$ electrode cycled versus Li metal. a) Average height of the Mo-Sn tower (left ordinate, circles) and the percentage change in height (right ordinate, rhombuses). b) The volume of the Mo-Sn tower (left ordinate, circles) and the percentage change in volume (right ordinate, crosses). c) The voltage versus AFM scan number.

5.2 Al Electrodes

Pure Al has also been investigated as a possible anode material for Li-ion batteries [14, 17, 103]. Al can react with Li to form LiAl which gives a specific capacity of 990 mAh/g. However, as for most pure elements, Al has very poor capacity retention. The volume change for the reaction



is approximately 290%. As for the case of Si and Sn, this volume change should be easy to detect by *in situ* atomic force microscopy.

The first study on the reaction of Li with Al was performed using thin film Al samples sputtered on stainless steel substrates. Figure 5.6 shows the results of an *in situ* AFM experiment conducted on a thin film Al electrode as it reacts with Li. Figure 5.6a shows a small selection of the AFM images collected during the experiment while figure 5.6b shows the voltage versus time (bottom abscissa) and AFM scan number (top abscissa). The full reaction of Li with Al is available for viewing as a “time lapsed movie” on the accompanying CD or on the web-site www.physics.dal.ca/~dahn/Luc-Thesis.html. Each AFM image is approximately $24 \times 24 \mu\text{m}$ in size. In order to reduce the particle size generally formed as films crack during the charge cycle, the electrode was discharged to 0.5 V for the first few cycles. Following this, the electrode was allowed to discharge completely to 0 V. As shown by the vertical contrast scale of images 000 and 117, allowing Li to react with the Al causes the film to expand vertically. This result is similar to that seen with the Si-Sn samples shown in the previous chapter. As more lithium is allowed to react with the Al film, we see from image 145 how the surface of the electrode changes. This image shows, for the first

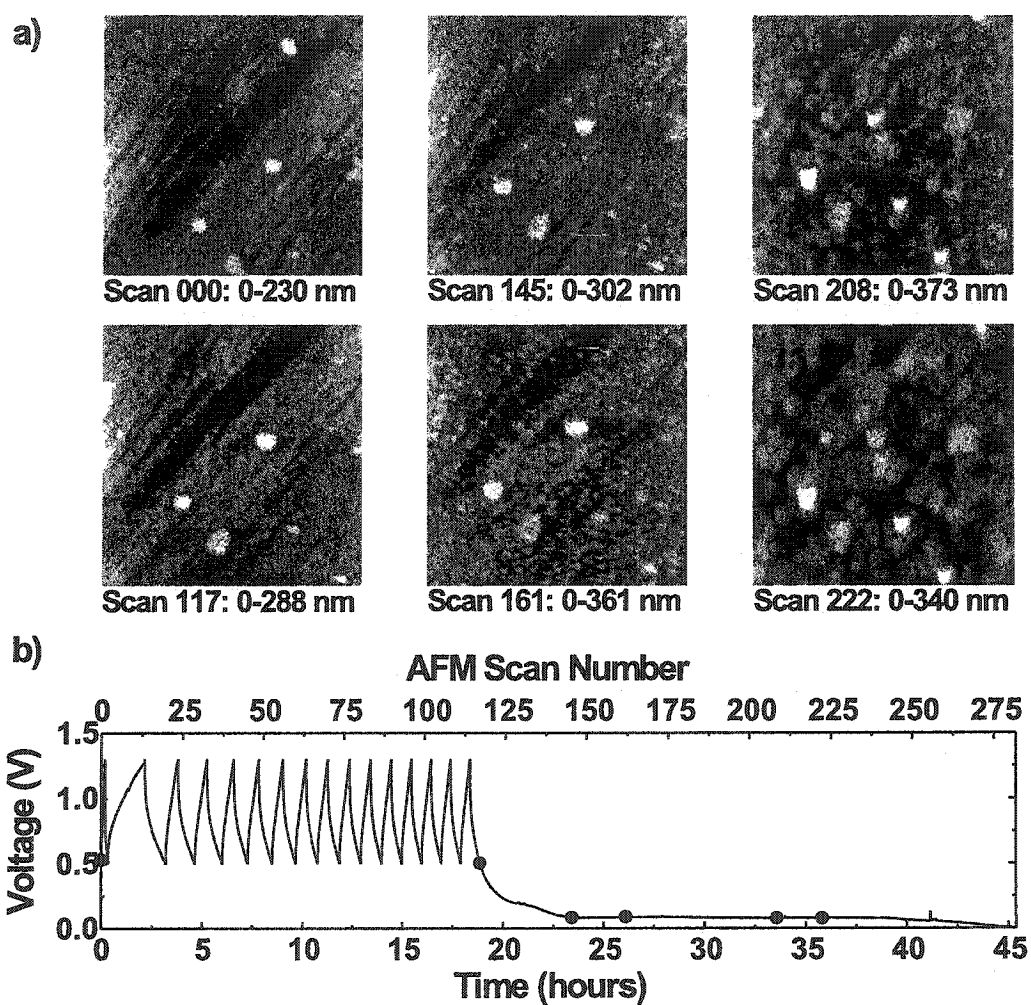


Figure 5.6: Results of an *in situ* AFM experiment conducted on an Al film as it reacts with Li. a) AFM topographs collected during the discharge. Each image is approximately $24 \times 24 \mu\text{m}$ in size. The vertical contrast scale is indicated below each image. b) Voltage versus both time (bottom abscissa) and AFM scan number (top abscissa) collected during the experiment.

time, the appearance of small “spikes” forming on the surface of the electrode. These “spikes” resemble triangles which we believe are the image of the tip. As more Li is allowed to react with the film the number of “spikes” increases as shown by image 161. Further reaction with Li causes the surface of the electrode to change as the “spikes” become larger in size. We believe that these “spikes” emanate from the formation of LiAl. Other experiments performed on Al films have shown similar results as observed here. Spikes on the surface of the Al electrode form when the voltage curve reaches the 0.2 V plateau. Unfortunately it was not able to observe the charge cycle. As we have observed repeatedly, Al films tend to crumble before reaching the end of the first discharge.

In order to better see the change in morphology we show an enhanced view of the surface of the electrode. Figure 5.7 shows a 10×10 micron portion of AFM images 000 and 161. As can be seen from images 5.7 a and c, the density of “spikes” is much larger than is observable from the larger image. Images 5.7b and d show the three dimensional representation of images 5.7a and c respectively. The three dimensional images show more clearly the growth of the electrode.

Unfortunately, from the AFM images collected on the Al film, it is not possible to use our RMS roughness analysis to obtain the change in thickness of the film. The reason for this is due to the dynamics of how the surface morphology changes. In the case of our $\text{Si}_{0.66}\text{Sn}_{0.34}$ electrode, we were able to use our RMS roughness analysis to monitor the relative change of large surface features as they expanded. For Al, we do not see the expansion of existing surface features but the growth of new ones. This mechanism, which occurs on the surface, makes it impossible to derive any changes from the bulk of the film. Because of this, patterned Al electrodes were used in an

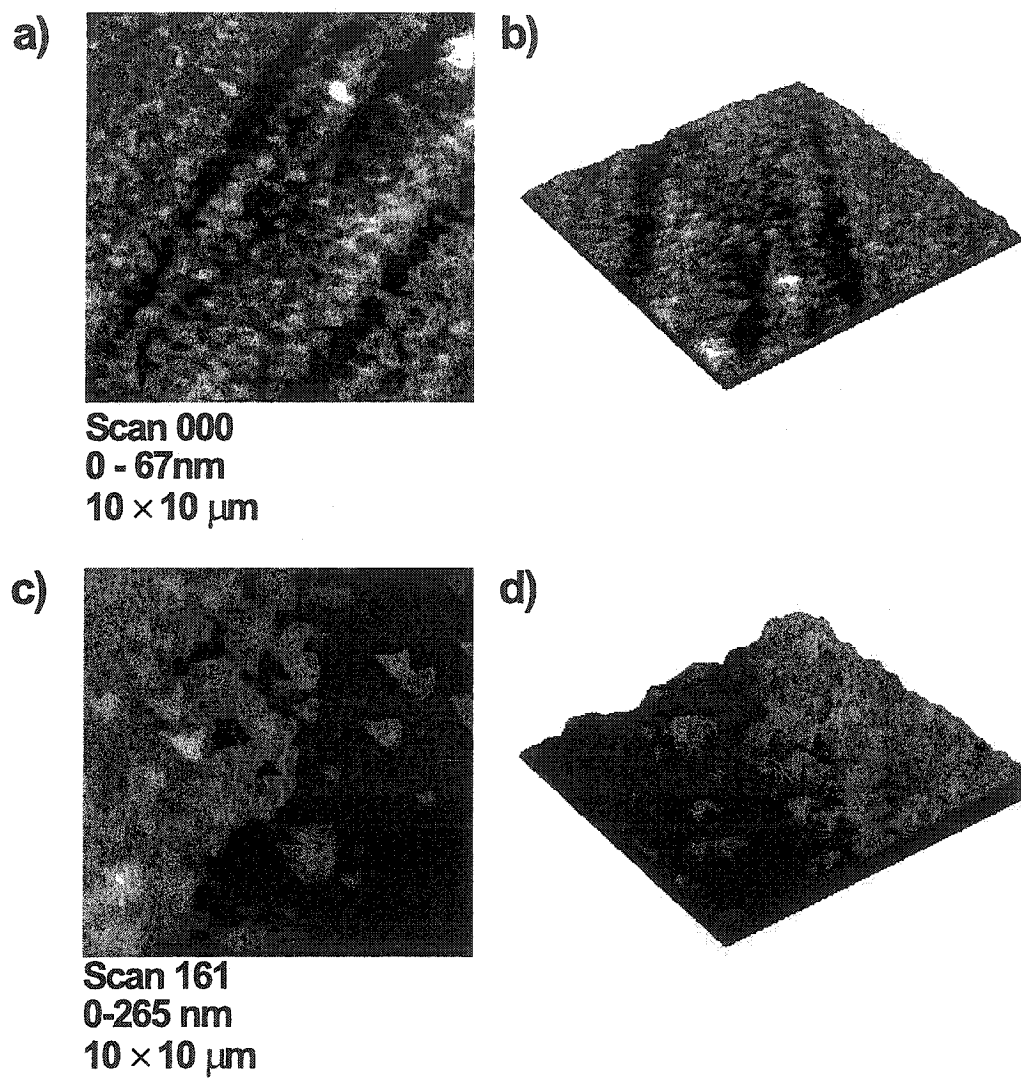


Figure 5.7: Two and three dimensional AFM images of a 10×10 portion of the AFM images a-b) 000 and c-d) 161 from figure 5.6.

attempt to measure the volume changes.

Figure 5.8a shows the AFM images of an Al tower taken during an *in situ* atomic force microscope experiment of a Li/Al cell. The voltage versus time (bottom abscissa) and AFM scan number (top abscissa) is shown in panel 5.8b. As can be seen, allowing Li to react with the Al electrode causes the towers to “pop off”. These data imply that the forces causing the Al tower to expand are greater than the adhesion bond between the tower and the stainless steel substrate.

In order to properly study the reaction of Li with Al the first step would be to find a tie layer which could withstand the shear stress at the sample/substrate interface. This, we hypothesize, would force the expansion of the Al tower in the direction perpendicular to the substrate as seen in the Si-Sn system. Alternatively, sputtering the towers on a conductive elastic coating could possibly “hold” the tower down while still allowing it to expand freely without any external constraints.

The data presented on the Mo-Sn and Al systems represent only a minute fraction of what can be obtained if a full independent study were conducted. The purpose of this chapter was simply to give two examples of different systems that show extreme behavior. In the first case, the Mo-Sn sample showed virtually no detectable change in both height and volume while the Al sample showed more dramatic results.

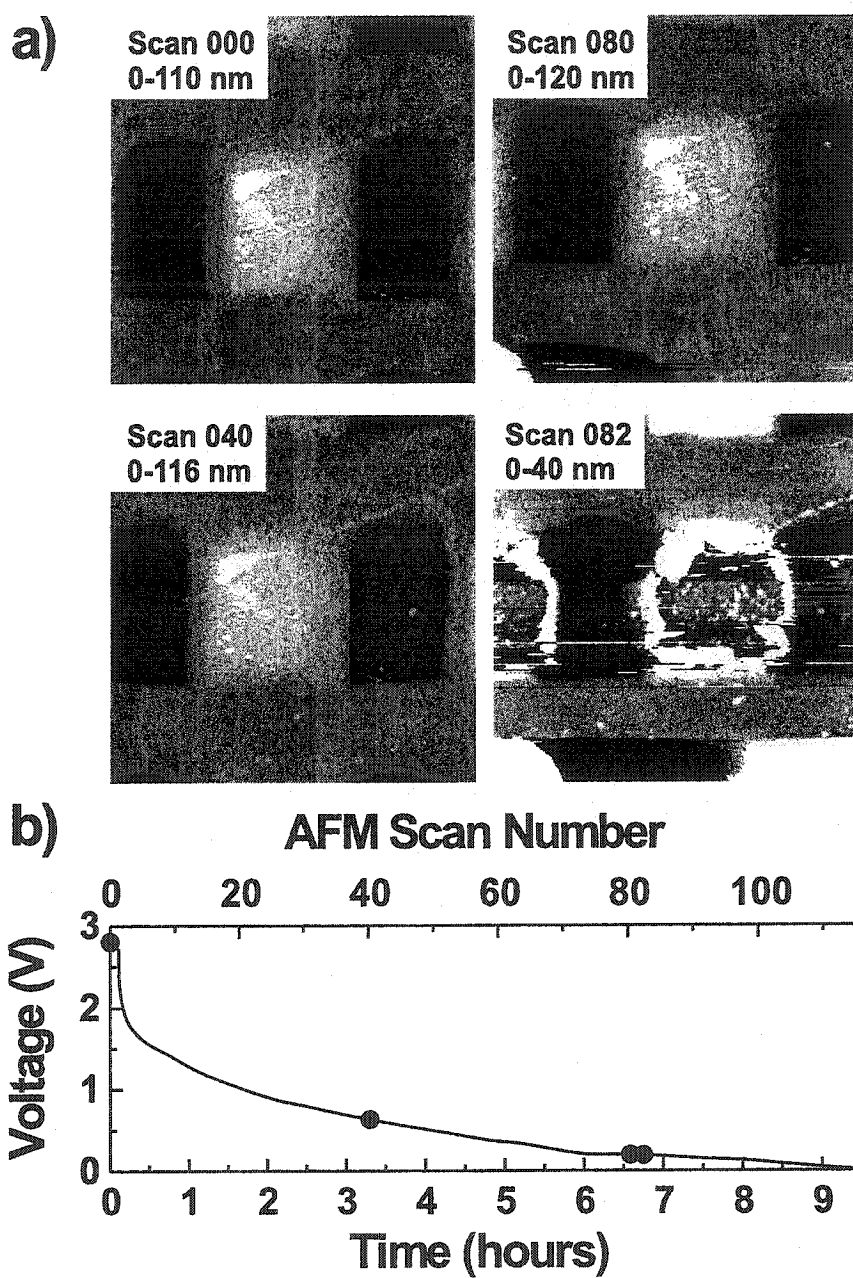


Figure 5.8: *In situ* AFM results for an Al patterned electrode cycled versus Li. a) AFM images showing the evolution of the Al tower. The position at which each AFM image was taken is shown in the b) voltage versus both time (bottom abscissa) and AFM scan number (top abscissa) plot by circles.

Chapter 6

Conclusion

In this thesis we have shown how an atomic force microscope could be placed inside an argon-filled glovebox can be used to study the morphological changes of anode materials as they react with lithium *in situ*.

We have also shown how an amorphous $\text{Si}_{0.66}\text{Sn}_{0.34}$ film can reversibly react with lithium for many cycles. *In situ* x-ray analysis showed how $\text{Si}_{0.66}\text{Sn}_{0.34}$ remains amorphous during the reaction with Li. Furthermore, from the optical microscopy data, we have shown how a $\text{Si}_{0.66}\text{Sn}_{0.34}$ film cracks into 100 μm islands (or particles) during the first charge cycle. This crack pattern was also shown to remain the same over many discharge/charge cycles. Moreover, using *in situ* atomic force microscopy, we have shown how each separate island does not undergo any sub-cracking during prolonged cycling. Using patterned electrodes of $\text{Si}_{0.6}\text{Sn}_{0.4}$, we have measured the volume changes of $\text{Si}_{0.6}\text{Sn}_{0.4}$ as it reacts with Li. *In short, in this thesis we have shown how 5-100 μm dia. particles of $\text{Si}_{0.66}\text{Sn}_{0.34}$ can reversibly react with lithium over many cycles while undergoing volume changes on the order to 250%.*

The measurements performed on these Si-Sn materials have shown that intermetallic materials can be used as anode materials in lithium-ion batteries. Even today, many researchers in the lithium-ion battery community believe that there is no future for intermetallic electrodes¹. This opinion is based on the countless reports of intermetallic systems which, similar to Sn electrodes, suffer from poor capacity retention due to self pulverization. The observations we have made in this work, we believe, finally puts an end to the speculations that intermetallic materials are inherently unsuitable for the application as anode material for lithium-ion batteries. This, we hope, will spark a new wave a research on amorphous alloys in the same way that tin-oxide materials fueled many studies on tin-based electrodes.

6.1 Future Work

In order for $\text{Si}_{0.66}\text{Sn}_{0.34}$ to become a viable commercial product as an anode material for lithium-ion batteries, it must be useable in powder form. Figure 6.1 shows the voltage versus capacity (6.1a) and capacity versus cycle number (6.1b) of a composite $\text{Si}_{0.66}\text{Sn}_{0.34}$ electrode ($\text{Si}_{0.66}\text{Sn}_{0.34}$ powder ($> 45 \mu\text{m}$) in a PVdF and Super-S carbon black mixture) cycled versus Li metal. Note that although the electrode has been discharged to only 0.2 V (where 140% expansion is expected), the capacity retention of the cell is very poor. This graph can be compared to figure 2.2 which shows the excellent capacity retention of a $\text{Si}_{0.66}\text{Sn}_{0.34}$ film cycled versus Li metal. From what we have shown in this thesis, one would expect that the cell shown in figure 6.1 should have given a better capacity retention.

¹We base this statement from many private communications and from numerous papers presented at lithium-ion battery conferences.

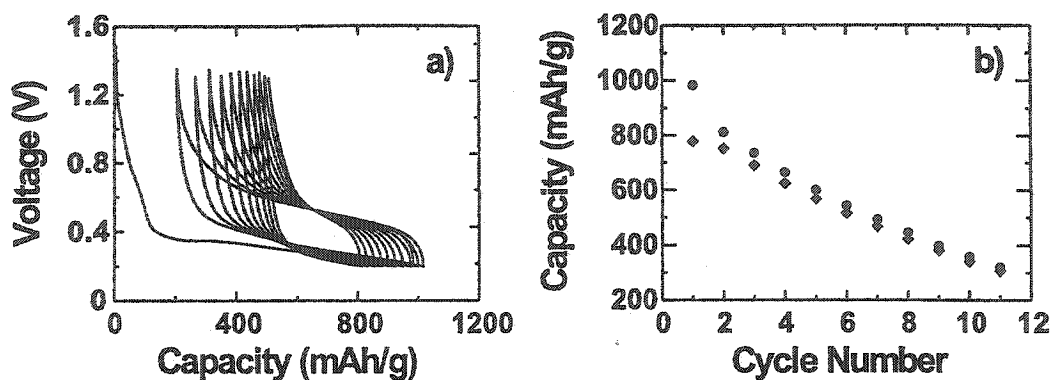


Figure 6.1: a) Voltage versus capacity and b) capacity versus cycle number of a composite $\text{Si}_{0.66}\text{Sn}_{0.34}$ electrode cycled versus Li.

It is our belief that the failure of the cell in figure 6.1 is not due to the active material but to the PVdF/Carbon mixture used to bridge the electrical contact between the active material and the current collector. We hypothesize that the PVdF/Carbon mixture cannot withstand the large volume changes dictated by the active material. Therefore the next step is to determine how to *hold on* to 10 μm dia. particles while maintaining electrical contact. In other words, the next step is to engineer an elastic conductive matrix that can accommodate volume changes on the order of 250%.

Work has already begun developing new binder materials to use as a replacement to PVdF. This work is focused on finding new polymer/carbon blends which have, amongst others, the following characteristics:

1. The polymer/carbon blends must be sufficiently elastic to withstand length changes on the order to 250 %.
2. The polymer/carbon blends must be sufficiently conductive to be used in an electrode.

3. The polymer/carbon blends must be sufficiently porous to allow electrolyte to maintain an ionic contact with the active material. Also, porosity is necessary to allow volume expansions to occur within the electrode without overly affecting the entire cell.
4. The polymers must not dissolve in the electrolyte or react with Li.

In order to test the elasticity of polymer/carbon blends, Zonghai Chen in our laboratory has assembled a workstation capable of measuring the strain suffered by a polymer/carbon film while being subjected to a specific stress. In order to help understand the dynamics of the polymer/carbon films, atomic force microscopy could be used to study the morphology changes of the film as a function of strain. Such an analysis could increase the understanding of the different failure mechanisms suffered by various polymer/carbon blends. Also the AFM could be used to quantify the porosity of different polymer/carbon blends. Studies such as these could help to focus on the key issues in finding new binder mixtures.

To truly understand the reaction mechanism of Li with $\text{Si}_{0.66}\text{Sn}_{0.34}$, a more detailed knowledge of the role of lithium is required. Although we know roughly how lithium is binding to Si and Sn, a deeper understanding could be obtained. To study this, one could perform reverse Monte Carlo analysis on *in situ* x-ray diffraction data. To do this requires high quality x-ray diffraction patterns of powdered material without the presence of super-S carbon and PVdF binder normally used in our *in situ* x-ray coin cells. These measurements would have to be performed using a Mo source (or better) to obtain high values of $q = 4\pi \sin(\theta)/\lambda$. As a supplement, neutron scattering could also be used to study the role of Li in lithiated $\text{Si}_{0.66}\text{Sn}_{0.34}$ samples. The advantage of using neutron scattering is that Li is more visible to neutrons than to x-rays. Clearly,

both of the above represent a significant amount of work and could potentially be the study of a Masters degree.

Many papers on lithium-ion batteries discuss the solid electrolyte interface (SEI) which forms on electrode materials during cycling. In our experiments we have never observed an SEI layer forming on the surface of our electrodes. We believe that since the SEI layer is only about 10 nm in thickness, it would not be noticeable compared to the large surface features of our electrodes. In order to study the formation and growth of the SEI, it would be better to use smooth surfaces like highly oriented pyrolytic graphite (HOPG) [104, 105, 106, 107] or highly polished metal surfaces. Also, it may be possible that continual sweeping of the AFM cantilever may remove the SEI layer forming on the surface of the electrode. Investigating this may require a comparison between contact mode AFM images and tapping mode AFM images performed on electrode materials.

6.2 Final Remarks

If one wanted to it would not be difficult to continue and list different projects that could be performed with our AFM workstation. Being a relatively new tool in our laboratory there are many possibilities for its use from studying polymers to the electrodeposition of electrode materials. It is my opinion that it is the versatility of the atomic force microscope that has made this project an overall success.

Appendix

Appendix A

Sputter Deposition

Sputter deposition, or what is often simply referred to as sputtering, is the process by which a material, from a specific source or target, is deposited on a substrate by the use of a glow discharge. Sputtering is often used for sample making in both industry and the scientific community. Examples of sputtered samples can be seen in every day life from highly reflective clothing to protective films on car windshields.

Figure A.1 shows a schematic representation of a sputtering system. The sputtering chamber consists of a grounded ultra high vacuum chamber connected to a sophisticated pumping system. Also connected to the chamber is an inert gas inlet and a high precision pressure gauge capable of measuring pressure as low as 10^{-7} torr or lower. Inside the chamber is located the sputtering target (the source of the material to be deposited) and the substrate opposite which sits on a mechanically driven turntable. During the sputtering process, a glow discharge or plasma (often used interchangeably) accumulated between the target and the substrate causes the mechanism for the sputtering process.

More specifically the sputter deposition process occurs as follows: First, substrate

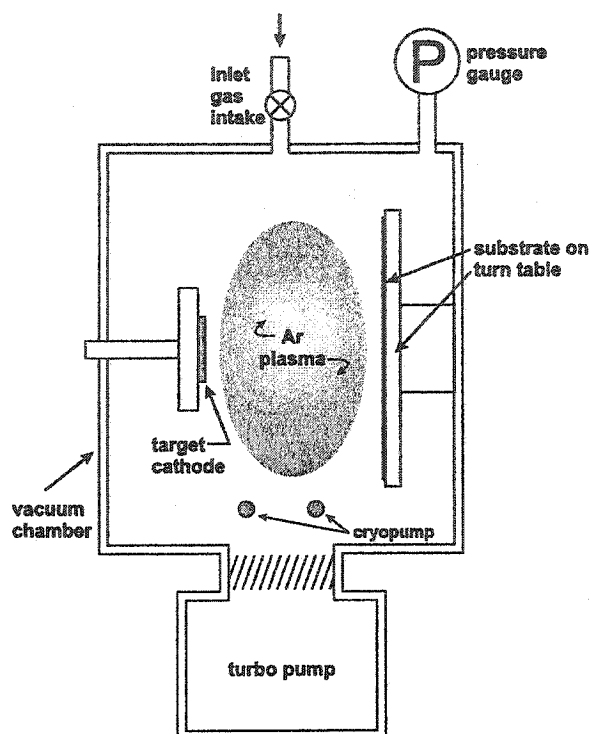


Figure A.1: Schematic representation of the inside of a sputtering chamber.

and sample are loaded and the sputtering chamber is evacuated to a pressure of approximately 10^{-7} torr. Once this pressure is achieved, the chamber is then filled with argon to a pressure in the milli-torr range. The argon gas is then ionized and used to clean the substrate. Once the substrate is properly cleaned, a bias is formed such that the plasma is attracted towards the target. When the Ar^+ ions from the plasma collide with the target, the transfer of momentum causes atoms (or clusters of atoms) to be emitted from the source and impinge on the substrate creating a film. During the collision process between argon ions and the target, electrons (known as secondary electrons) are emitted. These secondary electrons can have sufficient

energy to ionize neutral argon atoms in the plasma. In order to increase the number of collisions, magnets are often placed beneath the target as shown in figure A.2a. These magnets create a magnetic field which trap electrons and forces them to undergo a circular path (electrons drift in the $\mathbf{E} \times \mathbf{B}$ direction) in the vicinity of the target as shown in figure A.2b. These electrons then continuously ionize argon atoms thereby increasing the sputtering efficiency. This is known as *magnetron sputtering*.

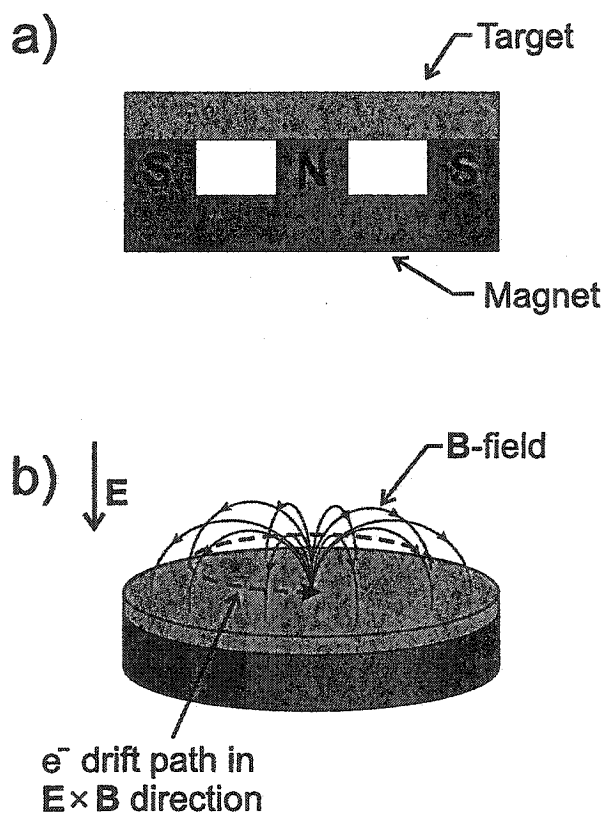


Figure A.2: Magnetrons used during sputtering. a) Position of the magnets under the target. b) Direction of the electric and magnetic fields cause electrons to undergo circular motion.

Figure A.3 a shows a picture of the sputtering machine used in our lab at Dalhousie University. As stated in the introduction of this thesis, this machine is a Corona Vacuum Coaters V3T system equipped with a turbo pump capable of reaching a base

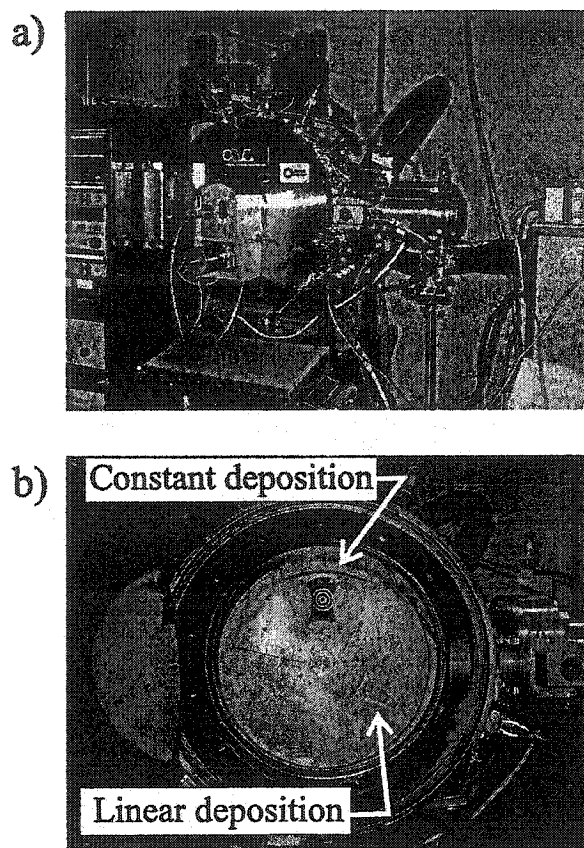


Figure A.3: (a) Sputtering machine at Dalhousie University. (b) Sputtering masks used to produce constant and linear deposition profiles.

pressure of 5×10^{-8} Torr. The inner chamber has magnetrons capable of accommodating four 5 cm diameter targets. The sputtering chamber is also equipped with a 40 cm diameter water-cooled rotating substrate table. As also stated in the introduction, this machine has been modified in order to perform combinatorial materials science. We now expand on this.

When a target is bombarded by an argon plasma during the sputtering process,

the amount of target atoms deposited on a stationary substrate resembles a Gaussian distribution where the largest thickness of sample is found directly opposite the target. Allowing the substrate to rotate underneath the target causes the atoms to be deposited in the shape of an annulus. Therefore, in order to produce a controlled deposition profile, special masks were constructed. Figure A.3b shows a picture of the masks used to perform combinatorial materials science. A schematic representation of these sputtering masks has been shown in figure 1.4. The mask shown at the top of figure A.3b is known as a *constant deposition mask*. Since the deposition on a rotating table is lowest at the outer edge of the table, the constant deposition mask must provide a larger opening at this point. Conversely, the mask shown at the bottom right of figure A.3b is called a *linear deposition mask*. This mask is designed to allow the maximum amount of deposition at the inner most part of the deposition ring and nothing at the outer edge. The deposition profile of these masks is shown schematically in figure The constant deposition mask gives a deposition profile as shown by *Material B* (— — —) while the linear deposition mask gives a deposition profile as shown by *Material A* (——).A.4. Combining the two masks together produces a

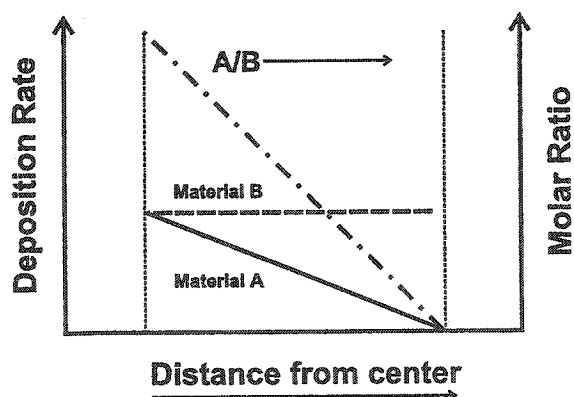


Figure A.4: Deposition profile from sputtering masks.

deposition profile as shown by the line A/B (— · — · —). With the use of these masks and through careful control of the deposition rates applied to any elements A and B, films of composition $A_{1-x}B_x$ can be grown.

Appendix B

Substrate Polishing

As in many cases in microscopy, the substrate on which the sample is deposited is as important as the sample itself. In some studies under ultra high vacuum, many days are dedicated to creating a perfect Si surface which later is made to accept the sample. Fortunately for us our substrate requirements were more flexible.

The substrates used in our study were 1 cm diameter, 1 mm thick disks made from 430 stainless steel. This particular type of metal was used because it is ferromagnetic, does not react readily (or at all) with other elements including lithium, and does not corrode in electrolyte. In order to obtain smooth substrates the metal disks were polished using a LECO VP-160 polishing machine equipped with an AP-60 pressure unit as shown in figure B.1. This system has a rotating table capable of rotation from 0 to 600 rpm. The sample can be independently rotated either with or opposite the turning direction of the rotating table. The AP-60 head can deliver a working force of 0 to 300 N. The polishing procedure is performed using a succession of polishing grits and surfaces as described in table B.1 (Directions are from Buehler, the manufacturer of the polishing supplies). It is very important that extreme precaution be exercised

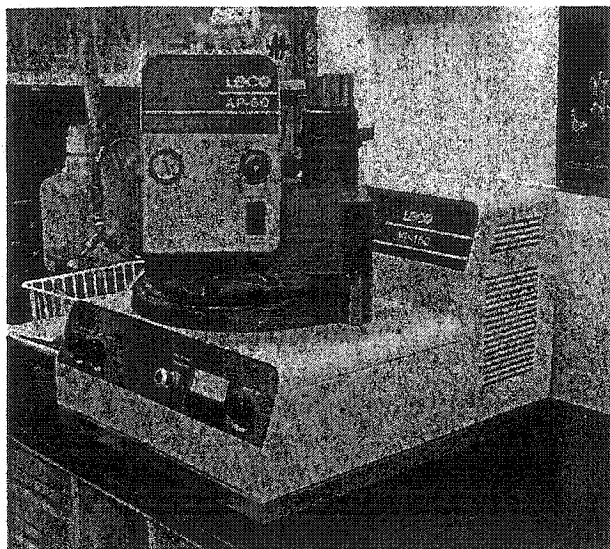


Figure B.1: LECO VP-160 polishing machine used to polish substrates for *in situ* AFM experiments.

when handling the polishing pads. Any contamination of the pad renders it useless and then it must be replaced.

It is also important not to over-polish substrates. Figure B.2 shows an AFM topograph of a stainless steel substrate which has been over-polished. The vertical contrast scale from dark to light corresponds to 0–29 Å. As can be seen, the surface of the substrate is covered by high (bright) and low (dark) areas. This type of surface feature is due to over-polishing. The stainless steel metal used for our substrates is composed of crystals on the order of 10–100 microns in size all with different orientations. We refer to these as grains. This means that on the surface of the substrate, each grain will expose different geometric planes (see Appendix A for more information on crystal planes.). Similarly to etching, each plane orientation will resist the polishing process differently therefore causing certain areas of the substrates to be lower than others.

The substrates used for our study have an RMS roughness of approximately 10–40

Table B.1: Directions for polishing stainless steel.

Surface	Lubricant	Abrasive	Time	Force/ sample	Speed (rpm)	Rotation
carbimet SiC	Water	180 grit	Until Plane	5lbs	220	Contra
carbimet* SiC	Water	600 grit	Until Plane	5lbs	220	Contra
Ultrapad		6 μm metadi supreme**	3 min	5lbs	150	Comp
Texmet 1000		3 μm metadi supreme**	2 min	5lbs	150	Comp
Texmet 1000*		1 μm metadi supreme	2 min	5lbs	150	Comp
Microcloth	water	Masterprep	1 min [‡]	5lbs	150	Contra

A sample is considered as 5 cm² of surface area.
 * Indicates steps which I have found help increase efficiency
 ** Avoid using too much Metadi Supreme – it is a polycrystalline diamond product and cuts very efficiently.
 The surface should remain slightly moist during polishing.
 Contra = contrary head vs. wheel rotation
 Comp = complimentary head vs. wheel rotation.
 Final Polish - wet cloth with water prior to application of Masterprep solution.
 During final polish, introduce water flush on cloth when 10 seconds remains.
 ‡ Do not exceed the suggested time of 1 min .

Å. As a comparison, glass microscope slides have an RMS roughness less than 10Å.

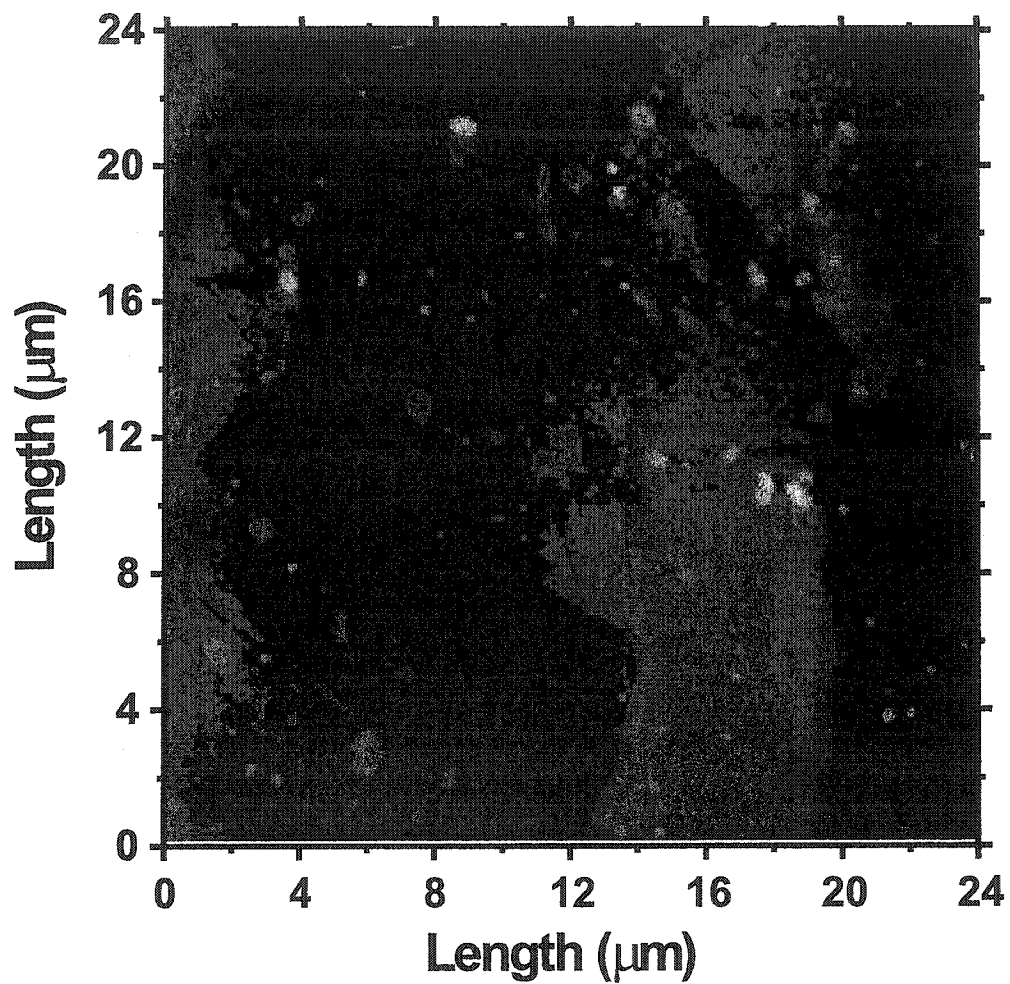


Figure B.2: AFM image of an over-polished stainless steel substrate. Over-polishing causes the different grains at the surface to be ground to different heights due to their different orientation. The vertical contrast scale from dark to light corresponds to 0–29 Å.

Appendix C

X-ray Analysis

Since its discovery in 1895, x-ray diffraction quickly became one of the most powerful tools for studying crystal structures. In this appendix, an outline of the basic theory of x-ray diffraction will be given.

C.1 Powder Diffraction

The intensity of a powder x-ray diffraction pattern obtained from a commercial x-ray diffractometer can be obtained in series of steps beginning with the scattering of an x-ray by a single electron. Figure C.1 shows an x-ray beam incident on a stationary electron at the origin. In the classical view, when an electron is subjected to electromagnetic radiation it begins to undergo simple harmonic motion about its equilibrium point. This oscillatory motion causes the electron to emit radiation in all directions. The intensity of the radiation at a point r making an angle 2θ from the

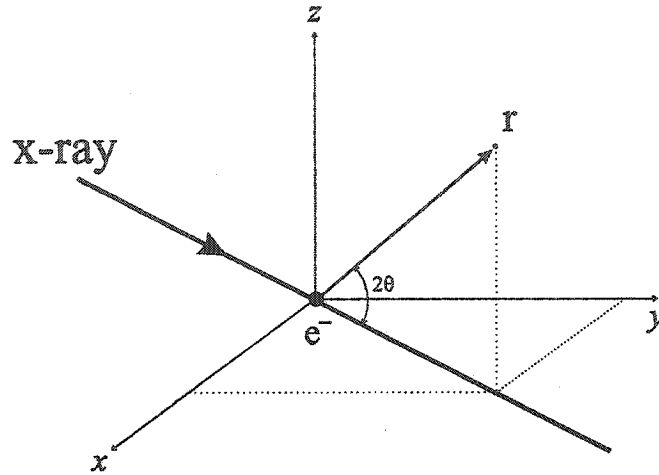


Figure C.1: X-ray beam incident on an electron.

incident beam, is given by the Thomson equation [109]:

$$I = I_0 \frac{e^4}{m_e^2 c^4 r^2} \left(\frac{1 + \cos^2(2\theta)}{2} \right) \quad (\text{C.1})$$

The factor in brackets in equation C.1 is known as the *polarization factor*.

For the case of scattering from an atom, it is sufficient to assume that the electrons form a diffused cloud around the nucleus. This introduces a new term to the Thomson equation called the *form factor*

$$f_n = \sum_n \int_0^\infty 4\pi r^2 \rho_n(r) \frac{\sin(kr)}{kr} dr \quad (\text{C.2})$$

where r the radial distance from the center of the atom, $\rho_n(r)$ is the atomic electron density, $k = \frac{4\pi \sin(\theta)}{\lambda}$ and the sum is taken over all electrons in the atom. The form factor is a measure of the scattering power of an atom.

In a unit cell, atoms are located at specific lattice sites given by the vector $\vec{r}_n = (x_n, y_n, z_n)$. When unit cells are added to form a crystal, the atoms can be seen to lie on planes labeled by the Miller indices (hkl) . The Miller indices represent a series of parallel planes which can be represented by the perpendicular vector $\vec{G} = h\vec{b}_1 + k\vec{b}_2 + l\vec{b}_3$ in reciprocal lattice space. When x-rays are incident on a crystal the diffraction of the x-rays can be considered as addition of scattered waves from a collection of parallel planes (hkl) . In such a case, the condition for constructive interference is given by the Bragg equation

$$n\lambda = 2d_{hkl} \sin \theta \quad (\text{C.3})$$

where $d_{hkl} = 2\pi/\|\vec{G}\|$ and θ is the angle of incidence of the x-ray beam. Using complex exponentials, the contribution of the scattered wave from each atom within the unit cell can be summed. This term is called the *structure factor* F_{hkl} and is given by

$$F_{hkl} = \sum_{n=1}^N f_n e^{2\pi i(hx_n + ky_n + lz_n)}. \quad (\text{C.4})$$

The intensity of the scattered x-ray beam is proportional to the modulus squared of the structure factor given by: $|F|^2 = FF^*$ where F^* is the complex conjugate.

Because of the geometry of a commercial diffractometer only a small amount of all the crystals in a powder sample will contribute to the observed intensity. Therefore, a scaling factor known as the *Lorentz factor* must be included into the equation for the integrated intensity¹.

$$\text{Lorentz factor} = \frac{1}{\sin^2(\theta) \cos(\theta)} \quad (\text{C.5})$$

In many crystal structures there are several sets of planes which have the same

¹When only the profile of the intensity is required, the Lorentz factor takes the form $1/\sin^2(\theta)$.

value of d for different values of hkl [†]. When an x-ray beam falls on a powder specimen there will be m sets of planes, having the same plane spacing, contributing to the diffracted beam. Therefore the *multiplicity factor*, m , must be included into the intensity equation.

The x-ray diffractometer used in this work is equipped with a diffracted beam monochromator used to isolate the $K\alpha$ radiation scattered from the sample. As in the case of scattering from a single electron, the scattering of x-rays from the monochromator produces a change in the polarization which adds a factor of $\cos^2(2\theta_M)$ to the polarization factor where $2\theta_m$ is the scattering angle of the monochromator.

Adding all the contributions, the relative intensity of an x-ray diffraction peak (hkl) is given by equation C.6

$$I = I_o |F_{hkl}|^2 m \frac{e^4}{8m_e^2 c^4 r^2} \left(\frac{1 + \cos^2(2\theta) \cos^2(2\theta_m)}{\sin^2(\theta) \cos(\theta)} \right). \quad (\text{C.6})$$

C.2 In Situ X-Ray Diffraction

In situ x-ray diffraction is the process where a cell under study is continuously x-rayed while cycling. Although this method has been in use for a number of years a discussion of the experimental setup is given below [110].

In order to make an *in situ* x-ray cell, 2325 type hardware was modified by inserting a beryllium disk at the bottom of the cell can. The beryllium disk acts as a solid window allowing x-rays to pass with little loss in intensity. Figure C.2 shows a sketch of an *in situ* x-ray cell. Once assembled, the cell is mounted into a special x-ray

[†]For example, in a cubic lattice the planes (100), (010), and (001) all have the same interatomic spacing.

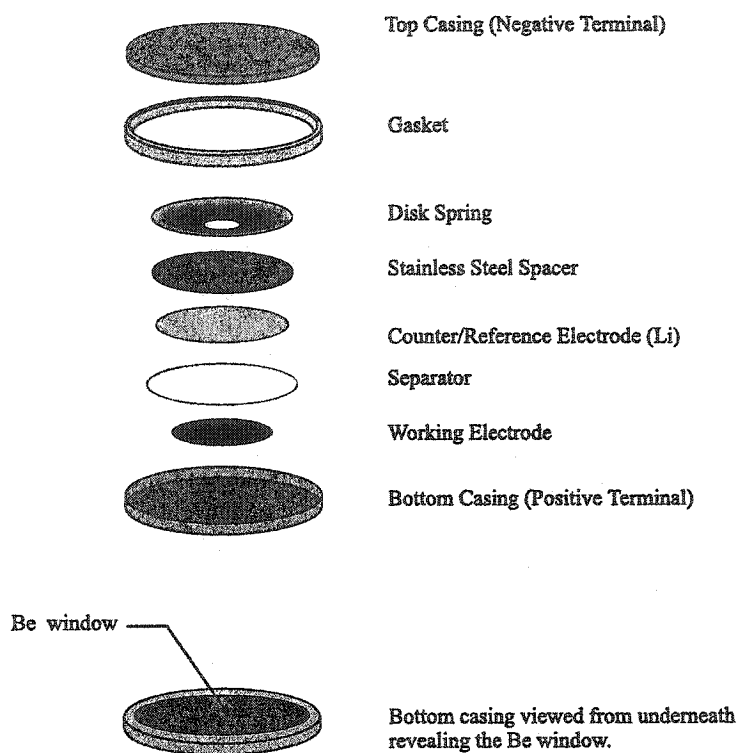


Figure C.2: Sketch of the hardware used to build *in situ* x-ray cells.

holder capable of providing current to the cell (figure C.3a), which is then mounted in the diffractometer as shown in figure C.3b. Once properly mounted, the cell is x-rayed continuously during the electrochemical process.

C.3 Debye Scattering Equation

When working with non-crystalline materials it becomes difficult to use x-ray diffraction as a method of characterizing the atomic structure. However it is possible to consider the scattering of x-rays from a collection of atoms. In electron units, the

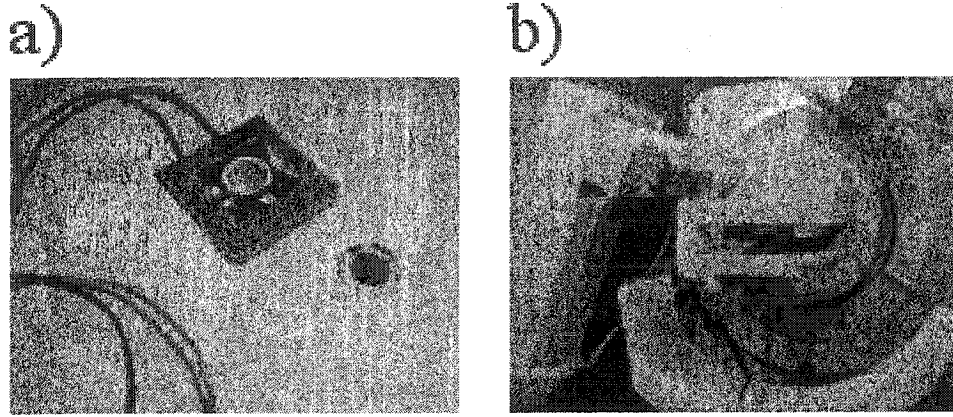


Figure C.3: Picture showing the experimental setup for performing *in situ* x-ray diffraction. a) the cell holder and b) the cell holder in the goniometer.

intensity of a scattered beam from an arrangement of atoms is given by:

$$I_{eu} = \sum_m \sum_n f_m f_n e^{(2\pi i/\lambda)(\mathbf{s}-\mathbf{s}_o)\cdot\mathbf{r}_{mn}} \quad (\text{C.7})$$

where m, n represent atoms, \mathbf{s} and \mathbf{s}_o are the direction vectors of the incident and scattered x-ray beams, and \mathbf{r}_{mn} is the vector between atoms m and n . Since \mathbf{r}_{mn} takes on all orientations with equal probability the exponential term in equation C.7 can be averaged over all space. In terms of the wave vector $\mathbf{k} = 2\pi(\mathbf{s} - \mathbf{s}_o)/\lambda$ we get:

$$\langle e^{(2\pi i/\lambda)(\mathbf{s}-\mathbf{s}_o)\cdot\mathbf{r}_{mn}} \rangle = \frac{1}{4\pi r_{mn}^2} \int_0^\pi e^{ikr_{mn} \cos(\phi)} 2\pi r_{mn}^2 \sin(\phi) d\phi = \frac{\sin(kr_{mn})}{kr_{mn}} \quad (\text{C.8})$$

Substituting this into equation C.8 we get

$$I_{eu} = \sum_m \sum_n f_m f_n \frac{\sin(kr_{mn})}{kr_{mn}}. \quad (\text{C.9})$$

Equation C.9 is called the Debye scattering equation.

Appendix D

Fitting Theory

Fitting experimental data to a given function is an important part of experimental science. Many programs like Microsoft Excel or Origin have fitting capabilities which operate by minimizing a χ^2 by sequentially changing adjustable parameters. Often these commercial packages can give erroneous results as the χ^2 falls into a local minimum as opposed to the absolute minimum. In this appendix we will show how data can be fitted reliably to specific functions.

To simplify the discussion, an example is given on how to fit experimental data y_i^{exp} to a straight line y_i . The goal to all fitting is to minimize an equation of the form:

$$\chi^2 = \sum_{i=1}^N w_i (y_i^{exp} - y_i)^2 \quad (D.1)$$

where N is the total number of data points, w_i is a weighing factor, y_i^{exp} is the experimental data and $y_i = mx_i + b$ is the equation of a straight line. Since m and b are the

parameters to be optimized, we can substitute the equation for the straight line into equation D.1 and differentiate χ^2 with respect to both m and b . Doing so we obtain:

$$\begin{aligned}\frac{\partial \chi^2}{\partial m} &= 2 \sum_{i=1}^N w_i (y_i^{exp} - (mx_i + b)) x_i \\ \frac{\partial \chi^2}{\partial b} &= 2 \sum_{i=1}^N w_i (y_i^{exp} - (mx_i + b))\end{aligned}\tag{D.2}$$

To find the minima, we set equations D.2 to zero and rearrange them as follows:

$$\begin{aligned}\sum_{i=1}^N w_i y_i^{exp} x_i &= \sum_{i=1}^N w_i (mx_i^2 + bx_i) \\ \sum_{i=1}^N w_i y_i^{exp} &= \sum_{i=1}^N w_i (mx_i + b)\end{aligned}\tag{D.3}$$

In order to get m and b equations D.3 must be solved simultaneously. This can most easily be done by writing equations D.3 in matrix form:

$$\begin{vmatrix} \sum_{i=1}^N w_i x_i^2 & \sum_{i=1}^N w_i x_i \\ \sum_{i=1}^N w_i x_i & \sum_{i=1}^N w_i \end{vmatrix} \begin{vmatrix} m \\ b \end{vmatrix} = \begin{vmatrix} \sum_{i=1}^N w_i y_i^{exp} x_i \\ \sum_{i=1}^N w_i y_i^{exp} \end{vmatrix}\tag{D.4}$$

Solving for m and b we get:

$$m = \frac{\sum_{i=1}^N w_i \sum_{i=1}^N y_i x_i - \sum_{i=1}^N w_i x_i^2 \sum_{i=1}^N w_i y_i^{exp}}{\sum_{i=1}^N w_i x_i^2 \sum_{i=1}^N w_i - \sum_{i=1}^N x_i^2}\tag{D.5}$$

$$b = \frac{\sum_{i=1}^N w_i x_i^2 \sum_{i=1}^N y_i^{exp} - \sum_{i=1}^N w_i x_i \sum_{i=1}^N w_i y_i^{exp} x_i}{\sum_{i=1}^N w_i x_i^2 \sum_{i=1}^N w_i - \sum_{i=1}^N x_i^2}\tag{D.6}$$

For today's modern computers this can be calculated very quickly.

In some cases it is necessary to rearrange the equation before proceeding with the

analysis above. In the work presented in this thesis it was necessary to fit data to the equation:

$$z = \alpha(x - x_o)^2 + \beta(y - y_o)^2 + \gamma. \quad (\text{D.7})$$

During the analysis, it was found that this equation could be more easily fitted if first rewritten as:

$$\begin{aligned} z &= \alpha(x - x_o)^2 + \beta(y - y_o)^2 + \gamma \\ &= \alpha(x^2 - 2xx_o + x_o^2) + \beta(y^2 - 2yy_o + y_o^2) + \gamma \\ &= \alpha x^2 + \beta y^2 + \delta x + \sigma y + \epsilon \end{aligned} \quad (\text{D.8})$$

where $\delta = -2\alpha x_o$, $\sigma = -2\beta y_o$, and $\epsilon = \alpha x_o^2 + \beta y_o^2 + \gamma$. Solving equation D.8 instead of equation D.7 makes the above analysis many times easier.

Appendix E

Software

As mentioned in chapter 3, there are many programs available for analyzing AFM images. However, all of these programs analyze one AFM image at a time. In this work, *in situ* AFM experiments were conducted for many hours, in which time hundreds of AFM images were collected. Therefore, in order to analyze our data, special software was written to automate the majority of the analysis.

E.1 Introduction

All of the software were written with Microsoft Visual Basic. Visual Basic is an excellent language to use for data analysis for many reasons. First of all, the programming language *Basic* is very simple to learn. Secondly, many commercial programs such as Microsoft Excel, Grapher, and even the PicoScan software used to control our AFM, accept commands from Visual Basic. This feature allows personal programs to interact with numerous other applications, ultimately creating powerful programs.

E.1.1 Tower Fitting Program

Figure E.1a shows a typical AFM image of a $\text{Si}_{0.6}\text{Sn}_{0.4}$ tower. The image shows a tower in the center of the topograph. The purpose of this program is to measure the volume, area, width, and length of the tower. The *tower fitting program* begins by loading the AFM images (binary format) in the PicoScan software and saving them in ascii (one column data) format. This is achieved by the using Active-X commands specified by the designers of the PicoScan software. The task of loading and saving data is not a difficult operation, but manipulating several hundred images by hand would require at least a few hours. All of the filenames of the AFM images are terminated (before the extension) by a three number index. This three number index allows the program to run through each image in sequence.

Before the data can be analyzed, the AFM images must first be flattened. Unfortunately, due to the unusual surface features of the towers, the commercial PicoScan software is incapable of flattening the topographs. As illustrated in figure E.1b, the left and right sides of the tower appear lower due to the hysteresis of the piezo ceramic in the AFM scanner. However, the regions above and below the tower (labeled A and B respectively) appear to be unaffected by the hysteresis. By imaging different step gratings (of known height) with the AFM, with the steps placed both parallel and perpendicular to the scan direction, it was determined that the height of the tower with respect to regions A and B corresponds to the correct numerical value of the height of the tower. Therefore, measuring the height of the towers with respect to these regions eliminates the use of scaling factors. Also, regions A and B have a large area which gives a more accurate reference for flattening the AFM images and measuring the physical properties of the tower. Therefore, in our analysis, regions A

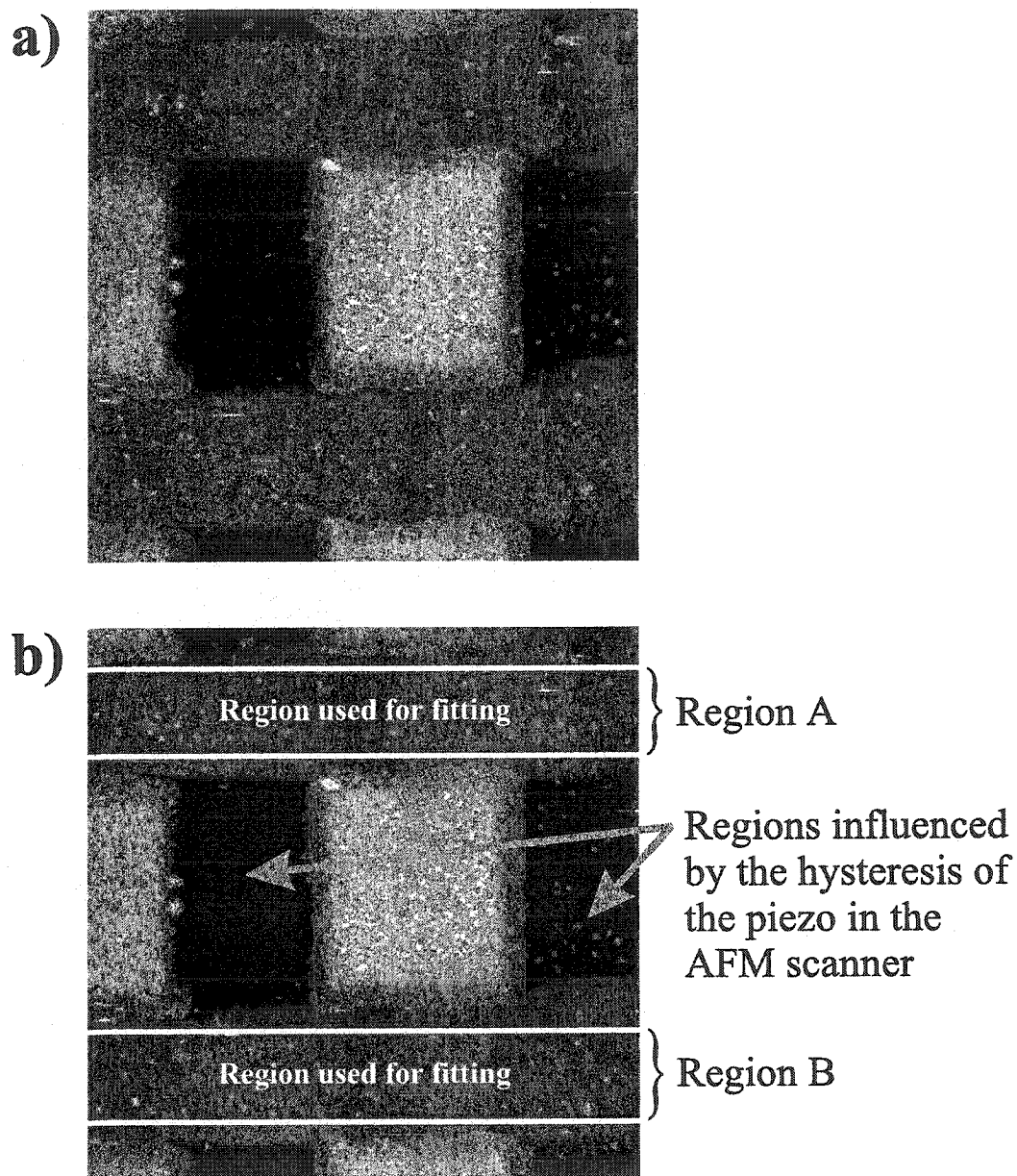


Figure E.1: a) Typical AFM topograph of a patterned $\text{Si}_{0.6}\text{Sn}_{0.4}$ electrode. b) Effects of piezo hysteresis on an AFM topographs of a $\text{Si}_{0.6}\text{Sn}_{0.4}$ patterned electrode.

and B were chosen for the data fitting¹.

The first step of the analysis was flattening the data by initially removing the tilt. This requires the user to indicate the regions on AFM image which are to be used for the data fitting (i.e. equivalent regions to A and B). Figure E.2a shows the as collected AFM data (often called the *raw data*) of a $\text{Si}_{0.6}\text{Sn}_{0.4}$ tower. To remove the tilt, regions A and B (shown in figure E.1b) are fitted to a plane. Cross-sections E.2b (horizontal white line in E.2a) and E.2c (vertical white line in E.2a) shows the fits in regions A and B are in good agreement with the data. The tilt of the AFM image is removed by subtracting the data from the fitted plane as discussed in section 3.3 of chapter 3.

Figure E.3a shows that removing the tilt from the AFM topograph exposes the curvature (or *cross coupling*) of the image. In order to flatten the AFM image, the data were fitted with an elliptical parabola, also discussed in section 3.3. Figures E.3 b and c show the excellent agreement in regions A and B between the data and the fit.

Once the AFM topographs were properly flattened, the physical dimensions of the tower were calculated. In order to measure these physical dimension, a *reference plane*, with respect to which all measurements are taken, is defined. Therefore, regions A and B of the flattened AFM image were again fitted to a plane which serves as the final *reference plane*. Following this, the software prompts the user to outline the perimeter of the tower with a rectangle. The volume of the tower is then defined by measuring everything within the rectangle and above the reference plane. Similarly, the average height of the tower is obtained by taking the average distance between

¹To be more specific, during the fitting process as described in Appendix D, all of the data outside regions A and B were assigned a weight values $w = 0$ while all of the data inside regions A and B were assigned a weight values $w = 1$.

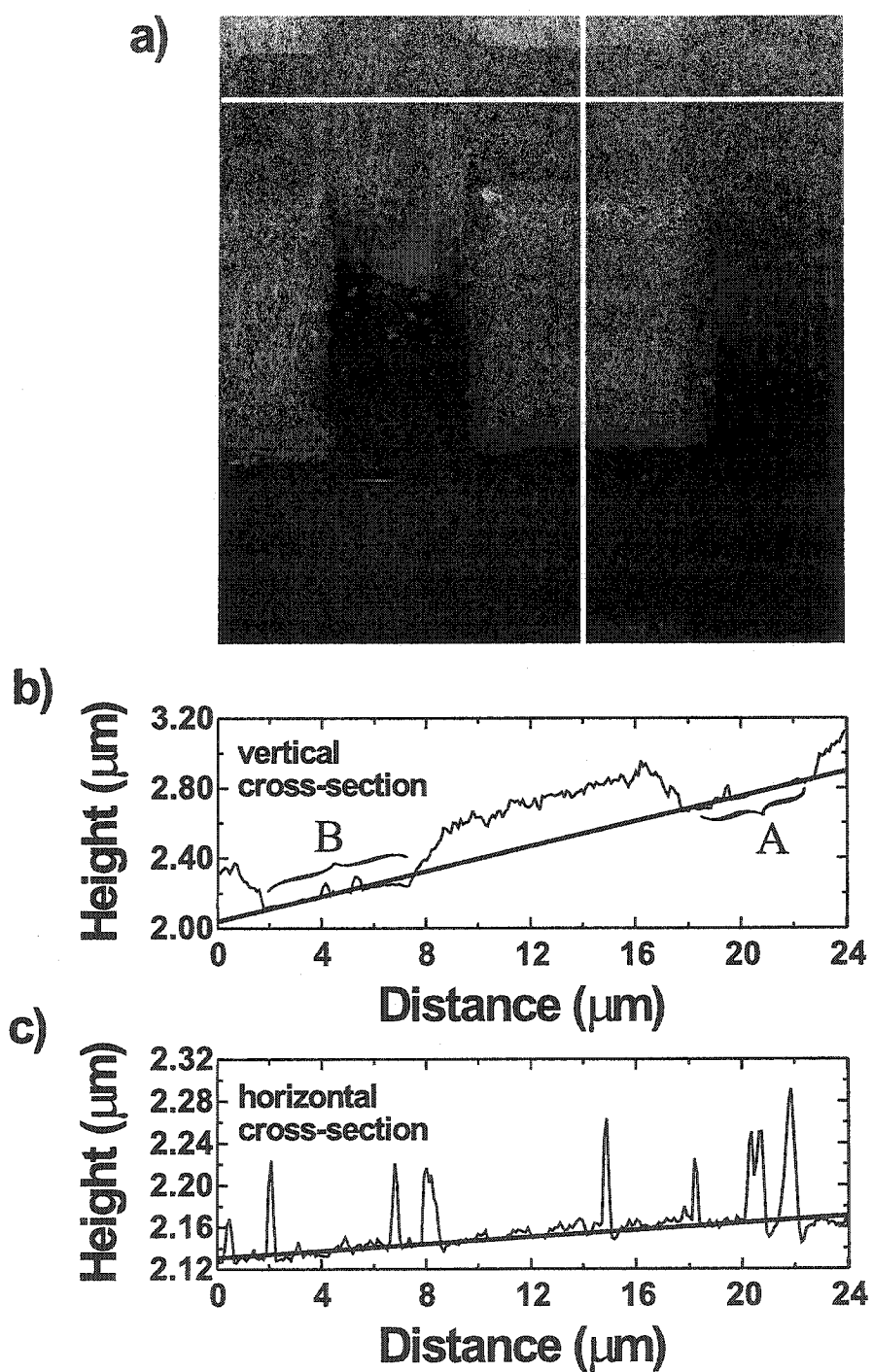


Figure E.2: a) Raw AFM topograph showing the initial tilt of the AFM image. b) Horizontal cross-section and c) vertical cross-section showing good agreement in regions A and B between the data and the fit.

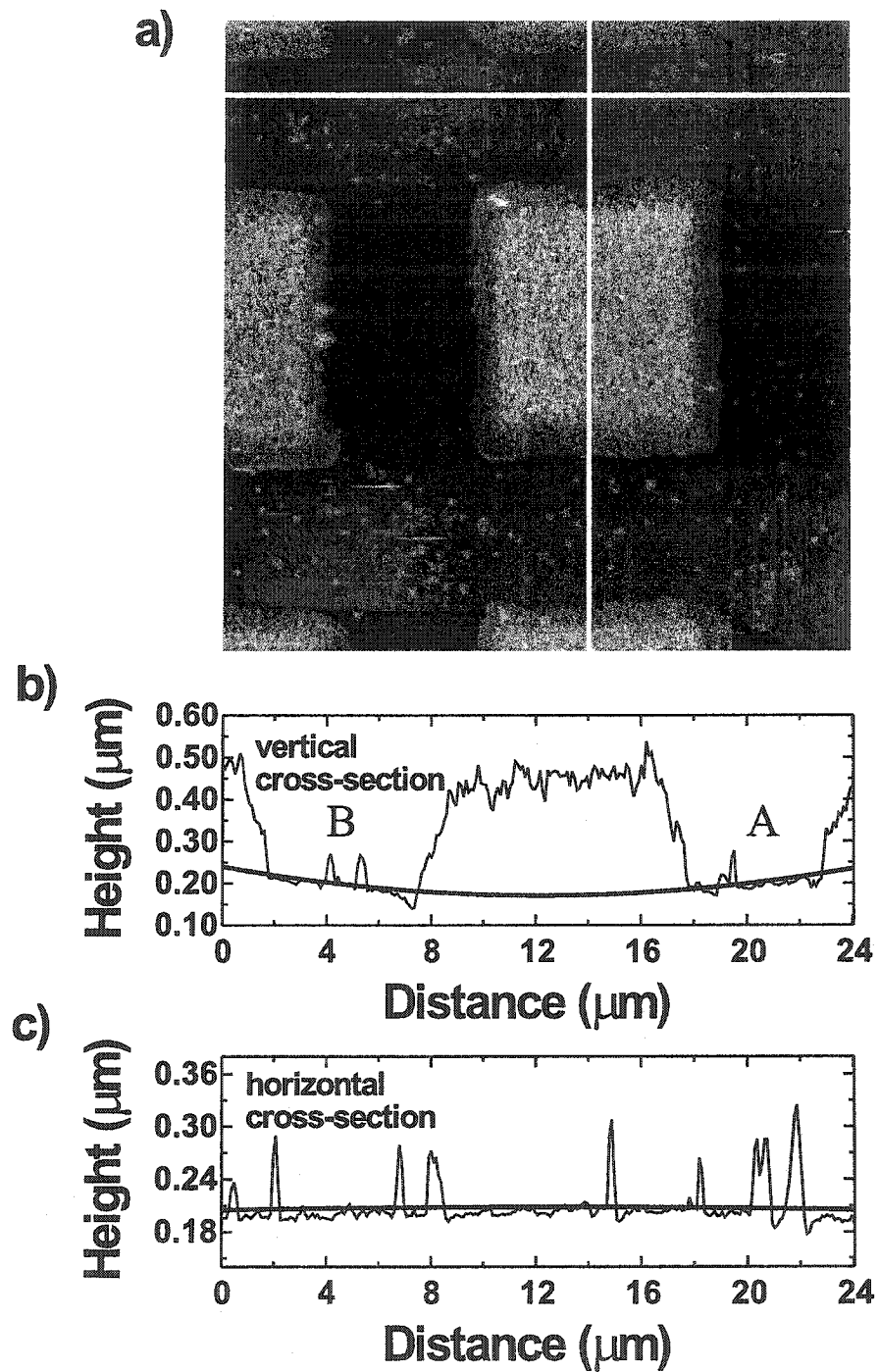


Figure E.3: a) Removing the tilt of the AFM topograph shows the cross-coupling effect. b) Horizontal cross-section and c) vertical cross-section showing good agreement in regions A and B between the data and the fit.

the *plane of reference* and a second plane defined within a smaller rectangle on the top of the tower. This second rectangle, which is also defined by the user, is shown in figure E.4.

Once the average height of the tower is determined, the length and width of the tower are obtained by calculating the average width and length at half the average height along the lines mid-way in the rectangle used to defined the height. These lines are shown in figure E.4. Finally, the area of the tower is obtained from the product of the length and width and also by dividing the volume with the average height. In the end, the program writes the index number, volume, height, area, length and width along with all the percent changes of these quantities to a common file and continues to the next image. E.4. Although the program does most of the work, a significant

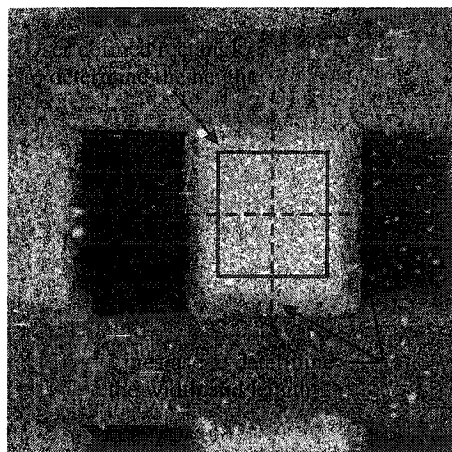


Figure E.4: Area and lines used to determine the average height, width, and length respectively.

amount of user input is required. For example, the analysis of 500 AFM images can take several hours to complete. A copy of the program used to perform the tower fitting as well as other programs used in this work can be found on the accompanying CD.

Bibliography

- [1] J.O. Besenhard, editor. *Handbook of Battery Materials*. Wiley-VCH, Weinheim, 1999.
- [2] M.S. Whittingham. Electrical energy storage and intercalation chemistry. *Science*, 192(4244):1126–1127, 1976.
- [3] I. Faul and J. Knight. Lithium rechargeable batteries - A review of recent trends. *Chem. Ind.*, 24:820–825, 1989.
- [4] F.C. Laman and K. Brandt. Effect of discharge current on cycle life of a rechargeable lithium battery. *J. Power Sources*, 24:195, 1988.
- [5] K. Brandt. A 65 Ah rechargeable lithium molybdenum disulfide battery. *J. Power Sources*, 18:117–125, 1986.
- [6] K. Brandt. Testing methods for lithium molybdenum disulfide intercalation batteries. *J. Power Sources*, 17:153–159, 1986.
- [7] D.P. Wilkinson, H. Blom, K. Brandt, and D. Wainwright. Effects of physical constraints on Li cyclability. *J. Power Sources*, 36(4):517–527, 1991.

- [8] D. Fouchard and J.B Taylor. The molice^l® rechargeable lithium system: Multicell aspects. *J. Power Sources*, 21:195, 1987.
- [9] J.J. Murray and J.E.A Alderson. Precision cycling and coulombic efficiency measurements on Li/MoS₂ and Li,Al/FeS cells. *J. Power Sources*, 26(3-4):293-299, 1989.
- [10] M. Winter, J.O. Besenhard, and P Novák. Insertion electrode materials for rechargeable lithium batteries. *Adv. Mater.*, 10:725, 1998.
- [11] M. Wakihara and O. Yamamoto, editors. *Lithium Ion Batteries*. Kodansha/Wiley-VCH, Tokyo/Weinheim, 1998.
- [12] M. Winter and J.O Besenhard. Electrochemical lithiation of tin and tin-based intermetallics and composites. *Electrochim. Acta*, 45:31-50, 1999.
- [13] B. Scrosati, A. Magistris, C.M. Mari, and G. Mariotto, editors. *Fast Ion Transport in Solids*. Kluwer Academic Publishers, Dordrecht, 1993.
- [14] A.N. Dey. Electrochemical alloying of lithium in organic electrolytes. *J. Electrochem. Soc.*, 118:1547, 1971.
- [15] J. Antula and B.F. Becker. Investigation of the cathodic reduction of lithium and arsenic ions on monocrystalline silicon by cyclic voltammetry. *J. Phys. Chem.*, 79:2470, 1975.
- [16] B.M. Rao, R.W. Francis, and H.W. Christopher. Lithium-aluminum electrode. *J. Electrochem. Soc.*, 124(10):1490-1492, 1977.

- [17] J.O. Besenhard. Cycling behaviour and corrosion of Li-Al electrodes in organic electrolytes. *J. Electroanal. Chem.*, 94:77-81, 1978.
- [18] E. Peled, A. Lombardi, and C.R. Schlaikjer. Lithium alloy-thionyl chloride cells: Performance and safety aspect. *J. Electrochem. Soc.*, 130(6):1365-1368, 1983.
- [19] T. Nohma, S. Yoshimura, K. Nishio, Y. Yamamoto, S. Fukuoka, and M Hara. Development of coin-type lithium secondary batteries containing manganese dioxide/Li-Al. *J. Power Sources*, 58(2):205-207, 1996.
- [20] J. Yang, M. Winter, and J.O. Besenhard. Small particle size multiphase Li-alloy anodes for lithium-ion-batteries. *Solid State Ionics*, 90(1-4):281-287, 1996.
- [21] J.O. Besenhard, J. Yang, and M Winter. Will advanced lithium-alloy anodes have a chance in lithium-ion batteries? *J. Power Sources*, 68(1):87-90, 1997.
- [22] Sanyo Electric. US Patent # 4,820,599, 1989.
- [23] J. Wang, I.D. Raistrick, and R.A. Huggins. Behavior of some binary lithium alloys as negative electrodes in organic solvent-based electrolytes. *J. Electrochem. Soc.*, 133(3):457, 1986.
- [24] B. A. Boukamp, G. C. Lesh, and R.A. Huggins. All-solid lithium electrodes with mixed-conductor matrix. *J. Electrochem. Soc.*, 128:725, 1981.
- [25] R.A. Huggins. US Patent # 4,436,796, 1984.
- [26] A.A. Anani, S. Crouch-Baker, and R.A. Huggins. Investigation of a ternary lithium alloy mixed-conducting matrix electrode at ambient temperature. *J. Electrochem. Soc.*, 135(8):2103, 1988.

- [27] A.A. Anani, S. Crouch-Baker, and R.A. Huggins. Kinetic and thermodynamic properties of several binary lithium alloy negative electrode materials at ambient temperature. *J. Electrochem. Soc.*, 134(12):3098, 1987.
- [28] R.A. Huggins. Polyphase alloys as rechargeable electrodes in advanced battery systems. *J. Power Sources*, 22:341–350, 1988.
- [29] W. G. Moffat. *Handbook of Binary Phase Diagrams*. Genium Publishing Corp., Schenectady, New York, 1990.
- [30] P. Villars, editor. *Pearson's Handbook of Crystallographic Data for Intermetallic Physics*. ASM International, Materials Park, OH, 1997.
- [31] Y. Idota, A. Matsufuji, Y. Maekawa, and T. Miyasaka. Tin-based amorphous oxide: A high-capacity lithium-ion-storage material. *Science*, 276(5317):1395–1397, 1997.
- [32] I. A. Courtney and J.R. Dahn. Electrochemical and *in situ* x-ray diffraction studies of the reaction of lithium with tin oxide composites. *J. Electrochem. Soc.*, 144(6):2045–2052, 1997.
- [33] I. A. Courtney and J.R. Dahn. Key factors controlling the reversibility of the reaction of lithium with SnO_2 and Sn_2BPO_6 glass. *J. Electrochem. Soc.*, 144(9):2943–2948, 1997.
- [34] I. A. Courtney, R.A. Dunlap, and J.R. Dahn. *In-situ* Sn-119 Mössbauer effect studies of the reaction of lithium with SnO and $\text{SnO}:0.25\text{B}_2\text{O}_3:0.25\text{P}_2\text{O}_5$ glass. *Electrochim. Acta*, 54(1-2):51–58, 1997.

- [35] I. A. Courtney, W.R. McKinnon, and J.R. Dahn. On the aggregation of tin in SnO composite glasses caused by the reversible reaction with lithium. *J. Electrochem. Soc.*, 146(1):59–68, 1999.
- [36] I. A. Courtney, J. S. Tse, O. Mao, J. Hafner, and J.R. Dahn. *Ab initio* calculation of the lithium-tin voltage profile. *Phys. Rev. B*, 58(23):15583–15588, 1998.
- [37] Ou Mao, R.A. Dunlap, and J.R. Dahn. Mechanically alloyed Sn-Fe(-C) powders as anode materials for Li-ion batteries: I. The Sn₂Fe-C system. *J. Electrochem. Soc.*, 146(2):405–413, 1999.
- [38] Ou Mao and J.R. Dahn. Mechanically alloyed Sn-Fe(-C) powders as anode materials for Li-ion batteries: II. The Sn-Fe system. *J. Electrochem. Soc.*, 146(2):414–422, 1999.
- [39] Ou Mao and J.R. Dahn. Mechanically alloyed Sn-Fe(-C) powders as anode materials for Li-ion batteries: III. Sn₂Fe:SnFe₃C active/inactive composites. *J. Electrochem. Soc.*, 146(2):423–427, 1999.
- [40] Ou Mao, R.L. Turner, I. A. Courtney, B.D. Fredericksen, M.I. Buckett, L.J. Krause, and J.R. Dahn. Active/inactive nanocomposites as anodes for Li-ion batteries. *Electrochemical and Solid State Letters*, 2(1):3–5, 1999.
- [41] Ou Mao, R.A. Dunlap, I. A. Courtney, and J.R. Dahn. *In situ* Mössbauer effect studies of the electrochemical reaction of lithium with mechanically alloyed Sn₂Fe. *Electrochemical and Solid State Letters*, 145(12):4195–4202, 1998.

- [42] K.D. Kepler, J.T. Vaughey, and M.M. Thackeray. $\text{Li}_x\text{Cu}_6\text{Sn}_5$ ($0 < x < 13$): An intermetallic insertion electrode for rechargeable lithium batteries. *J. Electrochem. Soc.*, 2(3):307–309, 1999.
- [43] C.S. Johnson, Vaughey JT, M.M. Thackeray, T. Sarakonsri, S.A. Hackney, L. Fransson, K. Edstrom, and J.O. Thomas. Electrochemistry and *in situ* x-ray diffraction of InSb in lithium batteries. *Electrochem. Commun.*, 2(8):595–600, 2000.
- [44] D. Larcher, L.Y. Beaulieu, O. Mao, A.E. George, and J.R. Dahn. Study of the reaction of lithium with isostructural A_2B and various Al_xB alloys. *J. Electrochem. Soc.*, 147(5):595–600, 2000.
- [45] L. Fang and B.V.R Chowdari. Sn-Ca amorphous alloy as anode for lithium ion battery. *J. Power Sources*, 97-98:181–184, 2001.
- [46] H.V. Ventkasetty, editor. *Lithium Batteries*. The Electrochemical Society, Pennington, NJ, 1981.
- [47] R.L. Turner. World intellectual property organization patent application, WO 00/03444, 2000.
- [48] R.R. Chen, Y.B. Mo, and D.A. Scherson. *In situ* atomic-force microscopy, imaging of electroprecipitated nickel hydrous oxide-films in alkaline electrolytes. *Langmuir*, 10(11):3933–3936, 1994.
- [49] Y.N. Hu and D.A. Scherson. Potential-induced plastic deformations of nickel hydrous electrodes in alkaline electrolytes: An *in situ* atomic force microscopy study. *J Phys Chem B*, 101(27):5370–5376, 1997.

- [50] Y. Cohen and D. Aurbach. The use of a special work station for *in situ* measurements of highly reactive electrochemical systems by atomic force and scanning tunneling microscopes. *Rev. of Sci. Instrum.*, 70(12):4668–4675, 1999.
- [51] Maxim Koltypin, Yaron S. Cohen, Boris Markovsky, Yair Cohen, and D. Aurbach. The study of lithium insertion-deinsertion processes into composite graphite electrodes by *in situ* atomic force microscopy (AFM). *Electrochem. Commun.*, 4(1):17–24, 2002.
- [52] Yaron S. Cohen, Yair Cohen, and D. Aurbach. Micromorphological studies of lithium electrodes in alkyl carbonate solutions using *in situ* atomic force microscopy. *J. Phys. Chem. B*, 104(51):12282–12292, 2000.
- [53] Robert C. Weast, David R. Lide, Melvin J. Astle, and William H. Beyer, editors. *Introduction to Solid State Physics*. CRC Press Inc., Boca Raton, Florida, 70th edition, (1989-1990).
- [54] T. Maruyama and H. Akagi. Thin films of amorphous silicon-tin alloy prepared by radio-frequency magnetron sputtering. *J. Electrochem. Soc.*, 144(12):4350–4353, 1997.
- [55] Charles Kittel. *Introduction to Solid State Physics*. John Wiley and Sons Inc., New York, seventh edition, 1996.
- [56] Khalid Laaziri, S. Kycia, S. Roorda, M. Chincoine, J.L. Robertson, J Wang, and S.C. Moss. High-energy x-ray diffraction study of pure amorphous silicon. *Phys. Rev. B*, 60(19):13520–13533, 1999.

- [57] J.R. Dahn, I.A. Courtney, and Ou Mao. Short-range Sn ordering and crystal structure of $\text{Li}_{4.4}\text{Sn}$ prepared by ambient temperature electrochemical methods. *Solid State Ionics*, 111(3-4):289-294, 1998.
- [58] G. Binnig and C.F. Quate. Atomic force microscope. *Phys. Rev. Lett.*, 56(9), 1986.
- [59] G. Binnig, C.H. Gerber, E. Stoll, T.R. Albrecht, and C.F. Quate. Atomic resolution with atomic force microscope. *Europhys. Lett.*, 3(12):1281-1286, 1987.
- [60] T.R. Albrecht and C.F. Quate. Atomic resolution with the atomic force microscope on conductors and nonconductors. *J. Vac. Sci. Technol.*, 6(2):271-274, 1988.
- [61] G. Meyer and N.M. Amer. Novel optical approach to atomic force microscopy. *Appl. Phys. Lett.*, 53(12):1045-1047, 1988.
- [62] J. Li and D. Lampner. *In situ* AFM study of pitting corrosion of Cu thin films. *Colloids Surf.*, 154(1-2):227-237, 1999.
- [63] S. Manne, P.K. Hansma, J. Massie, V.B. Elings, and A.A. Gewirth. Atomic-resolution electrochemistry with the atomic force microscope - copper deposition on gold. *Science*, 260:1646, 1991.
- [64] G. Binnig and D.P.E. Smith. Single-tube three dimensional scanner for scanning tunneling microscopy. *Rev. Sci. Instrum.*, 57(8):165-166, 1996.
- [65] J. E. Sader and E. White. Theoretical analysis of the static deflection of plates for atomic force microscope applications. *J. Appl. Phys.*, 74(1):1-9, 1994.

- [66] J. E. Sader. Parallel beam approximation for v-shaped atomic force microscope cantilevers. *Rev. Sci. Instrum.*, 66(9):4583–4587, 1995.
- [67] G.Y. Chen, R.J. Warmack, T. Thundat, D.P. Allison, and A. Huang. Resonance response of scanning force microscopy cantilevers. *Rev. Sci. Instrum.*, 65(8):2532–2537, 1994.
- [68] G. Y. Chen, R. J. Warmack, and A. Huang. Harmonic response of near-contact scanning force microscopy. *J. Appl. Phys.*, 78(3):1465–1469, 1995.
- [69] J.M. Neumeister and W.A. Ducker. Lateral, normal, and longitudinal spring constants of atomic-force microscopy cantilevers. *Rev. Sci. Instrum.*, 65(8):2527–2531, 1994.
- [70] A. Tori, S. Minoru, and K. Hane. A method for determining the spring constant of cantilevers for atomic force microscopy. *Meas. Sci. Technol.*, 7:179–184, 1996.
- [71] J. Senden and W. A. Ducker. Experimental determination of spring constants in atomic force microscopy. *Langmuir*, 10(4):1003–1004, 1994.
- [72] C. T. Gibson, G. S. Watson, and S. Myhra. Determination of the spring constants of probes for force microscopy/spectroscopy. *Nanotechnology*, 7(3):259–262, 1996.
- [73] S.K. Jericho and M.H. Jericho. Device for the determination of spring constants of atomic force microscope cantilevers and micromachined springs. *Rev. Sci. Instrum.*, 73(5), 2002.

- [74] S.T. Smith and L.P. Howard. A precision, low-force balance and its application to atomic-force microscope probe calibration. *Rev. Sci. Instrum.*, 65(4):903–909, 1994.
- [75] Aakikiro Torii, Minoru Sasaki, Kazuhiro Hane, and Shigeru Okuma. A method for determining the spring constant of cantilevers for atomic force microscopy. *Meas. Sci. Technol.*, 7(2):179–184, 1996.
- [76] J. E. Sader, I. Larson, and P. Mulvaney. Method for the calibration of atomic force microscope cantilevers. *Rev. Sci. Instrum.*, 66(7):3789–3798, 1995.
- [77] J. L. Hutter and J. Bechhoefer. Calibration of atomic-force microscope tips. *Rev. Sci. Instrum.*, 64(7):1868–1873, 1993.
- [78] J. Cleveland and S. Manne. A nondestructive method for determining the spring constant of cantilevers for scanning force microscopy. *Rev. Sci. Instrum.*, 64(2):403–405, 1993.
- [79] X. Yao, J. Walter, S. Burke, S. Stewart, M.H. Jericho, D. Pink, R. Hunter, and T.J. Beveridge. Atomic force microscopy and theoretical considerations of surface properties and turgor pressures of bacteria. *Colloid Surface B*, 23(2-3):213–230, 2002.
- [80] X. Yao, M.H. Jericho, D. Pink, and T.J. Beveridge. Thickness and elasticity of gram-negative murein sacculi measured by atomic force microscopy. *J. Bacteriol*, 181(25):6865–6875, 1999.

- [81] W. Xu, B.L. Blackford, J.G. Cordes, M.H. Jericho, D. Pink, and T.J. Beveridge. Atomic force microscope measurements of long-range forces near lipid-coated surfaces in electrolytes. *Biophys. J.*, 72(3):1404–1413, 1997.
- [82] Dror Sarid, editor. *Scanning Force Microscopy With Applications to Electric, Magnetic and Atomic Force*. Oxford University Press, New York, New York, revised edition, 1994.
- [83] Samuel H. Cohen, editor. *Atomic force microscopy/scanning tunneling microscopy*. Plenum Press, New York, 1994.
- [84] R. Howland and L. Benatar, editors. *A Practical Guide to Scanning Probe Microscopy*. ThermoMicroscopes, Palo Alto, 1996.
- [85] Ernst Meyer, editor. *Atomic Force Microscopy: Fundamentals to Most Advanced Applications*. Springer-Verlag, New York, 2002.
- [86] Burleigh Instruments Inc. *The Piezo book*. Burleigh Instruments, Inc., Fisher, New York.
- [87] L.Y. Beaulieu, V.K. Cumyn, K.W. Eberman, L.J. Krause, and J.R. Dahn. A system for performing simultaneous *in situ* atomic force microscopy/optical microscopy measurements on electrode materials for lithium-ion batteries. *Rev. Sci. Instrum.*, 72(8):3313–3319, 2001.
- [88] F.A. Lewis, editor. *The Palladium Hydrogen System*. Academic Press, New York, 1967.
- [89] Y. Fukai, editor. *The Metal-Hydrogen System*. Springer-Verlag, New York, 1993.

- [90] T. Yamamoto, M. Hirota, H. Inui, and M. Yamaguchi. Changes in microstructure and absorption - desorption pressures during hydrogen cycling in some intermetallic compounds. *Metals and Materials - Korea*, 6(6):609–615, 2000.
- [91] T. Brousse, R. Retoux, U. Herterich, and D.M. Schleich. Thin-film crystalline SnO₂-lithium electrodes. *J. Electrochem. Soc.*, 145(1):1–4, 1998.
- [92] A. Groisman and E. Kaplan. An experimental-study of cracking induced by desiccation. *Europhys. Lett.*, 25(6):415–420, 1994.
- [93] So Kitsunozaki. Fracture patterns induced by desiccation in a thin layer. *Phys Rev E*, 60(6):6449–6464, 1999.
- [94] P. Häring and R. Kötz. Nanoscale thickness changes of nickel-hydroxide films during electrochemical oxidation-reduction monitored by in-situ atomic-force microscopy. *J. Electroanal. Chem*, 385(2):273–277, 1995.
- [95] A. Kowal, R. Niewiara, B. Peronczyk, and J. Haber. *In situ* atomic force microscopy observation of change in thickness of nickel hydroxide layer on Ni electrode. *Langmuir*, 12(10):2332–2333, 1996.
- [96] S. Dongmo, P. Vautrot, N. Bonnet, and M. Troyon. Correction of surface roughness measurements in spm images. *Appl. Phys. A*, 66:S819–S823, 1998.
- [97] S.D. Beattie and J.R Dahn. Anomalous behavior of electroplated tin electrodes for lithium batteries. *Submitted to J. Electrochem. Soc.*, 2002.
- [98] S.D. Beattie and J.R Dahn. Behavior of electroplated Sn in Li/Sn cells. Poster presented at the 200th ECS Meeting, San Francisco, 2001.

- [99] N. Tamura, R. Ohshita, M. Fujimoto, S. Fujitani, M. Kamino, and I. Yonezu. Study on the anode behavior of Sn and Sn-Cu alloy thin-film electrodes. *J. Power Sources*, 107:48–55, 2002.
- [100] Joseph Fu. *In situ* testing and calibrating of z-piezo of an atomic force microscope. *Rev. Sci. Instrum.*, 66(7):3785–3788, 1995.
- [101] J.R. Dahn, R.L. Turner, Ou Mao, R.A. Dunlap, A.E. George, M.M. Buckett, D.J. McClure, and L.J. Krause. Structure and properties of sequentially sputtered molybdenum-tin films. *Thin Solid Films*, 408(1-2):111–122, 2002.
- [102] A. Bonakdarpour, L.Y. Beaulieu, T.D. Hatchard, K.C. Hewitt, and J.R Dahn. The insertion reaction of Li with $\text{Mo}_{1-x}\text{Sn}_x$ ($0 \leq x \leq 0.45$). Poster presented at the 11th IMLB, Monterey Ca. 2002.
- [103] J.O. Besenhard, M. Hess, and P. Komenda. Dimensionally stable Li-alloy electrodes for secondary batteries. *Solid State Ionics*, 40:525–529, 1990.
- [104] S.K. Jeong, M. Inaba, R. Mogi, Y. Iriyama, T. Abe, and Z. Ogumi. Surface film formation on a graphite negative electrode in lithium-ion batteries: AFM study on the effects of co-solvents in ethylene carbonate-based solutions. *Langmuir*, 15(26):8281–8286, 2001.
- [105] S.K. Jeong, M. Inaba, T. Abe, and Z. Ogumi. Surface film formation on graphite negative electrode in lithium-ion batteries. *J. Electrochem. Soc.*, 148(9):A989–A993, 2001.

- [106] K. Edstrom and M. Herranen. Thermal stability of the HOPG/liquid electrolyte interphase studied by *in situ* electrochemical atomic force microscopy. *J. Electrochem. Soc.*, 147(10):3628–3632, 2000.
- [107] D. Alliata, R. Kötz, P. Novák, and H Siegenthaler. Electrochemical SPM investigation of the solid electrolyte interphase film formed on HOPG electrodes. *Electrochem. Commun.*, 2(6):436–440, 2000.
- [108] B. E. Warren. *X-Ray Diffraction*. Dover Publications, Inc., New York, 1990.
- [109] B. D. Cullity. *Elements of X-ray Diffraction*. Addison-Wesley Publishing Co., 1956.
- [110] M.N. Richard, I. Koetschau, and J.R. Dahn. A cell for *in situ* x-ray diffraction based on coin cell hardware and Bellcore plastic electrode technology. *J. Electrochem. Soc.*, 144(2):554–557, 1997.